UNIVERSITY OF CALGARY

Alternative Methodologies for LiDAR System Calibration

by

Ki In Bang

A THESIS

SUBMITTED TO THE FACULTY OF GRADUATE STUDIES

IN PARTIAL FULFILMENT OF THE REQUIREMENTS FOR THE

DEGREE OF DOCTOR OF PHILOSOPHY

DEPARTMENT OF GEOMATICS ENGINEERING

CALGARY, ALBERTA

SEPTEMBER, 2010

UNIVERSITY OF
CALGARY

ABSTRACT

The objectives of this research are to analyze the LiDAR data errors and to develop alternative methodologies for estimating the biases in the LiDAR system parameters. The impact of the random/systematic errors on the derived point cloud is investigated in terms of LiDAR strip configuration such as flight altitude, direction, and scan angle. Two alternative methods have been developed to be used in cases where the point cloud coordinates of overlapping strips are available, but where raw measurements are not utilized. The simplified method consists of two steps: first, the 3D transformation parameters are estimated using the discrepancies between parallel overlapping LiDAR strips; second, the biases in the system parameters are derived from the estimated transformation parameters. The quasi rigorous method can deal with non-straight, non-parallel overlapping strips over rugged terrain with the help of time-tagged LiDAR point cloud and trajectory position data. In this method, laser firing points are estimated using the trajectory position data; then, the flight direction, beam direction, and encoder angle are calculated without system raw measurements. The proposed methods utilize a surface matching procedure, denoted as "ICPatch", which is beneficial in the absence of man-made objects in rural areas. The ICPatch procedure finds the closest point-patch pairs from overlapping strips, where one strip is represented by original points, and the other strip is represented by triangular patches. This research introduces two approaches for the similarity measure between the matched point-patch pairs. In the volume constraint, the volume of the tetrahedron which consists of the matched point and triangular patch are utilized as a constraint. For a point-based similarity measure, pseudo-conjugate points are derived from the matched point-patch pair, and the weight matrices for the pseudo-

conjugate points are modified to handle the non-conjugate problem. The feasibility of the proposed methods is verified using simulated and real datasets. Using the simulated data, the proposed methods were investigated whether they are sensitive to the assumptions used in the derivation of them. The improvement of relative and absolute accuracy of point cloud after the calibration was evaluated using real LiDAR data.

This thesis is dedicated to the soul of my father with my longing for him.

"All fathers and mothers do not have time enough to wait for their sons and

daughters."

TABLE OF CONTENTS

xiii

LIST OF ACRONYMS

2D	Two Dimensional
3D	Three Dimensional
AGL	Above Ground Level
CW	Continuous Wave
DGPS	Differential Global Positioning System
DSM	Digital Surface Model
FOV	Field Of View
GPS	Global Positioning System
ICP	Iterative Closest Point
ICPatch	Iterative Closest Patch
IMU	Inertial Measurement Unit
INS	Inertial Navigation System
LiDAR	Light Detection And Ranging
POS	Position and Orientation System
PRF	Pulse Repetition Frequency
QA	Quality Assurance
QC	Quality Control
RMSE	Root Mean Squared Error
TIN	Triangular Irregular Network

CHAPTER 1

INTRODUCTION

1.1   Problem Definition

The availability of 3D surface data is very important for various industrial, public, and military applications. Light Detection And Ranging (LiDAR) is an active sensor system used to collect 3D information from an object surface by using laser pulses. Recently, LiDAR systems have been proven as a cost-effective tool for the generation of surface models with dense/accurate irregular points. The products of LiDAR system surpasses thereby the quality of those derived from other techniques such as manual photogrammetric DSM generation, radar interferometry, and contour interpolation. A typical LiDAR system consists of a laser ranging and scanning unit, together with a Position and Orientation System (POS) which encompasses an integrated Differential Global Positioning System (DGPS) and an Inertial Navigation System (INS). The laser ranging unit estimates the distances from the sensor to the mapped surface by measuring the time delay between a laser pulse transmission and its detection, while the onboard GPS/INS component provides the position and orientation of the platform. The vertical accuracy of LiDAR data is relatively high (5-30 cm) compared to other methodologies. The quality of the LiDAR data is affected by many factors: the overall accuracy of the integrated GPS/INS position and orientation, the correctness of the system calibration, the average point density, flight altitude & speed, and the physical nature of the objects scanned (McGlone et al., 2004).

LiDAR data contaminated by systematic errors cannot guarantee the expected accuracy and exhibit discrepancies in overlapping areas. In order to improve the quality of LiDAR data, strip adjustment and LiDAR system calibration have been carried out. The differences between these two approaches conventionally lie in the type of available data and applications. The strip adjustment is performed to improve the compatibility between overlapping strips, while the calibration of a LiDAR system is carried out to make sure that the LiDAR final products meet the required accuracies. The strip adjustment reduces or eliminates the discrepancies between overlapping strips using 3D point cloud coordinates. On the other hand, the calibration procedure recovers the system parameters using the LiDAR geo-referencing equation and system raw measurements: GPS/INS navigation information, scanner encoder angles, and laser ranges (Habib et al., 2009a). The advantage of the strip adjustment is that end-users can reduce the discrepancies between overlapping strips which are caused by systematic errors without the need for the system raw measurements; however, the strip adjustment is limited to estimating the discrepancies between overlapping strips using an empirical transformation function. In other words, the strip adjustment is an empirical approach for increasing the compatibility among multiple strips rather than improving the accuracy of LiDAR points.

Many methodologies for LiDAR system calibration have been investigated over the past decade. Nevertheless, there is still no standard work flow commonly accepted for LiDAR system calibration; the lack of a standard error model and calibration method remains an important issue. The LiDAR system consists of several components, and thus, numerous error sources can take place (e.g., GPS time error, time synchronization between GPS, INS, and a laser scanner, interpolation of GPS/INS measurements, system components

mounting error, laser range and encoder angle error) (Baltsavias, 1999a; Schenk, 2001; Katzenbeisser, 2003). It is almost impossible and unnecessary to consider every conceivable error that may arise during the LiDAR system calibration because it is hard to define the error models for all the individual sensors. In addition, some errors are relatively insignificant, and others are tightly coupled (Schenk 2001; Habib et al., 2007). For these reasons, one should consider the adequate error model for the LiDAR system calibration, and decide on which systematic parameters should be calibrated or ignored.

A typical LiDAR system calibration method requires system raw measurements because there is no redundancy in 3D point cloud coordinates to solve the system parameters. However, it is not expected that LiDAR data users are commonly allowed to access the system raw measurement. Due to this restriction, the improvement of LiDAR data accuracy by removing the impact of the system biases on the derived point clouds cannot be achieved by data users. In addition, there is no standard for LiDAR system configuration; for example, the definitions of boresight angles, lever-arm parameters, and encoder angles depend on a system manufacturer. The lack of the standard of the system configuration leads to the problem that pre-developed calibration method cannot be directly used for any other LiDAR systems without modification even though there is no change in the calibration methodology.

LiDAR calibration requires the identification of common elements or primitives in overlapping LiDAR strips as well as control data. Hence, one should consider the appropriate primitives for such a task. Distinct points have been traditionally used as a primitive in photogrammetric data for a long time. However, it is well known that distinct

points and lines cannot be directly captured by a LiDAR system as the system produces irregular point data unlike photogrammetric systems (Ackermann, 1999). Planar patches and/or linear features indirectly measured have been alternatively used as conjugate surface elements in overlapping strips (Skaloud and Lichti, 2006; Habib et al., 2007; Lee et al., 2007; Skaloud and Schaer, 2007; Habib et al., 2009b). Planar patches can be extracted by plane segmentation; linear features are derived through the intersection of adjacent planar patches such as gable roofs. However, planar and linear features can be reliably extracted only in urban areas. Therefore, a surface matching procedure should be used for the establishment of correspondences between point clouds with non-identifiable landmarks (Zhang, 1994).

1.2   Research Objectives and Scope

The objectives of this research are to analyze the LiDAR systematic errors and to develop methods for estimating biases in the LiDAR system parameters. Possible approaches for LiDAR system calibration depend on which data is available; that is, the availability of system raw measurements, control data from GPS surveying and/or reference surface data, and the availability of additional images that overlap with the considered LiDAR data. This research proposes alternative calibration methods to be used in cases where the point cloud coordinates of overlapping strips are available, but where raw measurements are not utilized. In addition, the alternative calibration methods utilize a surface matching procedure, which is called Iterative Closest Patch (ICPatch). It can provide a benefit in the absence of man-made objects in rural areas. There is no need to extract identifiable linear and/or areal features (landmarks). Sections 1.2.1 and 1.2.2 will go into detail about

the research objectives: LiDAR system calibration and correspondences between point cloud datasets.

1.2.1   LiDAR System Calibration

A LiDAR system provides 3D coordinates of point cloud through the LiDAR geo-referencing equation which is a function of boresight angles, lever-arm offset, and system measurements. If there are biases in the system parameters, the point cloud coordinates will be distorted. The LiDAR system calibration is carried out as a quality assurance (QA) procedure to determine the system parameters, which fulfill the required quality of point cloud coordinates. The conventional LiDAR system calibration procedures have required full access to the raw measurements from the system components such as GPS/INS and laser scanner as well as the use of control data. This research focuses on developing alternative methods which can overcome the limited access to the system raw measurements and control data, and studying the optimal flight configuration for the LiDAR system calibration. In this regard, two approaches are considered. The first approach which is called the 'simplified method' estimates biases in the system parameters using only point cloud coordinates from parallel overlapping strips. In this method, the LiDAR geo-referencing equation is simplified with assumptions such as relatively flat terrain and parallel trajectory lines. The discrepancies between overlapping strips are represented by a 3D transformation function based on the simplified LiDAR geo-referencing equation. The second approach is the 'quasi-rigorous method'. It utilizes the platform position data with time-tagged point cloud. The use of the platform position data makes it possible to handle non-parallel and non-straight overlapping strips and

height variation of object surfaces. In the quasi-rigorous method, lateral and vertical distances between the laser firing point and object surface can be approximately estimated using trajectory position data and time-tagged point cloud coordinates; then, encoder angles (which indicate laser beam directions) are derived using these estimates.

1.2.2   Establishment of Correspondence between Point Cloud Datasets

Corresponding features between overlapping strips (as well as LiDAR strips and control data) are required to estimate the system parameters using the discrepancies between the conjugate surface elements caused by bias-contaminated point cloud coordinates. It is commonly known that it is almost impossible to identify distinct points in a LiDAR point cloud. In that sense, linear and areal features can be utilized as alternative primitives for the point cloud. The disadvantages of these alternative primitives are that they are mainly available in areas with man-made objects and pre-processing is required in order to extract them (e.g., plane segmentation and neighboring plane intersection). Instead of distinct features, surface matching procedures can be considered to establish correspondences between various point clouds. The surface matching techniques for 3D data have been addressed by many authors (Besl and McKay, 1992; Zhang, 1994; Bergevin et al., 1996; Park and Subbarao, 2003; Gruen and Akca, 2005). The most commonly implemented method is the 'Iterative Closest Point (ICP)'; it has been widely used as a method for 3D point cloud registration without identifiable landmarks. In this research, a modified approach named the 'Iterative Closest Patch' is used, where the corresponding features are defined by the closest point and patch, while the conventional ICP procedure assumes point-point correspondences. For the ICPatch procedure, the

normal distance between the matched point and planar patch is minimized, while the Euclidean distance between conjugate points is minimized in the ICP procedure. This research introduces two approaches for the similar measure between the matched point-patch pairs. In the volume constraint, the volume of the tetrahedron consisting of the matched point and triangular patch are utilized as a constraint. Another approach, a point-based similarity measure, derives pseudo-conjugate points from matched point-patch pairs. In this approach, the weight matrix for the pseudo-conjugate points should be modified to minimize the normal distances between matched point-patch pairs by assigning zero-weight along the corresponding patch. The advantage of this approach is that one can handle point-patch pairs without an additional function representing the similarity measure such as normal distance between corresponding point and patch.

1.3 Dissertation Outline

The proposed methods for LiDAR system calibration and establishing correspondences between point cloud dataset are introduced in this dissertation. The structure of this document and brief explanations of the chapters can be summarized as follows:

- Chapter 2 presents an overview of the LiDAR system and error sources. In addition, a literature review of existing LiDAR system calibration methods and point cloud registration techniques is also conducted.

- Chapter 3 introduces the proposed LiDAR system calibration methods. Two alternative calibration methods are discussed; the first one is the simplified method using only point cloud coordinates from parallel strips to estimate biases in system

parameters; the second one is the quasi-rigorous method which can deal with non-parallel strips using time-tagged laser footprints and trajectory data. In addition to the calibration procedures, point cloud adjustment procedures using the estimated biases are introduced for both methods.

- Chapter 4 details the co-registration methodology of point cloud datasets. The alternative primitives are introduced with the strategy of the similarity measure. Similarity measures between matched point-patch pairs are conducted using the volume constraints and modified weight matrices for both calibration procedures.

- Chapter 5 describes the experiments carried out using simulated and real datasets to demonstrate the feasibility and robustness of the proposed methodologies. The point clouds are reconstructed after estimating the biases in the system parameters. The adjusted point clouds are compared with the original datasets (before the calibration) in order to evaluate the impact of the system calibration.

- Chapter 6 summarizes the conclusions from the study of the proposed calibration methods and experimental results. Recommendations for future work follow the research conclusions.

CHAPTER 2

LITERATURE REVIEW

2.1 Introduction

Digital Surface Model (DSM) generation from LiDAR data has advantages in-terms of point density, positional accuracy, and production cost when compared to conventional photogrammetric procedures (Ackermann, 1999; El-Sheimy et al., 2005). In comparison to a radar system, a laser scanning system has favourable range measurements due to the use of higher energy pulses in shorter intervals and collimated light with shorter wavelength from a small aperture (Wehr and Lohr, 1999). A typical LiDAR system consists of a laser scanner and GPS/INS navigation components. The laser scanner mounted on the platform scans the object surfaces and produces a wide swath over which the distances to the mapped surface are measured. The distances from the sensor to the mapped surface are calculated by the time delay between the laser pulse transmission and detection while the onboard GPS/INS component provides the position and orientation of the platform. The laser beam direction (encoder angle) at which the laser is scanned is then measured. To account for the platform's movement, the motion of the platform is recorded by the GPS/INS navigation system and then the information is used in post-processing to calculate the coordinates of the point cloud.

The vertical accuracy of LiDAR data is relatively high (5-30 cm) compared to other methodologies, while the horizontal accuracy is about 30-50cm (McGlone et al., 2004; Alharthy, 2004). The quality of the LiDAR data is affected by many factors: accuracy of

the integrated GPS/INS position and orientation, validity of the system parameters, point density, flight altitude & speed, and amount and density of buildings & vegetation. The fundamentals and detailed principles of the laser ranging theorem was well documented by Baltsavias (1999a); Wehr and Lohr (1999), and the common method to determine the coordinates of LiDAR footprints was throughly explained by Vaughn et al. (1996); Shan and Toth (2009).

2.2   LiDAR Overview

The word laser means 'light amplification by stimulated emission of radiation'. Electrons in atoms can occupy many different energy levels. If energy is absorbed by an electron, it jumps to a higher energy level (orbit); it is called 'excited'; then, when the electron comes back to lower energy lever (where it was to get back to stable status), light is emitted. The light emission occurs at random, and thus has a low level of coherence. Stimulated Emission is what makes a laser different from the typical light created by a normal light source such as a bulb. In stimulated emission, an electron in a higher orbit is brought to a lower orbit by the presence of a photon of exactly the same energy as the energy difference between the two levels. When this happens, another photon is emitted which is identical to the first photon. Since two photons are identical, they add together to make the most intense wave possible. Amplifying the radiation in this way creates what is called coherent radiation, which is the most intense radiation possible (Bossler, 2010). Extensive literature has been published since the laser technology was invented by Charles Townes and Arthur Schawlow in Bell Labs in 1958. For further information

about laser, one can refer to various text books such as Hitz and et al. (1998); Weber (1999); Silfvast (2004).

The laser device, through the process described above, emits a coherent beam, which is monochromatic (typically with wavelength in the range from visible blue-green to near-infrared) and directional with less divergence compare to white light which travels in many directions and is very weak. A laser beam, however, is not perfectly cylindrical, refer to Figure 2.1. The waist is the narrowest part of the beam. From the waist, the beam diverges by an angle γ, which is known as the beam divergence angle and typically ranges from 0.2 to 1.0 mrad (Habib, 2006). For example, at a flight altitude of 1,000m, the diameter of the laser footprint is about 30 and 50cm for a beam divergence of 0.3 and 0.5 mrad, respectively (Shan and Toth, 2009). Therefore, the laser footprint should be thought of as a disc/ellipse rather than a distinct point. The size and the shape of the footprint depends on several factors such as the beam divergence angle, the distance between the laser beam firing point and the object, the look angle of the laser beam, and the orientation of the surface of the mapped object.
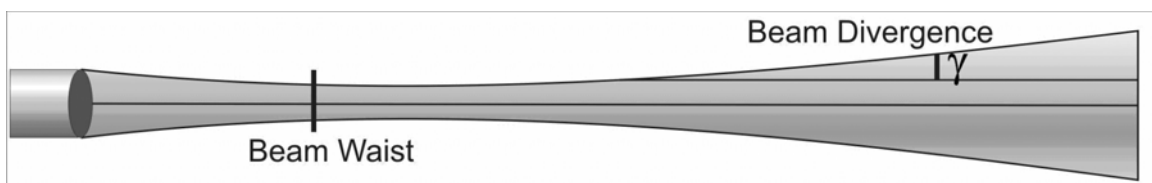
Figure 2.1. The divergence angle of a laser beam (Habib, 2006).

The ranging technologies using a laser can be classified into two groups: phase comparison method and time pulse method (Shan and Toth, 2009). In the phase comparison method, the ranging system transmits a continuous wave (CW) of laser

radiation. The ranges between the device and objects are determined by comparing the transmitted and received wave patterns. The laser ranging system using a CW is usually used in terrestrial LiDAR systems aiming to measure relatively short distances (typically less than 100m). The drawback of the CW system is that the phase difference between reflected and emitted signals is measured by comparing them, but the integer number of wavelengths cannot be determined by the signal difference. It is known as the ambiguity resolution problem, which is similar to the GPS carrier-phase ambiguity problem. In modern systems, the problem is solved by making many changes to the wavelength (Shan and Toth, 2009). Second, 'time pulse method' transmits discrete pulses instead of the CW and records time difference between transmitted and reflected pulses to determine the distance for the round trip (Baltsavias, 1999a; Wehr and Lohr, 1999). Usually, when the pulse is reflected from the specific targets such as grounds, buildings, and trees, the received pulses whose energy is higher than a predetermined threshold value can be detected. The detected pulse is recorded against the time between the signal emission and its reception in a graph, which is known as the waveform. Since the speed of light is accurately known, the accuracy of the laser range is dominantly affected by the quality of the time measurement. The ranging technology using the pulsed laser is common in airborne LiDAR systems commercially operated.

Some of recent LiDAR systems (e.g., Optech ALTM 3100, TopoSys Harrier 56/G4, RIEGL LMS-Q560, and LEICA ALS 50 II) are equipped with a full waveform digitiser. The full waveform digitising LiDAR systems have been developed, first as preparation for satellite systems to survey earth topography and vegetation cover, and later for airborne LiDAR systems (Hyyppä, 2004). An advantage of the full waveform system is

that the detection of the objects of interest can be processed after capturing LiDAR data to characterise the different targets along the path of the laser beam (Mücke, 2008). Depending on the nature of the mapped object, a portion of the laser light might penetrate that object (e.g., tree canopy). Penetrated energy might interact with other objects leading to several peaks in the waveform. Figure 2.2a illustrates a sample of full waveform where received signals are continuously recorded, and each peak indicates objects existing along the pulse path. Another advantage is that full waveform data is more useful than classical multi-echo LiDAR data since it can provide more than basic geometric information like 3D point clouds (Hug et al., 2004; Chauve et al., 2007). Figure 2.2b shows a profile captured by the LMS-Q5600. On the left side of this figure, the amplitudes of reflected signals are represented in the gray, while two waveform plots are shown on the right side. As one can see in this figure, the amplitude profile display and waveform plot "B" show two peaks indicating both roof and ground. Depending on the reflectances from the roof and ground, waveform data can be used to precisely determine the lateral position of the edge of the roof with sub-beam-diameter accuracy (Hug et al., 2004).

(a)

(b)
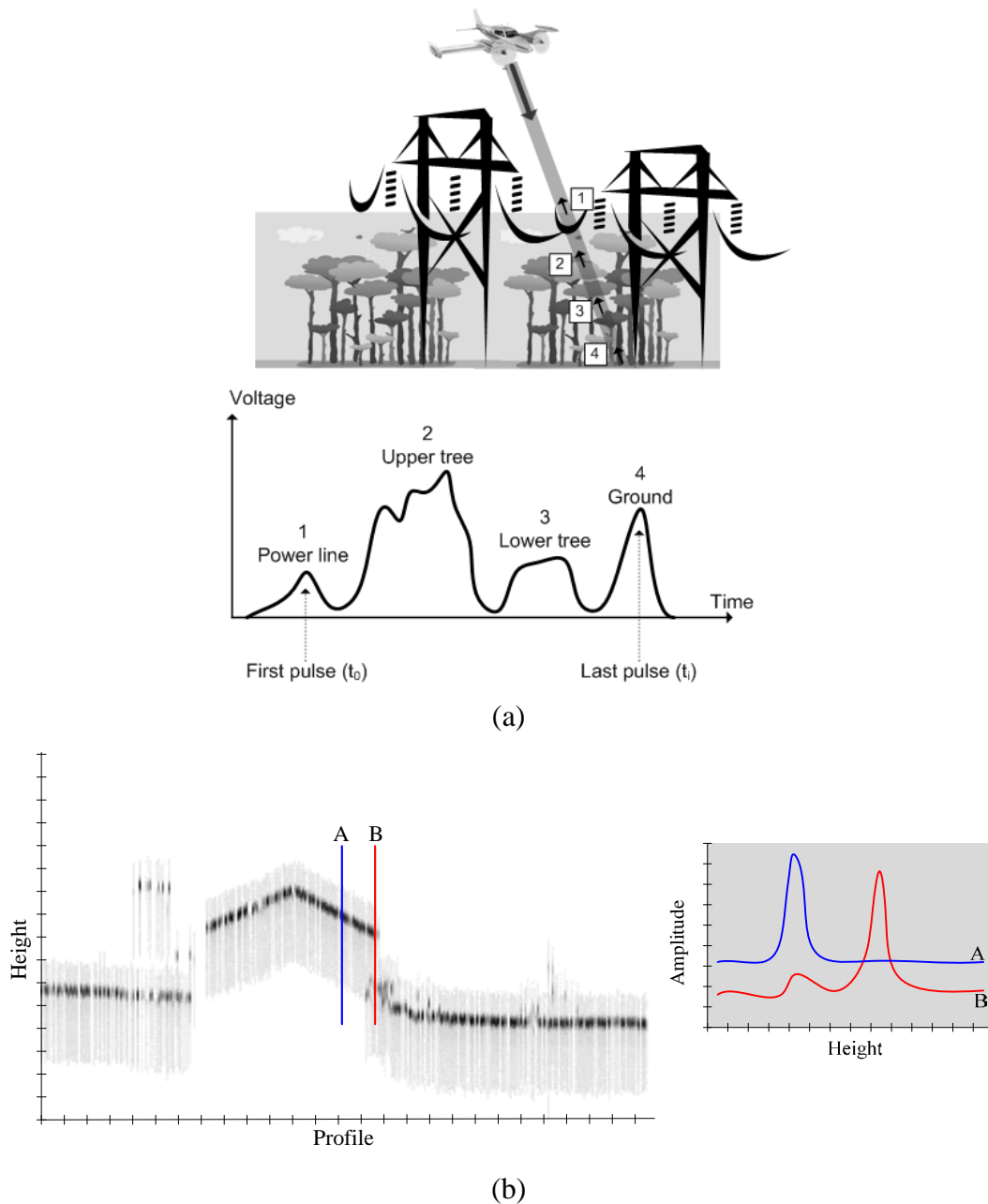
Figure 2.2. (a) Laser pulse interaction with objects and range derivation from the digitized waveform (Shan and Toth, 2009; Mallet, 2009; Bossler, 2010) and (b) a profile of full waveform data captured by the LMS-Q5600 (adapted from Hug et al., 2004).

LiDAR data is delivered in the form of *X*, *Y*, and *Z* ground coordinates of the captured surfaces, along with expected accuracies in the horizontal and vertical directions. The

system consists of three components: laser scanner, GPS, and INS, as illustrated in Figure

2.3. The laser scanner, GPS, and INS are mounted on a moving platform, and a GPS base

station is additionally operated for DGPS surveying. The laser scanner measures the

distances between the laser firing point and object points as well as laser beam directions

(represented by encoder angles). The coordinates of the object points are calculated using

the measurements after determining the laser scanner position and orientation. Since the

laser scanner is mounted on a moving platform such as fixed wing airplane, helicopter, or

van, the laser scanner position is directly geo-referenced by the GPS/INS navigation

system with respect to the ground coordinate system. Figure 2.4 shows some of the

LiDAR systems that are commonly used by the mapping industry.
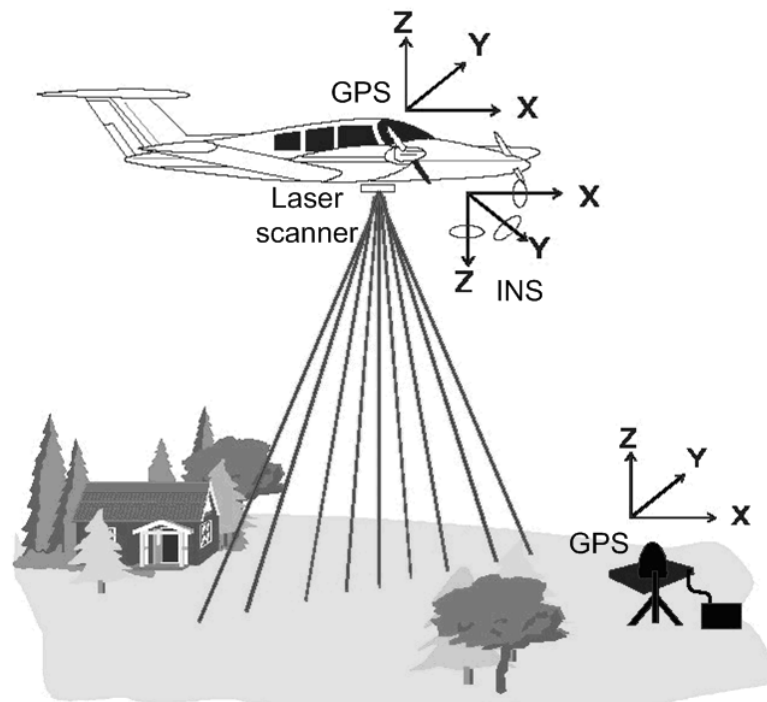
Figure 2.3. Basic components of a general LiDAR system.

http://www.leica-geosystems.com/en/Leica-ALS60-Airborne-Laser-Scanner_57629.htm

(a)

http://www.optech.ca/gemini.htm

(b)

http://www.rieglusa.com/products/airborne/lms-q680/index.shtml

(c)

http://www.toposys.com/pdf-ext/Engl/FalconIII-Handout-EN.pdf

(d)

Figure 2.4. Examples of LiDAR system equipment: (a) Leica ALS60, (b) OPTECH ALTM Gemini, and (c) RIEGL LMS-Q680i, and (d) TopoSys Falcon III.

In addition to the point positions, most modern LiDAR systems can provide intensity information which is the ratio between the strength of detected light (laser beam) and that of emitted light, and is influenced mainly by the reflectance properties of the object. The intensity data can be utilized for object extraction and land-cover classification (Song et al., 2002; Clode et al., 2004; Wang and Tseng, 2004). The intensity data has however serious noise, so that a filtering procedure is required before its use (Xudong et al., 2005). Figure 2.5 shows a range image (in the form of shaded relief) and an intensity image taken over the same area, illustrating the complementary information obtained from the

two types of data; those are interpolated to regular grid data derived from the original irregular point cloud.
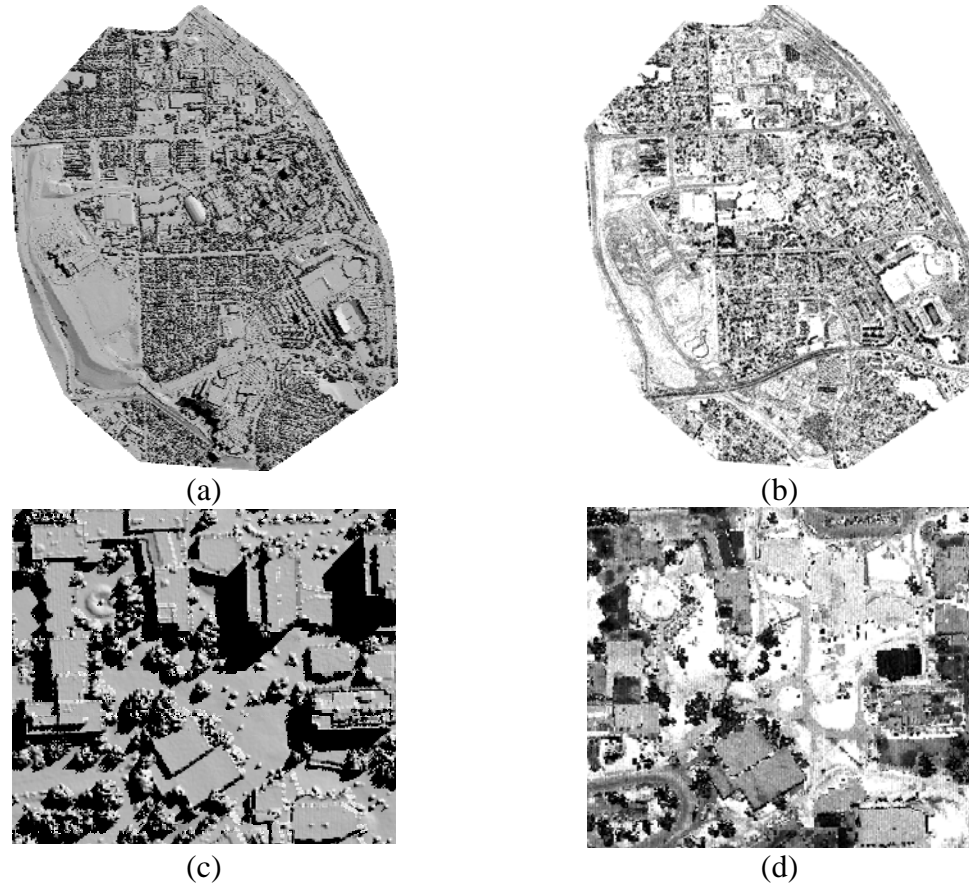
Figure 2.5. Sample LiDAR data: left two figures are interpolated range images (shaded relief) and right two figures are interpolated intensity images, over the same areas.

Table 2.1 presents the specifications of typical LiDAR systems. The typical wavelength of a LiDAR system is about 1,064 nm which falls in the infrared portion of the electromagnetic spectrum. Most objects on the ground have a reasonable reflectance at infrared wavelengths, so they produce a return signal with sufficient intensity to be detected. It is however known that water body, damp soil, and dark surfaces have very low reflectance; it is difficult to detect a signal reflected from these types of targets (Harding, 2004).

Table 2.1. Specifications of typical LiDAR systems (Habib, 2006; Bossler, 2010).

Specification	Typical values
Laser wavelength	1064 nm, near-infrared
Pulse rate	50-167 kHz
Pulse energy	100s μJ
Pulse width	10 ns
Beam divergence	0.25-2.0 mrad
Scan angle (or Field Of View)	40 °-75 °
Scan rate	25-90 Hz
GPS frequency	1-10 Hz
INS frequency	200-300 Hz
Operating altitude	80-3,500 m (6,000 m max)
Footprint size	0.25-2.0 m (at 1,000 m altitude AGL)
Number of returns	1-4 or full waveform
Ground spacing	0.5-2.0 m
Vertical accuracy	5-30 cm (at 1,000-3,000 m altitude AGL)
Horizontal accuracy	1/5,500-1/2,000 of flight attitude (m/AGL)

The pulse repetition rate indicates the number of emitted laser pulses per second. The scan rate, on the other hand, refers to the number of completed full scans per second. The density of a point cloud depends on the system and on the balance between flying speed, pulse rate, scan angle, and flight altitude (Ackermann, 1999). Higher pulse and scan rates require a lower flight altitude because there is a limitation in the capacity of a laser scanner power (Fugro EarthData, Inc., 2009). The swath width of a LiDAR strip is a function of the scan angle and flight altitude; for instance, 40° scan angle and 1,000m flight altitude lead to about 700m swath on the ground. The accuracy of GPS/INS

navigation is very important for deriving LiDAR points. The GPS error varies during the data capturing time; through integration of GPS with INS, the temporal variability can be smoothed. Typically, with DGPS and post-processing, accuracies of 5-15 cm can be achieved (Baltsavias, 1999a). The attitude accuracy of a platform is more important than the position accuracy, especially for a higher flight altitude, since the impact of the INS measurement quality on point cloud coordinates is a function of the flight altitude. The error budget of a LiDAR system will be further discussed in the next section.

The LiDAR scanning pattern on the ground is affected by the scanning device types as well as flight path and speed and the terrain topography. Figure 2.6 shows the scanning device types used in the commercial LiDAR systems: oscillating mirror, rotating polygon, nutating mirror (palmer scanner), and fiber scanner (Wehr and Lohr, 1999; Brenner, 2006; Shan and Toth, 2009). The oscillating mirror and rotating polygon produce linear scanning pattern; the oscillating mirror yields "zigzag" patterns (Figure 2.6a), while the rotating polygon has parallel lines on the ground (Figure 2.6b). Non-linear scanning pattern is available using the nutating mirror, which moves the laser beam along an elliptical path below the aircraft (Figure 2.6c). The advantage of the nutating mirror is that the ground is scanned twice from different directions (forward and backward); therefore, occluded areas in the forward scanning can be captured in the backward scanning (Mücke, 2008).
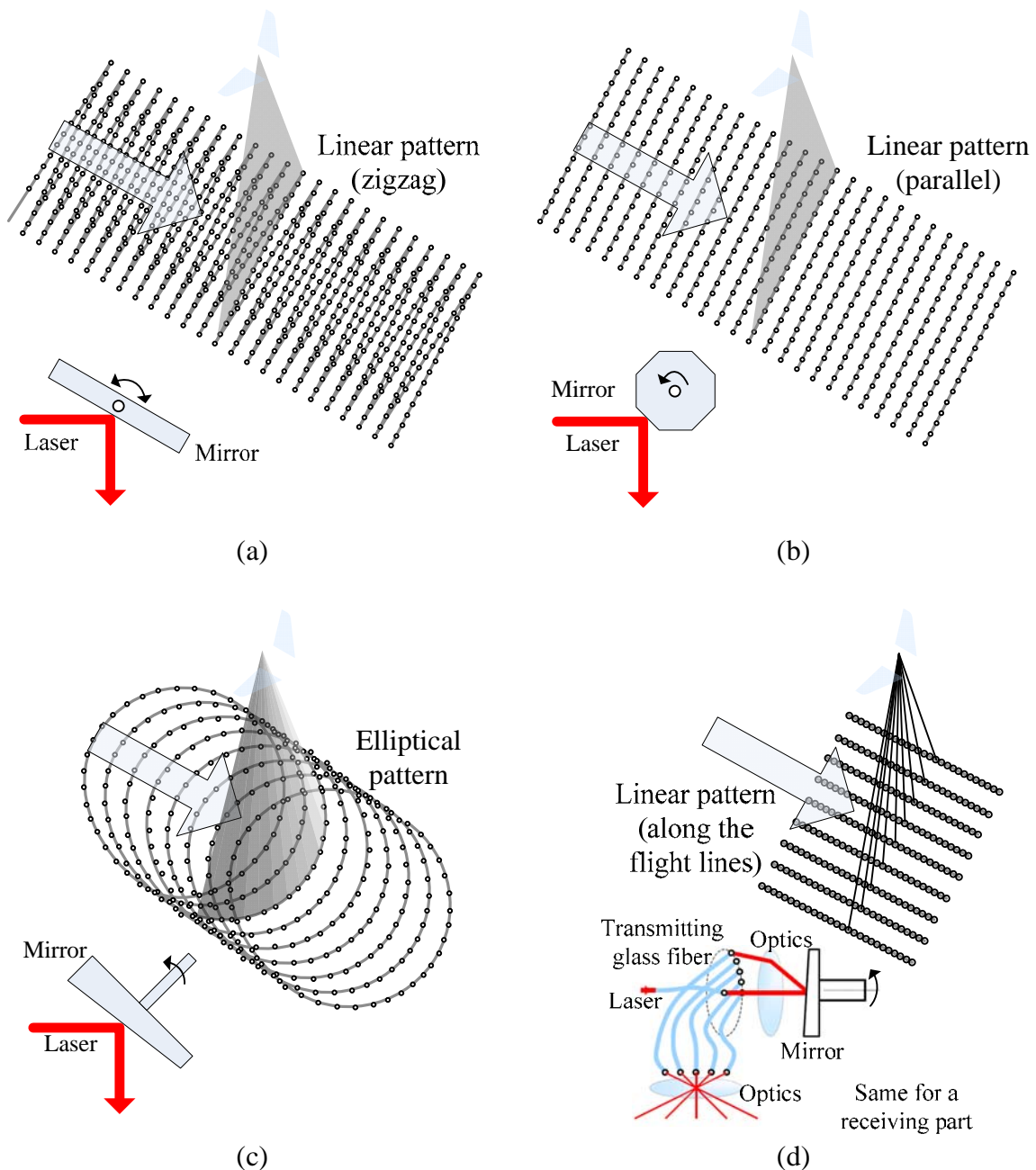
Figure 2.6. Scanning devices: (a) oscillating mirror, (b) rotating polygon, (c) nutating mirror, and (d) fiber based laser scanner (Brenner, 2006).

The fiber scanner consists of two arrays of glass fibers (transmitting and receiving arrays) which are arranged at one end in a circle and at the other end in a line. A laser is sent by a

motor-driven mirror into the circular glass fiber array, and linearly transmitted to the ground. The reflected laser from the ground is received by the receiving glass fiber; then, the laser is guided by another mirror into to a laser detector. The number of glass fibers determines the number of laser footprints across the flying direction (Figure 2.6d). The fiber scanner has an important advantage with respect to maintaining the stability of measuring laser beam directions because each glass fiber has a fixed beam direction (Schnadt and Katzenbeisser, 2004).

According to the reviews of the commercial LiDAR systems (Baltsavias, 1999b; Lemmens, 2009), the oscillating mirror and rotating polygon are the most popular. In other words, the linear scanning system is a majority from the point of view of the scanning pattern on the ground. For the oscillating mirror and rotating polygon, the required size of the mirrors is determined by the size of the transmitting and receiving aperture. The detection of the transmitted laser beam can be improved for a given laser power by enlarging the receiving aperture. A larger aperture means a larger mirror which needs more powerful devices to keep the speed of the mirror rotation fast, which is an engineering problem for designing the system (Shan and Toth, 2009).

The coordinates of the LiDAR footprints are the result of combining the derived measurements from each of its system components, as well as the boresight and lever-arm parameters relating to such components. The relationship between the system measurements and the parameters is embodied in the LiDAR geo-referencing equation represented in Equation 2.1 (Vaughn et al., 1996; Schenk, 2001; El-Sheimy et al., 2005; Shan and Toth, 2009). Four coordinate systems are used in the LiDAR geo-referencing

equation: mapping frame (ground coordinate system), Inertial Measurement Unit (IMU) body frame, laser unit frame, and laser beam frame (Figure 2.7). The position of the LiDAR footprint $\vec{X}_G$ can be determined in the mapping frame through the summation of three vectors ($\vec{X}_0$, $\vec{P}_G$ and $\vec{\rho}$) after applying the appropriate rotations coming from the platform attitude, laser beam directions, and boresight angles.

$$\underbrace{\vec{X}_G = \vec{X}_0 + R^m_{b\,(yaw,\,pitch,\,roll)}}_{\text{GPS/INS}}\left(\underset{\underset{\text{Lever-arm}}{\uparrow}}{\vec{P}_G} + \underset{\underset{\text{Boresight}}{\uparrow}}{R^b_{lu\,(\Delta\omega,\,\Delta\varphi,\,\Delta\kappa)}}\,\underbrace{R^{lu}_{lb\,(\alpha,\,\beta)}\begin{bmatrix}0\\0\\-\rho\end{bmatrix}}_{\text{Laser scanner}}\right) \tag{2.1}$$

In Equation 2.1, $\vec{X}_0$ is the vector between the origins of the mapping frame and the IMU body frame; $\vec{P}_G$ indicates the lever-arm which is defined by the spatial offset between the laser unit frame and the IMU body frame; and $\vec{\rho}$ is the laser range vector whose magnitude is equivalent to the distance from the laser firing point to its footprint. The term $R^m_{b\,(yaw,pitch,roll)}$ stands for the rotation matrix relating the mapping and IMU body frames; $R^b_{lu\,(\Delta\omega,\Delta\varphi,\Delta\kappa)}$ represents the rotation matrix defined by the boresight angles which are rotational offsets between the IMU and laser unit frames; and $R^{lu}_{lb\,(\alpha,\beta)}$ refers to the rotation matrix relating the laser unit frame and laser beam frame, which is determined by the laser beam direction through the encoder angles, α and β. In Figure 2.8, the Y_{lu} axis of the laser unit frame is parallel to the flying direction; α and β denote encoder angles around X_{lu} and Y_{lu} axes, respectively. For a linear scanner, which is the focus of this research, the laser beam direction can be represented by the encoder angle β (Figure 2.8a),

while the elliptical pattern requires both angles, α and β, to define the laser beam direction (Figure 2.8b). The involved quantities in the LiDAR geo-referencing equation are all measured during the acquisition process, except for the boresight and lever-arm parameters, which are usually determined through a calibration procedure.
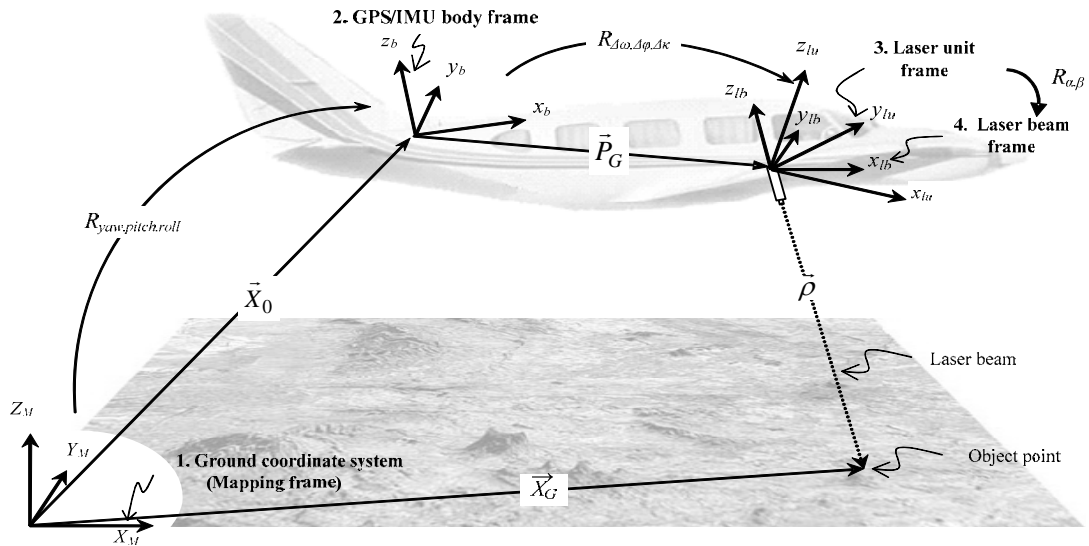
Figure 2.7. Observations included in a LiDAR system and the geometric relationship between them.
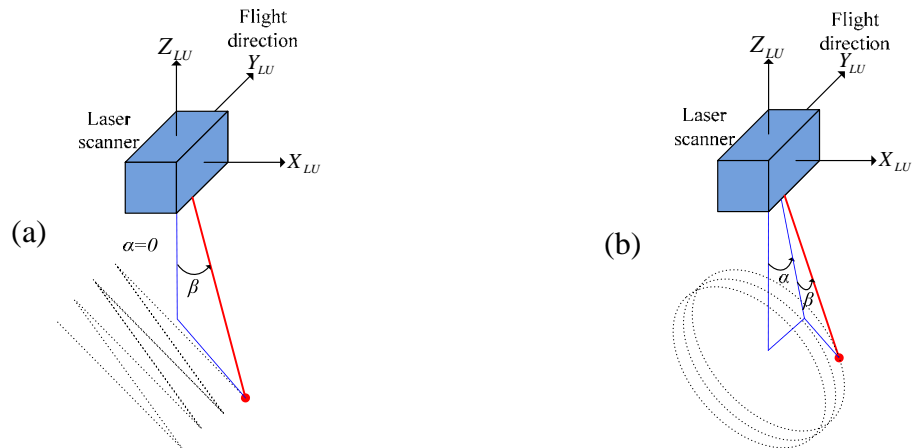
Figure 2.8. Linear and elliptical scanning devices: (a) the linear scanning device defines the laser beam direction using one rotation angle (typically across flight direction), while two rotation angles shown in (b) are used for the elliptical scanning device.

2.3   LiDAR Error Sources

There are two kinds of errors: random and systematic errors. The random errors are caused by the fact that repeated observations usually display a normal frequency distribution, while the systematic errors follow some physical law and thus can be predicted (Mikhail and Ackerman, 1976; Wolf and Ghilani, 1997). In the past, previous research has been done concerning the analysis of the accuracy and error sources in LiDAR systems: Huising and Gomes Pereira (1998), Baltsavias (1999a), Schenk (2001), and Glennie (2007); May and Toth (2007). The magnitude of the random errors depends on the precision of the system's measurements, which include the position and orientation measurements from the integrated GPS/INS, encoder angles, and laser ranges. The systematic errors, on the other hand, are mainly caused by biases in the boresight angles and lever-arm offsets relating the system components as well as biases in the system measurements such as encoder angles and laser ranges. In the following paragraphs, the random and systematic errors will be further discussed for a linear scanning device.

2.3.1   Random Errors

The purpose of studying the impact of random errors is to provide sufficient understanding of the nature of the noise in the derived point cloud as well as the achievable precision from a given flight and system configuration. The impact of random errors in the system measurements on the derived point cloud can be investigated by two approaches: the first approach based on a simulation procedure and the other approach using the law of error propagation. The simulation procedure starts from a given surface

and trajectory, which are then used to derive the system measurements (laser ranges, encoder angles, position and orientation information for each pulse). Then, noise is added to the system measurements, which are later used to reconstruct the surface through the LiDAR geo-referencing equation. The differences between the noise-contaminated and true coordinates of footprints are used to represent the impact of a given noise in the system measurements. The following list summarizes the effect of noise in the system measurements.

- Position noise will lead to similar noise in the derived point cloud. Moreover, the effect is independent of the system flight altitude and scan angle (Figure 2.9a).

- Orientation noise (platform attitude or encoder angles) will affect the horizontal coordinates more than the vertical coordinates within nominal scan angle ranges (e.g., $\pm 25°$). In addition, the effect is dependent on the system flight altitude and scan angle (Figure 2.9b).

- Noise in laser range mainly affects the vertical component of the derived coordinates (especially in the nadir region). The effect is independent of the system flight altitude. The impact, however, is dependent on the system's scan angle.

Through the proposed simulation, one can also notice that noise in some of the system measurements affects the relative accuracy of the derived point cloud. As an illustration, Figure 2.9 reveals that a given attitude noise in the GPS/INS derived orientation affects the nadir region of the flight trajectory less significantly than off nadir regions. Such a phenomenon is contrary to derived surfaces from photogrammetric mapping where the measurements noise does not affect the relative accuracy of the final product.
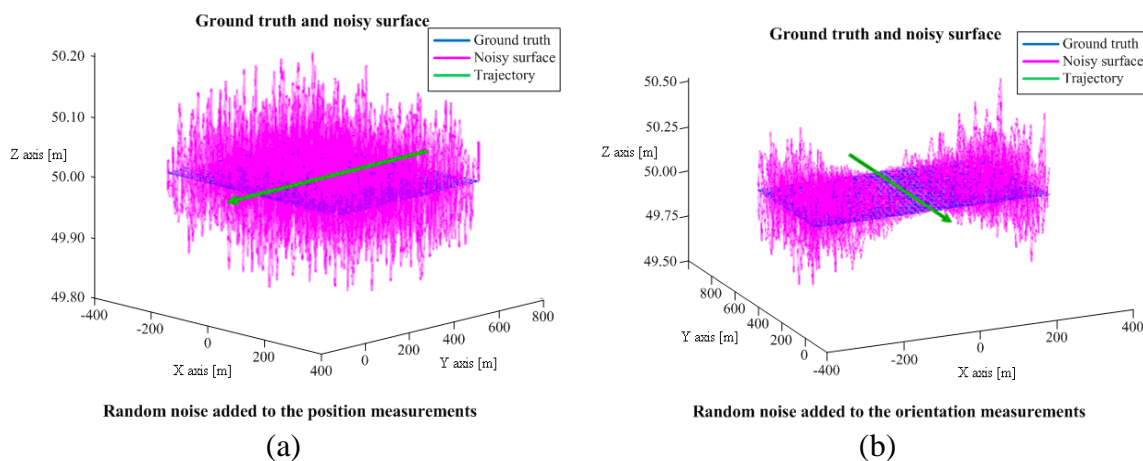
Figure 2.9. Effect of adding noise to the GPS/INS-derived position and orientation on the point cloud coordinates; (a) relative accuracy is not affected by the position noise, while (b) the attitude noise introduces relatively less errors along the LiDAR strip centre. The red lines show the noise-contaminated point positions compared to the true points in blue.

The second approach to studying the effect of random errors can be based on the law of error propagation applied to the LiDAR geo-referencing equation. Error propagation involves finding the stochastic characteristics of dependent variables given the characteristics of the independent variables and the functional relationships relating the two sets of variables (Mikhail and Ackerman, 1976). The fundamental and other applications of the law of error propagation (or propagation of variances and covariances) can be found in a few textbooks: Mikhail and Ackerman (1976); Wolf and Ghilani (1997); Koch (1999). For each of the LiDAR footprints, the law of error propagation can be used to estimate the precision of the derived coordinates, given the precision of the system measurements. The advantage of such a methodology is that it can estimate the "best achievable precision" from a given system and flight configuration. One should note that the use of the "best achievable precision" expression is based on the fact that the law of error propagation assumes a relatively flat and horizontal solid surface. In other

words, the precision of the derived point cloud covering steep and/or forested areas is not taken into consideration. To illustrate such a procedure for an operational system, Table 2.2 shows the expected precision of the measurements from two Optech LiDAR systems (ALTM 2050 and ALTM 3100). The manufacturer precision specifications for both systems are as follows: the horizontal precision is less than 1/2000 of the flight altitude in meters, while the vertical precision is roughly 15cm at a flight altitude of 1,200m, and roughly 25cm at a flight altitude of 2000 m (Optech, 2007).

Table 2.2. Precision specifications for the Optech system components (Applanix, 2007; Optech, 2007).

System model	GPS (m) Post-processed	IMU (°) Post-processed			Encoder angle (°)	Laser range (cm)
		Roll	Pitch	Yaw		
ALTM 2050	0.05 – 0.3	0.008	0.008	0.015	0.009	~ 2
ALTM 3100	0.05 – 0.3	0.005	0.005	0.008	0.009	~ 2

Using the law of error propagation and the specifications in Table 2.2, the expected precision of the derived LiDAR footprints is reported in Figure 2.10. It should be noted that the reported precisions in Figure 2.10 corresponds to LiDAR footprints at the swath edges and the centre of a scan-line (i.e., footprints with the maximum and minimum encoder angles). When comparing the manufacturer precision specifications with the numbers (horizontal and vertical accuracies) in Figure 2.10, one can see that the manufacturer precision specifications are more conservative than the calculated precision using error propagation which assumes relatively flat and solid surfaces without the consideration of vegetation and atmospheric effects. It is commonly known that the horizontal accuracy of data derived from photogrammetric systems is better than its vertical accuracy, while the vertical accuracy of LiDAR data surpasses the horizontal

accuracy. One can confirm this fact in this error propagation test; in Figure 2.10, the worst value of the vertical accuracy is 16 cm and the worst horizontal one is more than 50 cm.
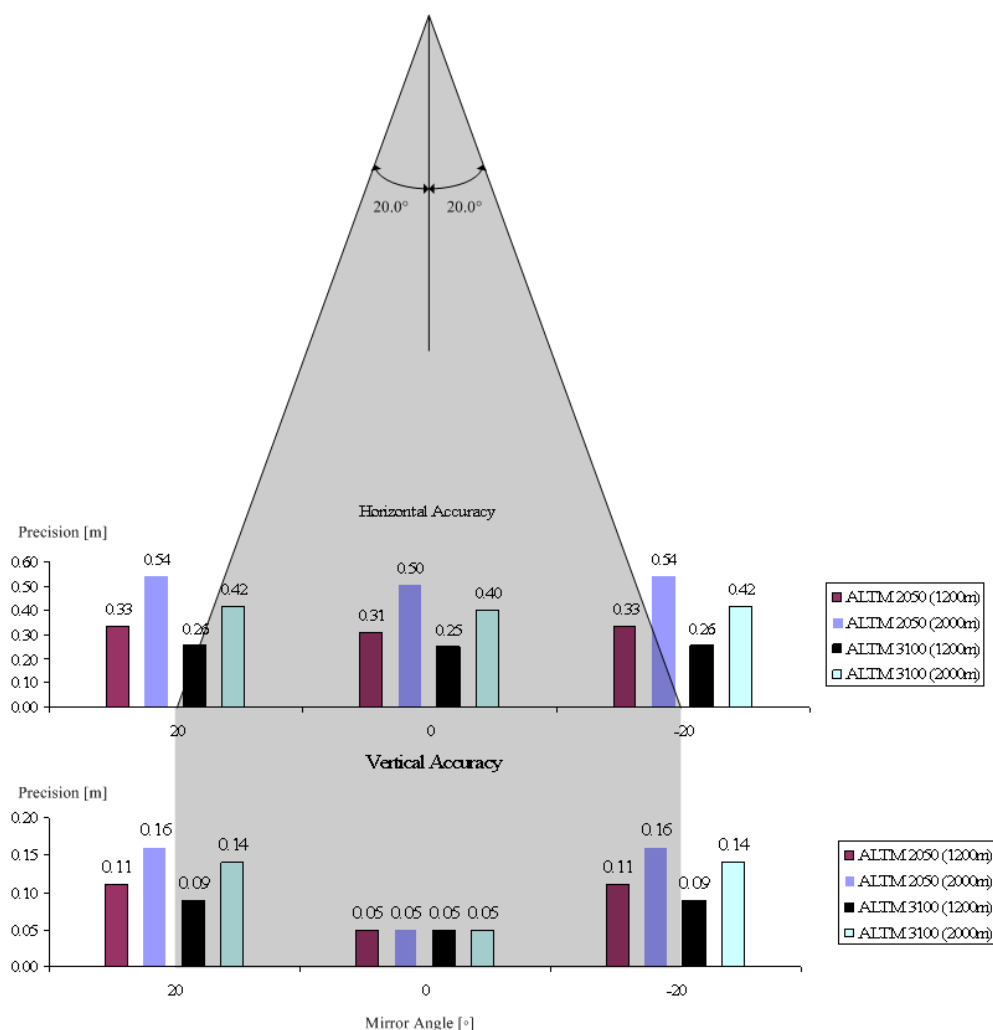
Figure 2.10. Expected precision of laser footprints is calculated by the law of error propagation at the centre and edge of a LiDAR swath using the system specifications in Table 2.2.

2.3.2 Systematic Errors

Systematic biases in the system measurements (e.g., encoder angles and laser ranges) and system parameters (e.g., boresight angles and lever-arm offset relating the system

components) will lead to systematic errors in the derived point cloud. The impact of these biases can be either derived through mathematical analysis of the LiDAR geo-referencing equation or by using a simulation process. The simulation process starts with a given surface and trajectory, which are then used to derive the system measurements (ranges, encoder angles, position and orientation information for each pulse). Biases are then added to the system parameters and measurements in order to generate a bias-contaminated point cloud which is compared with the true surface introduced in the simulation procedure for the analysis of the impact of the systematic errors. In order to evaluate the compatibility of overlapping strips and study the impact of the flight directions, two strips (forward and backward directions) are simulated. In this simulation test, a flat terrain is assumed; biases in boresight, lever-arm, range measurement, and encoder angle scale factor are introduced. For more detail about the flight specifications and systematic errors introduced in the simulation procedure, refer to Table 2.3.

Figure 2.11 shows the result of the simulation data test. In this figure, the graphs in the left column represent the coordinate errors (ΔX, ΔY, and ΔZ) along the scan-line caused by the biases in the system parameters for both forward and backward strips, where the flight directions are parallel to the Y axis and scanning directions are across the flight direction (X axis). On the other hand, the right column graphically illustrates the impact of the systematic biases on the ground, where $\delta\Delta X$, $\delta\Delta Y$, and $\delta\Delta Z$ are the biases in lever-arm offset; $\delta\Delta\omega$, $\delta\Delta\varphi$, and $\delta\Delta\kappa$ are the biases in boresight angles; δS, and $\delta\Delta\rho$ denote the biases of the encoder angle scale factor and range measurement, respectively.

Table 2.3. Description of the simulation data used for evaluating the impact of biases in the system parameters.

Parameters		Values
Flight direction (heading)		Along the ground Y axis
Platform attitude (roll and pitch)		roll = pitch = zero (level scanning)
Flight altitude		550m
Scan angle		20°
Lever-arm	Bias along X axis	0.1m
	Bias along Y axis	0.2m
	Bias along Z axis	0.3m
Boresight	Bias in pitch angle	50"
	Bias in roll angle	50"
	Bias in yaw angle	50"
Bias in encoder angle scale factor		0.001
Bias in laser range measurements		0.5m
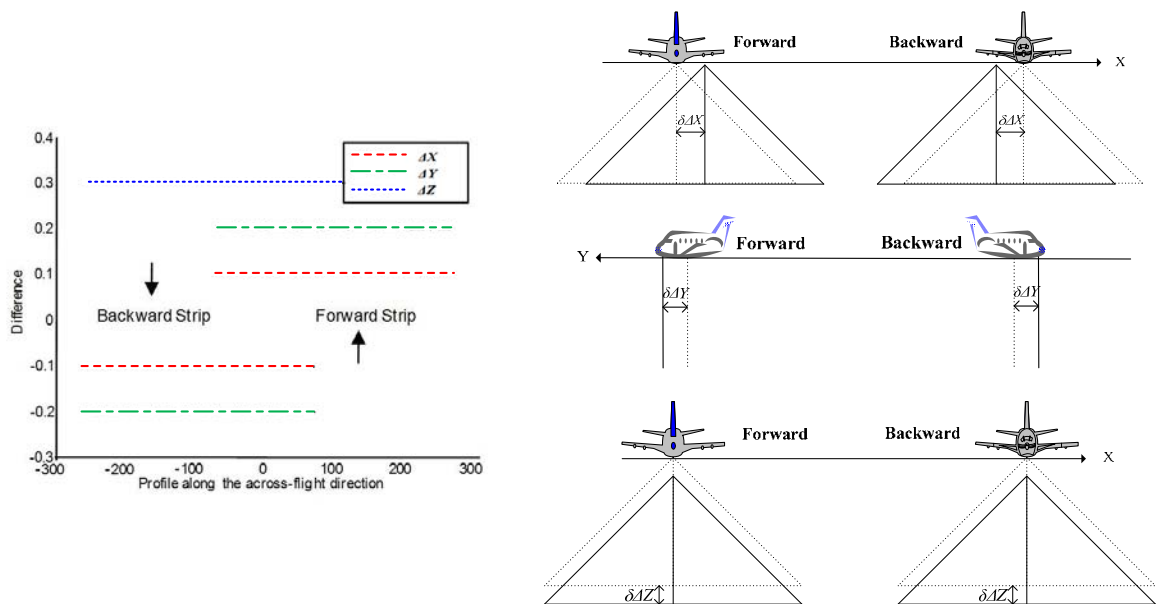
(a) Impact of biases in lever-arm components
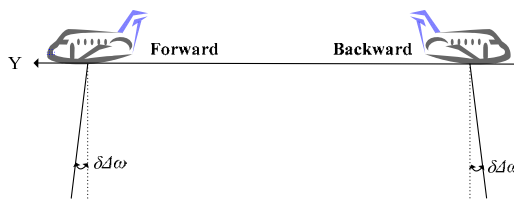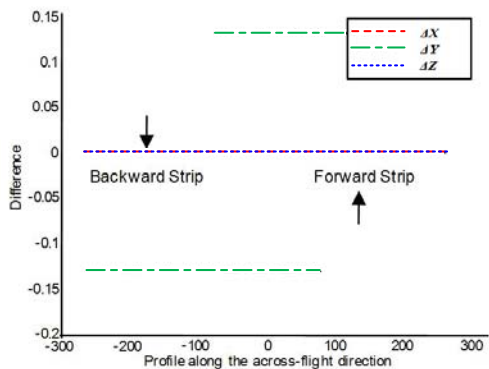
(b) Impact of bias in boresight pitch angle
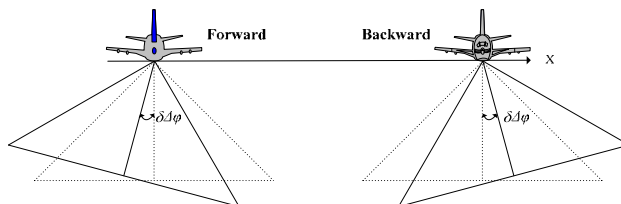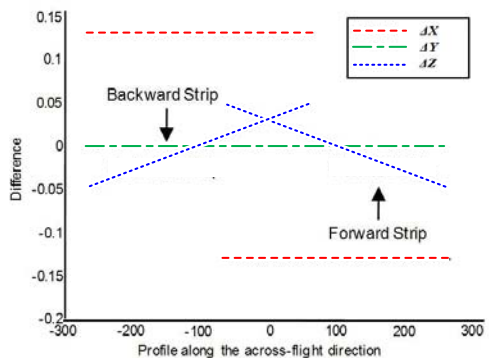
(c) Impact of bias in boresight roll angle
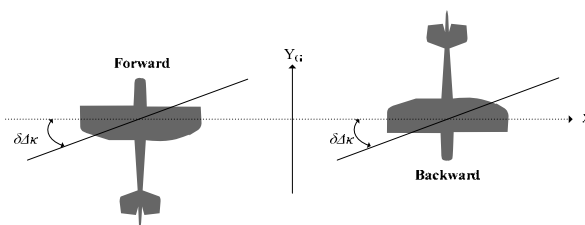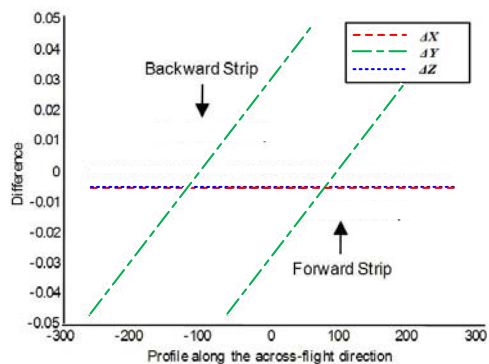
(d) Impact of bias in boresight yaw angle
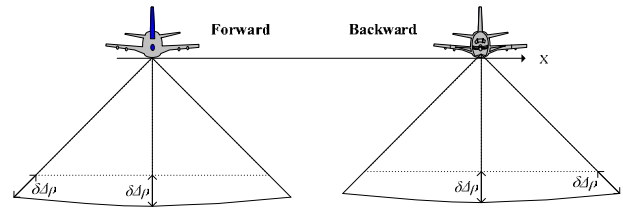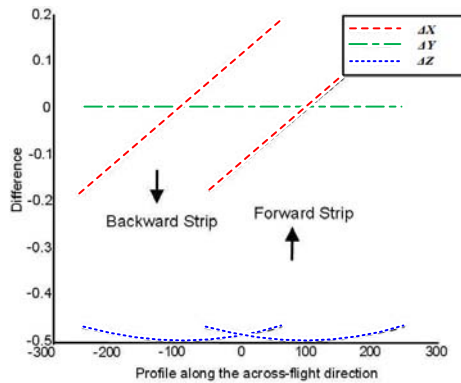
(e) Impact of bias in range measurement
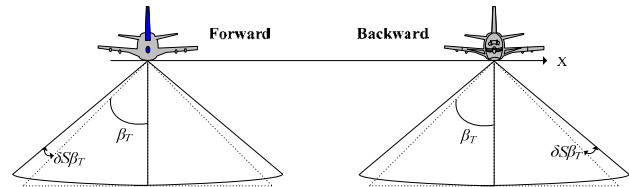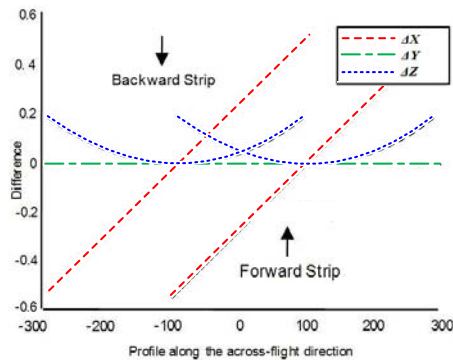
(f) Impact of bias in encoder angle scale factor

Figure 2.11. Differences between the bias-contaminated and true coordinates of the footprint for two overlapping strips flown in opposite directions: (a) impact of biases in lever-arm components, (b) impact of bias in boresight pitch angle, (c) impact of bias in boresight roll angle, (d) impact of bias in boresight yaw angle, (e) impact of range bias, and (f) impact of encoder angle scale bias.

The impacts of the biases in the lever-arm parameters are represented in Figure 2.11a; it can be seen that the errors caused by the biases ($\delta\varDelta X$, $\delta\varDelta Y$, and $\delta\varDelta Z$) in the lever-arm parameters are constant along the scan-lines, and there is no difference between forward and backward strips in Z coordinates. In a similar way, the impacts of biases in the boresight pitch, roll, and yaw angles are shown in Figures 2.11b, 2.11c, and 2.11d,

respectively. The impact of the bias ($\delta\Delta\omega$) in the boresight pitch angle causes constant discrepancies between forward and backward strips in the flight direction (Figure 2.11b). On the other hand, Figure 2.11c shows the impact of the bias ($\delta\Delta\varphi$) in boresight roll angle which causes errors across the flight direction (ΔX) as well as the vertical direction (ΔZ). However, there is no error along the flight direction (ΔY). In Figure 2.11c, even though the errors (ΔX) across the flight direction slightly changes along the scan-lines, it looks constant because the variation of the errors is small enough to be ignored. The bias ($\delta\Delta\kappa$) in the boresight yaw angle causes errors along the flight direction (ΔY) whose magnitudes are dependent on encoder angles, while the errors across the flight direction (ΔX) are close to zero and no error takes place in vertical direction (ΔZ) (Figure 2.11d). Figures 2.11e and 2.11f show the impact of the biases ($\delta\Delta\rho$ and δS) in the range measurement and scale of encoder angle, respectively. The Z coordinate errors caused by both biases have curved shapes along the scan-lines. The errors in the vertical coordinates (ΔZ) caused by the bias in the scale are zero in the centres of the scan-lines, while the errors caused by the bias in the range measurements are maximized there. The errors in the across flight direction (ΔX) caused by both the biases change along the scan-line, while there is no error caused by the biases along the flight direction (ΔY). The impact of the various systematic biases of a LiDAR system on the ground may depend on the flight direction (forward and backward), flight altitude, and encoder angle. Table 2.4 summarizes the impact of the biases with respect to those factors, and it will be discussed in more details in section 3.2 in terms of mathematical analysis.

Table 2.4. Summary of the impact of biases in the parameters and measurements of a LiDAR system with a linear scanner on the derived point cloud.

	Flight altitude	Flight direction (forward/backward)	Encoder angle (across flight direction)
Biases in lever-arm components	● Effect is independent of the flight altitude.	● Planimetric effect is dependent on the flight direction. ● Vertical effect is independent of the flight direction.	● Effect is independent of the encoder angle.
Bias in boresight pitch angle	● Effect is dependent on the flight altitude.	● Planimetric effect along the flight direction is dependent on the flight direction.	● Effect is independent of the encoder angle.
Bias in boresight roll angle	● Planimetric effect across the flight direction is dependent on the flight altitude. ● Vertical effect is independent of the flight altitude.	● Planimetric effect across the flight direction and vertical effect are dependent on the flight direction.	● Planimetric effect across the flight direction is independent of the encoder angle. ● Vertical effect is dependent on the encoder angle.
Bias in boresight yaw angle	● Effect is independent of the flight altitude.	● Planimetric effect along the flight direction is independent of the flight direction.	● Planimetric effect along the flight direction is dependent on the encoder angle.
Bias in laser range measurements	● Effect is independent of the flight altitude.	● Planimetric effect across the flight direction and vertical effect are independent of the flight direction.	● Planimetric effect (D_X) across the flight direction and vertical effect (D_Z) are dependent on the encoder angle (D_X more than D_Z).
Bias in encoder angle scale factor	● Effect is dependent on the flight altitude.	● Planimetric effect across the flight direction and vertical effect are independent of the flight direction.	● Planimetric effect across the flight direction and vertical effect are dependent on the encoder angle.

2.4 LiDAR System Calibration

The systematic errors contained in laser footprints come from biases in system parameters; those are biases in individual sensor measurements and mis-alignment of the sensors when mounted on a platform. The research in recent years has identified systematic biases and improved the quality of the LiDAR data, which can be classified into strip adjustment and LiDAR system calibration. The strip adjustment improves the quality of acquired overlapping strips by detecting and reducing discrepancies in the considered strips, while the LiDAR system calibration determines systematic errors to ensure the positional accuracy of laser footprints.

In the past few years, the strip adjustment has been developed for evaluating and/or improving the positional accuracy of LiDAR by checking the compatibility of laser footprints in overlapping strips (Kilian et al., 1996; Crombaghs et al., 2000; Maas, 2000; Bretar et al., 2004; Vosselman, 2002; Pfeifer et al., 2005). In Crombaghs et al. (2000), a method for reducing vertical discrepancies between overlapping strips is proposed. Since the horizontal quality of the derived point cloud is considerably lower than the vertical one, this approach is not sufficient to evaluate the overall quality of the LiDAR data. In Kilian et al. (1996), an adjustment procedure similar to the photogrammetric block adjustment was introduced for detecting discrepancies and improving the compatibility between overlapping strips. In that research, twelve parameters were considered: six constant offsets and six time-dependent drifts for positions and orientations, which are estimated using tie and control points for each strip. However, the independent parameter set for each strip does not meet the ultimate goal of the LiDAR system calibration

because the estimated parameters cannot be assumed to be valid for other strips which are not involved in the adjustment procedure. Another drawback of this approach is that it relies on distinct points such as building corners to relate overlapping LiDAR strips and control surfaces. Due to the irregular nature of the LiDAR footprints (which is caused by the scanning pattern, terrain relief, flying speed), the identification of landmarks (e.g., building corners) is quite difficult and not reliable.

More appropriate primitives have been suggested by Maas (2000), where the correspondence is established between discrete points in one LiDAR strip and Triangular Irregular Network (TIN) patches in a second strip. The correspondences are derived through a least-squares matching procedure where normal distances between conjugate point-patch pairs are minimized. The drawback of this work is that simple shifts were used as the transformation function relating conjugate point-patch pairs, and the validity of such a model was not completely justified. Moreover, the estimated shifts were not used to derive an indication of the point cloud quality. Vosselman (2002) estimated the offset between overlapping strips using linear features extracted from interpolated surface data, where the linear features were gathered from gable roofs and ditches. Pfeifer et al. (2005) developed a method using plane segmentation instead of using points, linear features, or TIN patches. In this research, planar patches were extracted using normal vector computation and region growing in overlapping strips. Bretar et al. (2004) proposed an alternative methodology for improving the quality of LiDAR data using derived surfaces from photogrammetric procedures. The main disadvantage, which limits the practicality of this methodology, is relying on the availability of aerial imagery over the same area. In addition, the proposed approach uses an affine transformation to relate

LiDAR and photogrammetric surfaces; however, there was not sufficient justification of the use of the affine transformation. The abovementioned approaches focused on the detection and elimination of the discrepancies between overlapping strips. Even though the discrepancies are caused by systematic errors in a LiDAR system, the strip adjustment procedures cannot be used for estimating biases in the system parameters.

On the other hand, LiDAR system calibration determines the system parameters based the models defined by the biases in the individual sensor measurements and mounting parameters to ensure the positional accuracy of the final product of a LiDAR system. Schenk (2001) introduced the sources of systematic errors that can occur in a LiDAR system. A calibration procedure was then proposed using such an analysis. This work comprehensively explained possible errors in LiDAR systems; however, it is not recommended to include all possible systematic errors as unknown parameters in an adjustment procedure due to the high correlation between some parameters (Vosselman, 2002). For example, if the biases in scanner encoder angles and boresight parameters are considered simultaneously in a calibration procedure, it will cause a nearly singular normal matrix. Burman (2000) estimated boresight and lever-arm parameters using elevation and intensity discrepancies between overlapping strips. This approach needs encoder angles and distance measurements as well as point cloud coordinates, and an interpolation procedure is required for the generation of regular grid data which is used to calculate topographic slope and intensity gradient of a point in question. This approach was implemented in "TerraMatch" which is one of the commercial LiDAR software packages (Burman, 2002). The discrepancies between overlapping strips were also used in Toth (2002); where boresight parameters were automatically determined using the

discrepancies between corresponding points, which were derived by the least square matching, without control data and system raw measurements. In this approach, the navigation data for the strips are required to estimate laser firing points. However, it is possible to estimate more than the firing points using trajectory information as it will be discussed in the section introducing the proposed methods. The method introduced by Morin (2002) used the discrepancies between overlapping strips to solve the boresight angles and the scanner torsion. These parameters are either estimated using ground control points or by manually observing discrepancies between tie points in overlapping strips. This approach is faced with an important issue; the identification of distinct points in LiDAR is difficult due to the irregular nature of point cloud data. In addition, this approach is not free from the need of the laser scanner and GPS/INS measurements.

Instead of points and linear features, surface patches have been used as alternative primitives. Filin (2003) recovered systematic errors such as boresight and range bias using natural surfaces represented by a set of planar patches. This approach estimates systematic errors by minimizing the normal distances between laser points and control surfaces. The limitation of the approach is that system raw measurements are required as well as a control surface. Skaloud and Lichti (2006) presented a calibration technique using tie planar patches. The underlying assumption of this approach is that systematic errors in the LiDAR system will lead to non-coplanarity of conjugate planar patches as well as bending effects in these patches. This calibration method can simultaneously solve for the plane parameters and boresight angles which are considered as unknowns in the integration of LiDAR geo-referencing and plane equations. In addition, the range bias can be estimated using vertical control surface. However, this approach requires

relatively large planar patches, which might not always be available when the LiDAR data is captured in rural areas. According to Burman (2000); Skaloud and Lichti (2006); and Habib et al. (2007), if the boresight and lever-arm parameters are considered at the same time, one of the difficulties is the correlations between those parameters. Therefore, the use of planar patches should be carefully handled through the use of an optimal flight plan, as well as optimal planar patch distribution due to the correlations between these system parameters (Habib et al., 2007).

Since Ackermann (1999) introduced the potential integration of imaging and laser sensors, research has been performed to investigate the potential and limitations of the integration of LiDAR and photogrammetric data and their complementary nature. For example, Postolov et al. (1999) and Ghanma (2006) introduced the co-registration between LiDAR and photogrammetric data, and Bretar (2004) generated a DSM from photogrammetric data which was then compared LiDAR data for the strip adjustment. Habib et al. (2007) used planar patches derived from photogrammetric data for the LiDAR system calibration, where the photogrammetric bundle adjustment was augmented by adding the LiDAR geo-referencing equation to the collinearity equations using the LiDAR system raw measurements. In that approach, the LiDAR boresight angles are determined by minimizing the normal distances between the derived LiDAR footprints and the photogrammetric areal patches. In addition to the estimation of the boresight angles, that methodology also ensures the co-registration between the photogrammetric and LiDAR data to a common reference frame, which has a positive impact on later products such as ortho-photos and photo-realistic 3D models. The

drawback of this approach is the need for laser scanner and GPS/INS measurements and photogrammetric data captured over the same area as the LiDAR data.

The calibration approaches taken by LiDAR surveying companies are empirical. For example, the method proposed by Jung and Lee (2006) requires a calibration site where well-known features such as building edges and flat surfaces in run-ways are available. Discrepancies between a point cloud and control features are manually observed and used to determine the system parameters such as the boresight roll angle, pitch angle, height offset, and laser range measurement scale. This approach is a sequential approach rather than a procedure based on least square adjustment. The limitations of the method are the need for well defined calibration sites and manual procedures. In addition, the heading angle, one of the important system parameters, is not considered in this calibration procedure.

Even though various approaches for LiDAR system calibration have been introduced to date, there is still no standard calibration method. For example, the systematic error factors under consideration are not consistent, and Table 2.5 shows which error factors have been considered by each author in the previous research. The lever-arm offsets are sometimes ignored, while the boresight angles are considered by most authors. In addition, the offset and scale of laser range measurements and encoder angles are rarely considered. The considered systematic errors in the LiDAR system are presented in Table 2.5; however, one should notice that it does not mean that all considered factors are accounted for in the LiDAR calibration procedure at the same time. Even though some systematic errors are discussed as error sources, the analytical procedure of the LiDAR

system calibration is complex and difficult because of the correlation between the considered parameters. The last row of Table 2.5 shows the systematic errors considered in this research: boresight angles, lever-arm offsets, laser range offset, and encoder angle scale factor. Chapter 3 will introduce the proposed methods which can estimate the biases in the considered system parameters at the same time.

Table 2.5. LiDAR systematic errors considered in the previous research.

Proposed by	Considered systematic errors									
	$\Delta\omega$	$\Delta\varphi$	$\Delta\kappa$	ΔX	ΔY	ΔZ	$\Delta\rho$	S_ρ	$\Delta\beta$	S_β
Baltsavias (1999a)	●	●	●	●	●	●	●		●	
Morin (2000)	●	●	●							●
Burman (2000)	●	●	●	●	●	●				
Schenk (2001)	●	●	●	●	●	●	●	●	●	●
Toth (2002)	●	●	●							
Filin (2003)	●	●	●				●			
Skaloud and Lichti (2006)	●	●	●				●			
Jung/Lee (2006)	●	●				●		●		
Habib et al. (2007)	●	●	●	●	●	●				
This research	●	●	●	●	●	●	●			●

where,

$\Delta\omega$, $\Delta\varphi$, and $\Delta\kappa$ are boresight angles,

ΔX, ΔY, and ΔZ are lever-arm offset components,

$\Delta\rho$ and S_ρ are bias and scale of laser range measurements, and

$\Delta\beta$ and S_β are range bias and scale factor of encoder angles of a laser scanner, respectively.

CHAPTER 3

ALTERNATIVE LIDAR CALIBRATION METHODOLOGIES

3.1 Introduction

The 3D coordinates of point cloud generated by a LiDAR system are directly geo-referenced due to the use of a navigation system consisting of GPS and INS, and a laser scanner onboard a platform. The accuracy of the point cloud coordinates is affected by inherent systematic and random errors in a LiDAR system. The achievement of the full potential accuracy requires the elimination of all systematic errors. In this research, system parameters, which include mounting parameters (lever-arm and boresight) and systematic errors in a laser scanner (encoder angle scale factor and laser range bias), are estimated using point cloud coordinates of overlapping strips. Two alternative calibration methods are introduced for the determination of biases in the system parameters. Those methods can overcome the limitations of existing calibration procedures in terms of requirements of raw LiDAR data. The first presented method, denoted as the "simplified method", makes use of the LiDAR point cloud from parallel overlapping strips captured over an area with moderately varying elevation. The systematic biases are estimated using the identified discrepancies between conjugate primitives in overlapping LiDAR strips. The second method denoted as "quasi-rigorous method" can deal with non-parallel strips over rugged terrain, but requires time-tagged LiDAR point cloud and navigation data (trajectory position).

3.2 Simplified Method

The simplified method is designed to work with parallel LiDAR strips captured over an area with moderately varying elevation. It requires only the LiDAR point cloud and the system biases are estimated using the detected discrepancies between overlapping LiDAR strips. More specifically, this calibration method consists of a two-step procedure. First, the discrepancies between parallel overlapping strips are determined. Second, the system biases are estimated using the detected discrepancies between the strips.

In the simplified method, the following assumptions are considered in the mathematical derivation: (i) linear scanning systems are considered, (ii) variations in the object space elevations are much smaller than the flight altitude, (iii) the flight lines are parallel, (iv) the platform trajectory is straight, (v) we are dealing with an almost levelled scanner (i.e., the roll and pitch angles are small enough to be ignored), and (vi) the boresight angles are assumed to be very small. In addition, an additional coordinate system defined in the centre of the overlapping area is introduced. Figure 3.1 shows the user defined coordinate system; its Y axis is defined half-way between the overlapping strips at the ground level, and X axis is along the scan-line (across the flight direction). In the figure, x_A and x_B denote lateral coordinates of a ground object point P relative to the laser unit frame, and the lateral distance between two flight lines is represented by D.
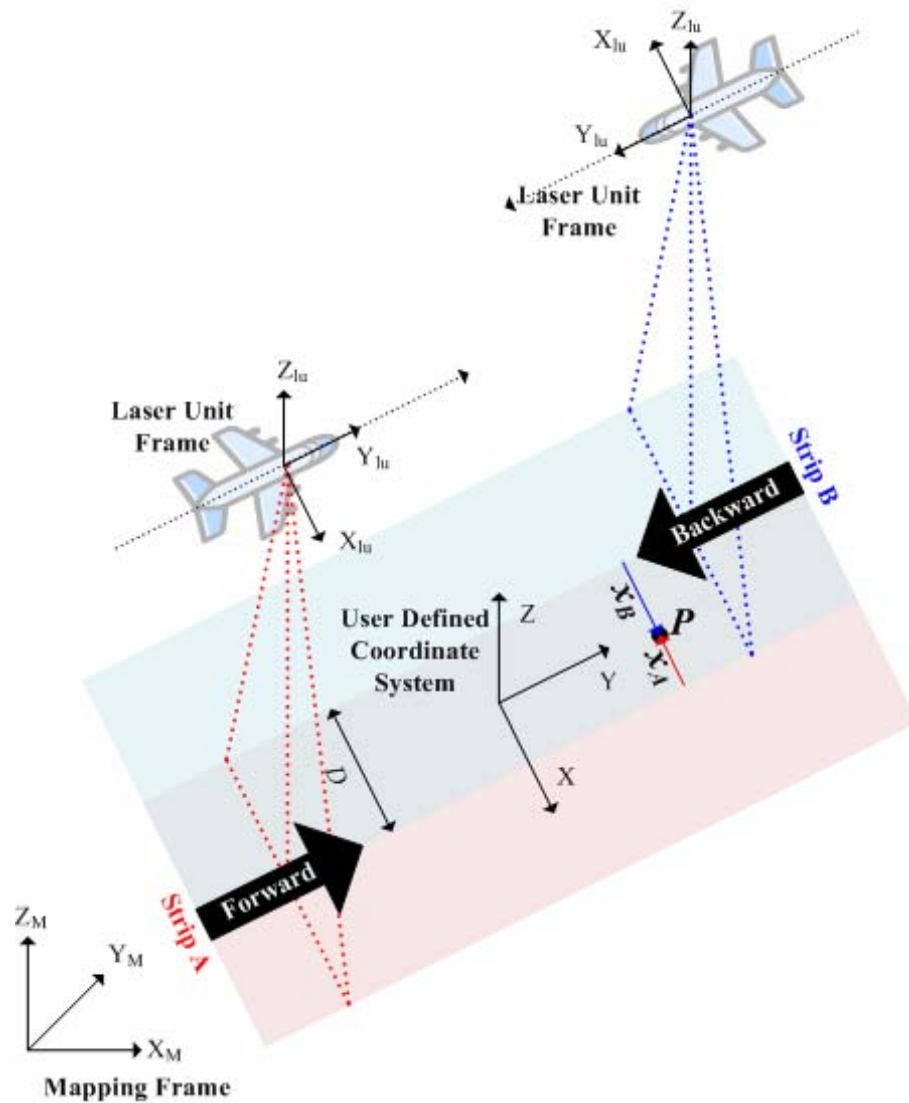
Figure 3.1. Flight lines and definitions of used coordinate systems in overlapping strips.

In the local coordinate system, the LiDAR geo-referencing equation as introduced in section 2.2 can be simplified using the aforementioned assumptions. Thus, the rotation matrix $R_{(yaw, pitch, roll)}$ relating the ground and IMU body frame leads to an identity matrix for the forward strip; however, the 1st and 2nd diagonal elements relating x and y coordinates are negative values for the backward strips (Equation 3.1). In addition, the

rotation matrix $R_{(\Delta\omega,\ \Delta\varphi,\ \Delta\kappa)}$ relating the boresight can be represented by Equation 3.2 for

small boresight angles. Therefore, the LiDAR geo-referencing equation leads to the form

in Equation 3.3. In this equation, the multiple signs ($\pm$ & $\mp$) pertain to the forward and

backward strips with the upper sign referring to the forward strip and the lower sign

referring to the backward strip.

$$R_{yaw,pitch,roll} = \begin{bmatrix} \pm 1 & 0 & 0 \\ 0 & \pm 1 & 0 \\ 0 & 0 & 1 \end{bmatrix} \tag{3.1}$$

$$R_{\Delta\omega,\ \Delta\phi,\ \Delta\kappa} = \begin{bmatrix} 1 & -\Delta\kappa & \Delta\varphi \\ \Delta\kappa & 1 & -\Delta\omega \\ -\Delta\varphi & \Delta\omega & 1 \end{bmatrix} \tag{3.2}$$

$$
\begin{aligned}
\vec{X}_U &\approx \vec{X}_o + \begin{bmatrix} \pm\Delta X \\ \pm\Delta Y \\ \Delta Z \end{bmatrix} + \begin{bmatrix} \pm 1 & \mp\Delta\kappa & \pm\Delta\varphi \\ \pm\Delta\kappa & \pm 1 & \mp\Delta\omega \\ -\Delta\varphi & \Delta\omega & 1 \end{bmatrix} \begin{bmatrix} -(\rho+\Delta\rho)\sin(S\beta) \\ 0 \\ -(\rho+\Delta\rho)\cos(S\beta) \end{bmatrix} \\
&= \vec{X}_o + \begin{bmatrix} \pm\Delta X \\ \pm\Delta Y \\ \Delta Z \end{bmatrix} + \begin{bmatrix} \pm 1 & \mp\Delta\kappa & \pm\Delta\varphi \\ \pm\Delta\kappa & \pm 1 & \mp\Delta\omega \\ -\Delta\varphi & \Delta\omega & 1 \end{bmatrix} \begin{bmatrix} x \\ 0 \\ -H \end{bmatrix}
\end{aligned}
\tag{3.3}
$$

where,

$\vec{X}_U$ denotes the point coordinates in question with respect to the local coordinate system,

$\Delta X, \Delta Y, \Delta Z$ are the components of the lever-arm offset vector $\vec{P}_G$,

S is a scale for the encoder angle β (this scale should be unity for a bias-free system),

H is the flight altitude above ground, and

x is the lateral coordinate of the LiDAR point in question with respect to the laser unit

frame.

The LiDAR point coordinates ($\vec{X}_U$), as presented in Equation 3.3, are functions of the system parameters ($\vec{x}$) and measurements ($\vec{l}$); it can be represented as the true point coordinates ($\vec{X}_{True}$) without systematic errors (Equation 3.4). In the presence of biases in the system parameters, the LiDAR point coordinates will become biased ($\vec{X}_{Biased}$) and will be functions of the system parameters and measurements as well as the biases in the system parameters ($\delta\vec{x}$), as expressed by Equation 3.5. As shown in Equation 3.5, this research will investigate the impact of biases in the lever-arm offset components ($\delta\Delta X$, $\delta\Delta Y$, $\delta\Delta Z$), biases in the boresight angles ($\delta\Delta\omega$, $\delta\Delta\varphi$, $\delta\Delta\kappa$), constant bias in the measured ranges ($\delta\Delta\rho$), and constant scale bias in the encoder angle (δS). Equation 3.5 can be linearized with respect to the system parameters using Taylor series expansion, yielding the form in Equation 3.6, after ignoring second and higher order terms. In Equation 3.6, the term $\partial f / \partial\vec{x}$ represents the partial derivatives with respect to the system parameters, while the term $(\partial f / \partial\vec{x})\delta\vec{x}$ represents the impact of the system biases on the derived point cloud coordinates.

$$\vec{X}_u = \vec{X}_{True} = f(\vec{x}, \vec{l}) \tag{3.4}$$

where,

$\vec{x} = (\Delta X, \Delta Y, \Delta Z, \Delta\omega,\ \Delta\varphi,\ \Delta\kappa, \Delta\rho, S)$, and

$\vec{l} = (\vec{X}_o, \beta, \rho)$

$$\vec{X}_{Biased} = f(\vec{x} + \delta\vec{x}, \vec{l}) \tag{3.5}$$

where,

$\delta\vec{x} = (\delta\Delta X, \delta\Delta Y, \delta\Delta Z, \delta\Delta\omega,\ \delta\Delta\varphi,\ \delta\Delta\kappa, \delta\Delta\rho, \delta S)$

$$\vec{X}_{Biased} \approx f(\vec{x},\vec{l}) + \frac{\partial f}{\partial \vec{x}} \delta \vec{x} = \vec{X}_{True} + \frac{\partial f}{\partial \vec{x}} \delta \vec{x} \tag{3.6}$$

The impact of the biases in lever-arm parameters and boresight angles are represented by the forms of Equations 3.7a and 3.7b; the impact of the biases in the range measurements and the encoder angle scale factor are given by Equations 3.7c and 3.7d. As previously discussed in section 2.3, the errors caused by the biases in the lever-arm parameters on the ground are constant along the scan-lines. Equation 3.7a, which is compatible with Figure 2.11a, shows the mathematical expression of the impact of the biases in the lever-arm offset. As one can see in the equation, the biases in the lever-arm offset produce constant errors on the ground, whose magnitudes are equivalent to the size of the biases. In addition, the errors are dependent on the flight direction except the error in the Z coordinate; the multiple signs in the equation pertain to the forward (upper sign) and backward (lower sign) strips.

$$\frac{\partial f}{\partial \Delta X} \delta \Delta X + \frac{\partial f}{\partial \Delta Y} \delta \Delta Y + \frac{\partial f}{\partial \Delta Z} \delta \Delta Z = \begin{bmatrix} \pm \delta \Delta X \\ \pm \delta \Delta Y \\ \delta \Delta Z \end{bmatrix} \tag{3.7a}$$

$$\frac{\partial f}{\partial \Delta \omega} \delta \Delta \omega + \frac{\partial f}{\partial \Delta \varphi} \delta \Delta \varphi + \frac{\partial f}{\partial \Delta \kappa} \delta \Delta \kappa = \begin{bmatrix} \mp H \delta \Delta \varphi \\ \pm H \delta \Delta \omega \pm x \delta \Delta \kappa \\ - x \delta \Delta \varphi \end{bmatrix} \tag{3.7b}$$

$$\frac{\partial f}{\partial \Delta \rho} \delta \Delta \rho = \begin{bmatrix} \mp \sin(S\beta) \delta \Delta \rho \mp \Delta \varphi \cos(S\beta) \delta \Delta \rho \\ \mp \Delta \kappa \sin(S\beta) \delta \Delta \rho \pm \Delta \omega \cos(S\beta) \delta \Delta \rho \\ \Delta \varphi \sin(S\beta) \delta \Delta \rho - \cos(S\beta) \delta \Delta \rho \end{bmatrix} \approx \begin{bmatrix} \mp \sin(S\beta) \delta \Delta \rho \\ 0 \\ -\cos(S\beta) \delta \Delta \rho \end{bmatrix} \tag{3.7c}$$

$$\frac{\partial f}{\partial S}\delta S = \begin{bmatrix} \mp H\beta\delta S \mp \Delta\varphi x\beta\delta S \\ \mp \Delta\kappa H\beta\delta S \pm \Delta\omega x\beta\delta S \\ \Delta\varphi H\beta\delta S - x\beta\delta S \end{bmatrix} \approx \begin{bmatrix} \mp H\beta\delta S \\ 0 \\ -x\beta\delta S \end{bmatrix} \tag{3.7d}$$

The impacts of the biases in boresight angles are represented in Equation 3.7b which is compatible with Figures 2.11b, 2.11c, and 2.11d. As shown in the equation, the *X* coordinates (across the flight direction) are distorted by the bias in the boresight roll ($\delta\Delta\varphi$) and the difference between true and biased *X* coordinates depend on the flight altitude (*H*). The coordinate difference is constant because the flight altitude does not change during the data capturing time and the object surface is flat according to the previous assumptions. Therefore, the bias $\delta\Delta\varphi$ leads to constant *X* coordinate differences along the scan-lines. The bias in the boresight pitch angle ($\delta\Delta\omega$) causes constant errors along the flight direction, whose magnitudes depend on the flight altitude. The bias in the boresight yaw ($\delta\Delta\kappa$) causes errors along the flight direction (*Y*); however, the differences between true and biased coordinates change with the encoder angle (along the scan-line). The differences of *Z* coordinates are caused by the bias $\delta\Delta\varphi$ and change along the scan-lines.

Equation 3.7c and 3.7d represent the impacts of the biases in the range measurements and the encoder angle scale factor, respectively. The differences caused by both biases ($\delta\Delta\rho$ and δS) between true and biased coordinates along the flight direction (*Y*) are small enough to be ignored (see Figures 2.11e and 2.11f). As shown in Equation 3.7c and 3.7d, the differences of *Y* coordinates are represented by the multiplication of small boresight angles and bias terms and those values are close to zero. For example, the differences of

Y coordinates caused by the biases in the range measurements (0.5m) and encoder angle scale factor (0.001) are much less than 1mm under the conditions of the simulation test in section 2.3 (see Table 2.3). On the other hand, the biases ($\delta\Delta\rho$ and δS) produce differences that are changing along the scan-lines to *X* (across the flight direction) and *Z* coordinates. Equation 3.8 represents the differences between true and biased coordinates caused by all the considered biases for the forward and backward strips. One should note that Equation 3.8 can be derived after ignoring the multiplication of small boresight angles and bias terms in Equation 3.7c and 3.7d; in addition, the multiple signs in those equations indicate the impact for the forward and backward strips (with the upper sign referring to the forward strip).

$$\vec{X}_{Biased} - \vec{X}_{True} = \frac{\partial f}{\partial \vec{x}} \delta\vec{x} \approx \begin{bmatrix} \pm \delta\Delta X \mp H \, \delta\Delta\varphi \mp \sin(S\beta) \, \delta\Delta\rho \mp H\beta\delta S \\ \pm \delta\Delta Y \pm H\delta\Delta\omega \pm x\delta\Delta\kappa \\ \delta\Delta Z - x\delta\Delta\varphi - \cos(S\beta) \, \delta\Delta\rho - x\beta\delta S \end{bmatrix} \qquad (3.8)$$

So far, we derived the impact of various biases in the LiDAR system parameters on the LiDAR point cloud in Equation 3.8. Using the derived expression, we would like to derive the mathematical relationship between conjugate points in overlapping strips, which are flown in the same or opposite directions. The mathematical relationship between these points can be derived by rewriting Equation 3.8 for the two overlapping strips and subtracting the resulting equations from each other. An example of such a relationship for two strips, which are flown in opposite directions, is shown in Equation 3.9. In this equation, β_A and β_B denote encoder angles of the forward strip A and

backward strip B, respectively. The coordinates x_A and x_B denote the laser unit coordinates of both forward and backward strips along the scan-lines.

$$\begin{bmatrix} X_A - X_B \\ Y_A - Y_B \\ Z_A - Z_B \end{bmatrix} \approx \begin{bmatrix} 2\delta\Delta X - 2H \ \delta\Delta\varphi - (\sin(S\beta_A) + \sin(S\beta_B)) \ \delta\Delta\rho - H \ (\beta_A + \beta_B) \ \delta S \\ 2\delta\Delta Y + 2H \ \delta\Delta\omega + (x_A + x_B) \ \delta\Delta\kappa \\ -(x_A - x_B) \ \delta\Delta\varphi - (\cos(S\beta_A) - \cos(S\beta_B)) \ \delta\Delta\rho - (x_A \ \beta_A - x_B \ \beta_B) \ \delta S \end{bmatrix} \quad (3.9)$$

Equation 3.9 can be simplified by assuming that the differences between sine and tangent functions within the scan angle range of $\pm 25°$ are small enough to be ignored, which is the typical value for operational LiDAR systems. Therefore, the term $(\sin(S\beta_A) + \sin(S\beta_B))\delta\Delta\rho$ in Equation 3.9 can be represented by Equation 3.10. One should note that two cases are possible: the backward strip B can be on the left or right sides of the forward strip A (Figure 3.2); in Equations 3.10 and 3.11, the upper/lower signs pertain to the strips B_L and B_R, respectively (Figure 3.2). For the strip B_L, $-(x_A + x_B)$ is equivalent to D (the lateral distance between two flight lines), and, in the other case (the strip B_R), the term is equivalent to $-D$. Also, one assume that the value, "$\cos(S\beta)\delta\Delta\rho$", does not significantly change within the nominal scan angle range (e.g., $\pm 25°$); therefore, the term $(\cos(S\beta_A) - \cos(S\beta_B)) \ \delta\Delta\rho$ can be reduced to zero. Assuming $\beta_A \approx -x_A / H$ and $\beta_B \approx -x_B / H$, the term $(x_A \ \beta_A - x_B \ \beta_B)\delta S$ can be rewritten as $(\beta_A + \beta_B)(x_A - x_B)\delta S$, where $(\beta_A + \beta_B)$ approximate to β_T which is the total scan angle between the two flight lines (i.e., the angle from one flight line to an object point, which is vertically below the second flight line – refer to Figure 3.2). Therefore, such simplification leads to Equation 3.11. In this equation, the multiple signs pertain to the strips B_L and B_R in Figure 3.2, respectively.

$$(\sin(S\beta_A) + \sin(S\beta_B))\delta\Delta\rho \approx (\tan(S\beta_A) + \tan(S\beta_B))\delta\Delta\rho$$
$$= (-x_A / H - x_B / H)\delta\Delta\rho = \delta\Delta\rho(\pm D / H) \tag{3.10}$$

$$\begin{bmatrix} X_A - X_B \\ Y_A - Y_B \\ Z_A - Z_B \end{bmatrix} \approx \begin{bmatrix} 2\,\delta\Delta X - 2\,H\,\delta\Delta\varphi \mp (D/H)\delta\Delta\rho \mp H\,\beta_T\,\delta S \\ 2\delta\Delta Y + 2\,H\,\delta\Delta\omega \mp D\,\delta\Delta\kappa \\ -(x_A - x_B)\,\delta\Delta\varphi \mp (x_A - x_B)\,\beta_T\,\delta S \end{bmatrix} \tag{3.11}$$
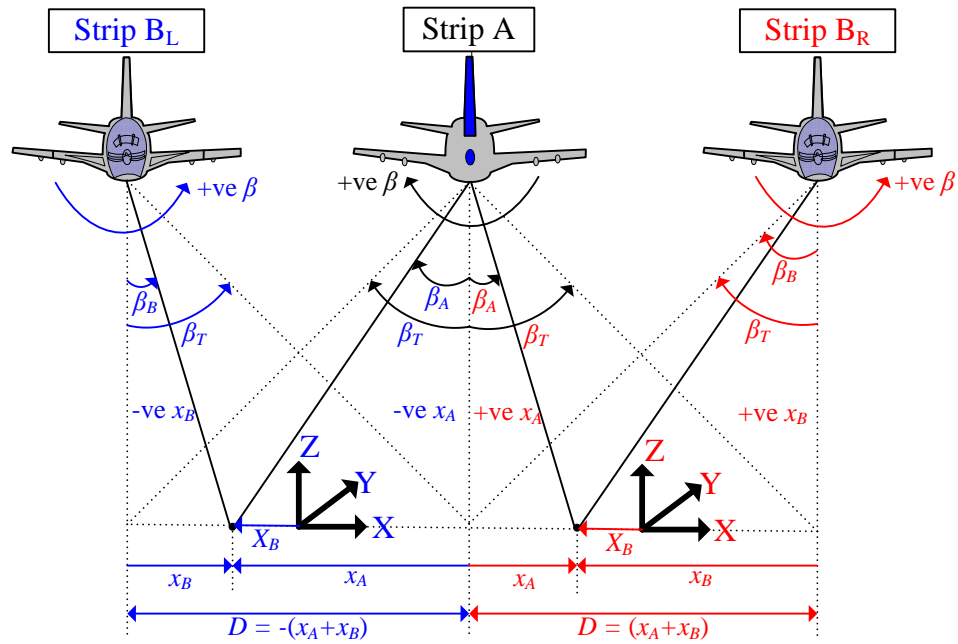
Figure 3.2. Observed object point in overlapping strips flown in opposite directions.

The third row "$-(x_A - x_B)\,\delta\Delta\varphi \mp (x_A - x_B)\,\beta_T\delta S$" of Equation 3.11 denotes the impact of the biases ($\delta\Delta\varphi$ and δS) on the vertical discrepancy between conjugate points. The following derivation will show that this impact can be analyzed using a rotation defined by the biases. In Figure 3.2, X_B denotes the object point coordinate across the flight direction with respect to the local coordinate system. The lateral coordinates x_A and x_B of LiDAR points of the overlapping strips can be represented by $\mp D/2 + X_B$ and

$\mp D/2 - X_B$, respectively, where the multiple sings pertain to the strips B_L and B_R; hence, the difference between the lateral coordinates $(x_A - x_B)$ can yield $2X_B$. The values of the sine function for $2\delta\Delta\varphi$ and $2\beta_T\delta S$ approximate to $2\delta\Delta\varphi$ and $2\beta_T\delta S$; the values for cosine function are close to 1.0 because both the angular values are considered small angles. In addition, one should notice that Z_B can be ignored because of the assumption of relatively flat terrain and the use of a user defined coordinate system. Consequently, the impact of the biases ($\delta\Delta\varphi$ and δS) can lead to $R_{(0,2\delta\Delta\varphi\pm2\beta_T\delta S,0)}$ which is a rotation around Y axis (along the flight direction) as shown in Equation 3.12. Figure 3.3 graphically illustrates Equation 3.12. As it can be seen in this figure, the height discrepancy between conjugate points in overlapping strips (last row in Equations 3.11 or 3.12) is the result of a rotation around the flight direction (i.e., roll angle equivalent to $2\delta\Delta\varphi\pm2\beta_T\delta S$).

$$
\begin{bmatrix} 0 \\ 0 \\ -(x_A - x_B)\,\delta\Delta\varphi \mp (x_A - x_B)\,\beta_T\delta S \end{bmatrix} + \begin{bmatrix} X_B \\ Y_B \\ Z_B \end{bmatrix}
$$

$$
\approx \begin{bmatrix} X_B \\ Y_B \\ (-2\delta\Delta\varphi \mp 2\beta_T\delta S)X_B + Z_B \end{bmatrix} \approx \begin{bmatrix} X_B + (2\delta\Delta\varphi \pm 2\beta_T\delta S)Z_B \\ Y_B \\ (-2\delta\Delta\varphi \mp 2\beta_T\delta S)X_B + Z_B \end{bmatrix} \quad (3.12)
$$

$$
= \begin{bmatrix} 1 & 0 & (2\delta\Delta\varphi \pm 2\beta_T\delta S) \\ 0 & 1 & 0 \\ (-2\delta\Delta\varphi \mp 2\beta_T\delta S) & 0 & 1 \end{bmatrix} \begin{bmatrix} X_B \\ Y_B \\ Z_B \end{bmatrix} \approx R_{(0,2\delta\Delta\varphi\pm2\beta_T\delta S,0)} \begin{bmatrix} X_B \\ Y_B \\ Z_B \end{bmatrix}
$$

where,

$$
x_A - x_B = (\mp\frac{D}{2} + X_B) - (\mp\frac{D}{2} - X_B) \approx 2X_B \text{ (refer to Figure 3.2)},
$$

$Z_B \approx 0$, and

$$(2\delta\Delta\varphi \pm 2\beta_T\delta S)Z_B \approx 0$$
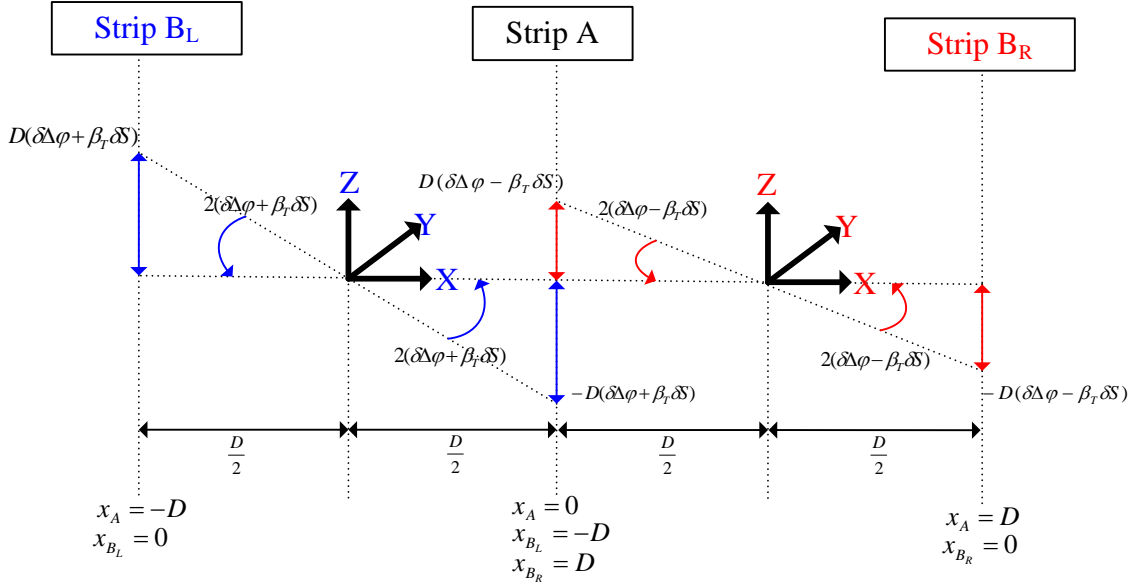
Figure 3.3. The introduced tilt across the flight direction by the biases in the boresight roll angle and encoder angle scale factor.

Equation 3.13 can be derived from Equation 3.11 after applying the mathematical manipulation in Equation 3.12. As shown in Equation 3.13, the relationship between the conjugate points in the forward and backward strips can be represented by a function of shifts and a rotation around the flight direction (*Y* axis).

$$\begin{bmatrix} X_A \\ Y_A \\ Z_A \end{bmatrix} = \begin{bmatrix} 2\,\delta\Delta X - 2\,H\,\delta\Delta\varphi \mp D/H\,\delta\Delta\rho \mp H\beta_T\delta S \\ 2\,\delta\Delta Y + 2\,H\,\delta\Delta\omega \mp D\,\delta\Delta\kappa \\ 0 \end{bmatrix} + R_{(0,\,2\delta\Delta\varphi \pm 2\beta_T\delta S,\,0)} \begin{bmatrix} X_B \\ Y_B \\ Z_B \end{bmatrix} \qquad (3.13)$$

For two flight lines flown in opposite directions with 100% overlap, Equation 3.13 would reduce to the form in Equation 3.14 since the lateral distance (*D*) between the two flight lines is zero. As shown in Figure 3.4, the lateral laser unit coordinates (x_A and x_B) and

encoder angles (β_A and β_B) of the forward and backward strips have opposite signs and their magnitudes are equivalent for an object point in the overlapping area.

$$\begin{bmatrix} X_A \\ Y_A \\ Z_A \end{bmatrix} = \begin{bmatrix} 2\,\delta\Delta X - 2\,H\,\delta\Delta\varphi \\ 2\,\delta\Delta Y + 2\,H\,\delta\Delta\omega \\ 0 \end{bmatrix} + R_{(0,2\delta\Delta\varphi,0)} \begin{bmatrix} X_B \\ Y_B \\ Z_B \end{bmatrix} \tag{3.14}$$
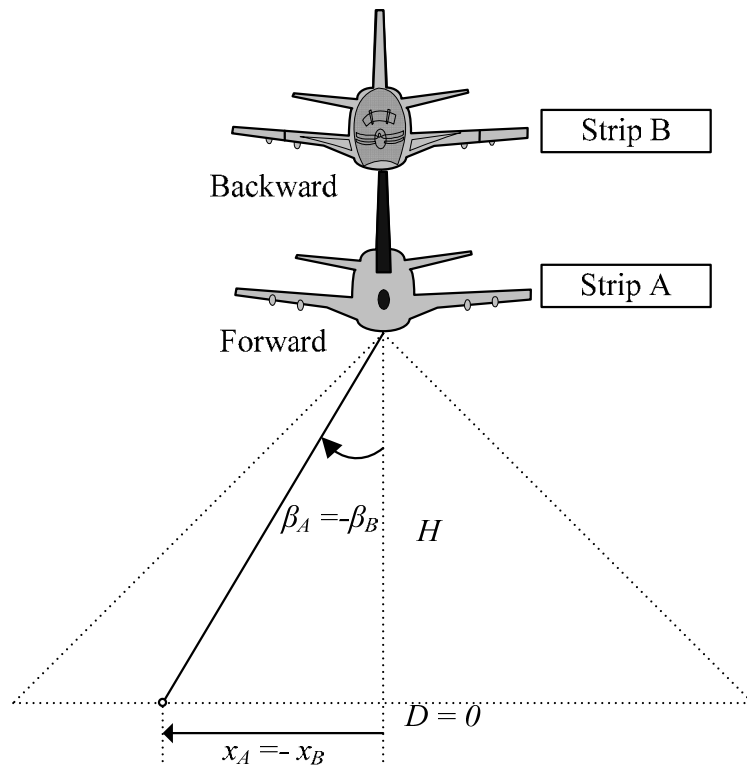
Figure 3.4. Observed object point in overlapping strips flown in opposite directions with 100% overlap.

In a similar way, Equation 3.8 leads to Equation 3.15 for two overlapping strips flown in same directions with a lateral distance D (Figure 3.5). In Equation 3.15, $(\sin(S\beta_A) - \sin(S\beta_B))$ approximates to D/H based on the assumption that $\sin(S\beta_A)$ and $\sin(S\beta_B)$ are close to $\tan(S\beta_A)$ and $\tan(S\beta_B)$ within the common encoder angle range

and $(\tan(S\beta_A) - \tan(S\beta_B))H$ is the lateral distance D. Assuming $\beta_A \approx -x_A / H$ and

$\beta_B \approx -x_B / H$, the term $(x_A \beta_A - x_B \beta_B)$ can be rewritten by $(\beta_A - \beta_B)(x_A + x_B)$, where

$(\beta_A - \beta_B)$ approximate to β_T (the total scan angle between the two flight lines). In the

similar way of Equation 3.12, $(x_A + x_B)$ approximate to $2X_B$ and the

term $-(x_A + x_B)\beta_T \delta S$ in the last row of Equation 3.15 can be represented by the rotation

matrix $(R_{(0,2\beta_T \delta S,0)})$ along the flight direction; therefore, Equation 3.15 can be rewritten by

Equation 3.16.
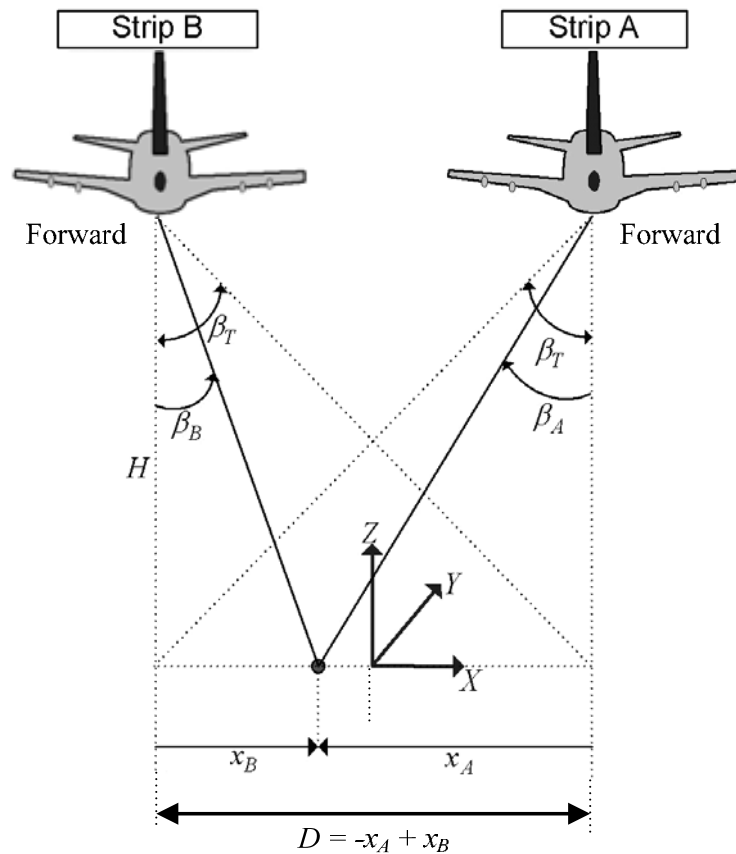
Figure 3.5. Observed object point in overlapping strips flown in same directions.

$$
\begin{bmatrix} X_A - X_B \\ Y_A - Y_B \\ Z_A - Z_B \end{bmatrix} \approx \begin{bmatrix} -(\sin(S\beta_A) - \sin(S\beta_B))\, \delta\Delta\rho - H\,(\beta_A - \beta_B)\, \delta S \\ (x_A - x_B)\, \delta\Delta\kappa \\ -(x_A - x_B)\, \delta\Delta\varphi - (x_A\,\beta_A - x_B\,\beta_B)\, \delta S \end{bmatrix}
$$

$$
\approx \begin{bmatrix} -D/H\; \delta\Delta\rho - H\beta_T \delta S \\ -D\, \delta\Delta\kappa \\ D\, \delta\Delta\varphi - (x_A + x_B)\,\beta_T \delta S \end{bmatrix} \tag{3.15}
$$

$$
\begin{bmatrix} X_A \\ Y_A \\ Z_A \end{bmatrix} = \begin{bmatrix} -D/H\; \delta\Delta\rho - H\beta_T \delta S \\ -D\; \delta\Delta\kappa \\ D\; \delta\Delta\varphi \end{bmatrix} + R_{(0,\,2\beta_T \delta S,\,0)} \begin{bmatrix} X_B \\ Y_B \\ Z_B \end{bmatrix} \tag{3.16}
$$

Equations 3.13, 3.14, and 3.16 reveal the possibility of identifying the presence of systematic errors in the system parameters by evaluating the discrepancies between conjugate points in overlapping strips, which are flown in the same or opposite directions. Moreover, using these equations, it is possible to determine the flight configuration that maximizes the impact of systematic errors. For example, as it can be seen in Equation 3.16, large lateral distance (D) between the overlapping strips is useful for magnifying the boresight yaw and roll biases as well as biases in the range and encoder angle scale factor. In addition, higher flight altitudes are optimal for magnifying the boresight pitch and roll biases (refer to Equations 3.13 and 3.14). Also, closer inspection of these equations would allow for the determination of an optimal flight configuration design, which decouples various systematic errors. For example, working with four strips which are captured from two flight altitudes in opposite directions with 100% overlap are optimal for the recovery of the planimetric lever-arm offsets as well as the boresight pitch and roll biases (Equation 3.14). In addition, two flight lines flown in the same direction with the large lateral distance D are optimal for the recovery of the boresight yaw and roll

biases, range bias, and encoder angle scale factor bias (Equation 3.16). One should however know that the lack of overlap ratio can decrease the reliability of determining the transformation parameters between overlapping strips. Therefore, 30-50% overlap ratios can be recommended.

Figure 3.6 illustrates the optimal configuration of overlapping strips required for using the proposed simplified calibration method. As previously discussed, there are three possible configurations for parallel overlapping strips. Among them, two overlapping cases are essentially required to estimate the considered systematic biases: first, two strips flown in opposite flight directions with 100% overlap ratio (case 1.a and 1.b in Figure 3.6) and second, two strips flown in same flight directions with large lateral distance between two flight lines (case 2 in Figure 3.6). Two overlapping strip pairs of the first case from two different flight altitudes are required to decouple $\delta\varDelta Y$ and $\delta\varDelta\omega$. The impact of $\delta\varDelta Y$ is independent of the flight altitude while $\delta\varDelta\omega$ produces different errors as the flight altitude changes (refer to Equation 3.14). A closer investigation of Equations 3.13, 3.14, and 3.16 reveals that $\delta\varDelta Z$, the bias in the lever-arm offset along the Z direction cannot be determined by observing discrepancies between conjugate surface elements in overlapping strips. Such inability is caused by the fact that a vertical bias in the lever-arm parameters produces the same effect regardless of the flight direction, flight altitude, or encoder angle (see section 2.3). In the experimental results chapter, calibration results using simulated and real datasets with the optimum flight configuration will be demonstrated.
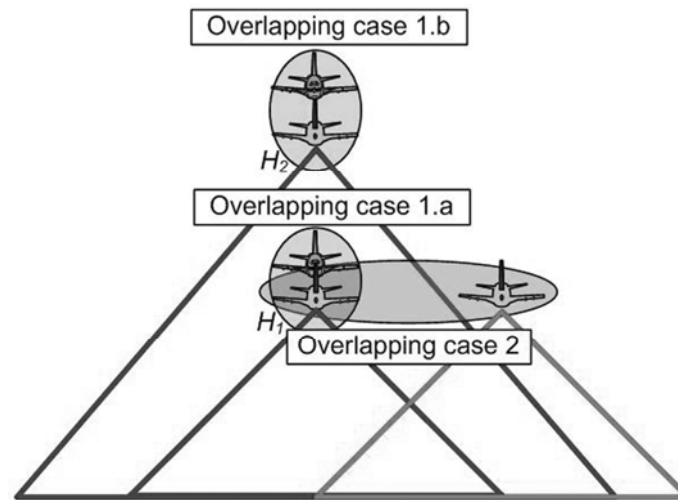
Figure 3.6. Two types of optimal overlapping cases: case 1 consists of two stips flown opposite directions with 100% overlap, and two strips have less than 100% overlap ratio and same flight direction in case 2.

In summary, the discrepancies between parallel strips in the presence of the studied biases can be modeled by 3 shifts and a rotation angle around the flight line (Equation 3.17). Once the transformation parameters relating parallel overlapping strips are determined, the biases in the system parameters can be estimated using Equations 3.18, 3.19, and 3.20. The relationship between the system biases and the discrepancies (X_T, Y_T, Z_T, and φ) between conjugate bias-contaminated points in two flight lines, which are flown in opposite directions is given by Equation 3.18. This equation would reduce to the form in Equation 3.19 for flight lines with 100% overlap. For two flight lines flown in the same direction, the relationship between the system biases and the discrepancies between the strips is expressed by Equation 3.20. The multiple signs ($\pm$ & $\mp$) in Equation 3.18 pertain to two possible cases of the opposite/non-100% overlapping strips; the upper sign refers to the case where strip B (backward) is on the left side of strip A (forward),

while the lower sign refers to the case where strip B is on the right side of strip A (refer to

Figures 3.2 and 3.3).

$$\begin{bmatrix} X_A \\ Y_A \\ Z_A \end{bmatrix} = \begin{bmatrix} X_T \\ Y_T \\ Z_T \end{bmatrix} + R_{(0,\varphi,0)} \begin{bmatrix} X_B \\ Y_B \\ Z_B \end{bmatrix} \qquad (3.17)$$

$$\begin{bmatrix} X_T \\ Y_T \\ \varphi \end{bmatrix} = \begin{bmatrix} 2\,\delta\Delta X - 2\,H\,\delta\Delta\varphi \mp D/H\,\delta\Delta\rho \mp H\beta_T\,\delta S \\ 2\,\delta\Delta Y + 2\,H\,\delta\Delta\omega \mp D\,\delta\Delta\kappa \\ 2\delta\Delta\varphi \pm 2\beta_T\,\delta S \end{bmatrix} \qquad (3.18)$$

$$\begin{bmatrix} X_T \\ Y_T \\ \varphi \end{bmatrix} = \begin{bmatrix} 2\,\delta\Delta X - 2\,H\,\delta\Delta\varphi \\ 2\,\delta\Delta Y + 2\,H\,\delta\Delta\omega \\ 2\delta\Delta\varphi \end{bmatrix} \qquad (3.19)$$

$$\begin{bmatrix} X_T \\ Y_T \\ Z_T \\ \varphi \end{bmatrix} = \begin{bmatrix} -D/H\,\delta\Delta\rho - H\beta_T\,\delta S \\ -D\,\delta\Delta\kappa \\ D\,\delta\Delta\varphi \\ 2\beta_T\,\delta S \end{bmatrix} \qquad (3.20)$$

Once the procedure for the estimation of the four parameters (X_T, Y_T, Z_T, and φ) of

Equation 3.17 is carried out for all considered overlapping strip pairs, the biases ($\delta\varDelta X$,

$\delta\varDelta Y$, $\delta\varDelta\omega$, $\delta\varDelta\varphi$, $\delta\varDelta\kappa$, δS, and $\delta\rho$) in the system parameters are determined by Equations

3.18, 3.19, and 3.20. After estimating the biases, the biased point cloud coordinates can

be adjusted by Equation 3.21 to remove the impact of incorrect system parameters.

Equation 3.21 can be derived from Equation 3.8 which represents the mathematical

relationship between true and biased coordinates with systematic biases terms. In

Equation 3.21, "yaw" denotes the flight direction. One should note that the correction

terms calculated using the estimated biases ($\delta\hat{\Delta} X$, $\delta\hat{\Delta} Y$, $\delta\hat{\Delta}\omega$, $\delta\hat{\Delta}\varphi$, $\delta\hat{\Delta}\kappa$, $\delta\hat{\rho}$ and $\delta\hat{S}$)

should be rotated using the rotation matrix R_{yaw}, because the correction terms are calculated based on the assumption that the flight direction is parallel to the *Y* axis of the ground coordinate system. In this equation, *H* is the nominal flight altitude; β and *x* are encoder angle and lateral laser unit coordinate of a LiDAR point in question, respectively. Since the system raw measurements are not available, β and *x* should be approximately determined as shown in Figure 3.7. The lateral coordinate *x* is determined based on an approximate centre of a scan-line, and the encoder angle β is estimated using the flight altitude H_0, point elevation *Z*, and estimated lateral coordinate *x* (i.e., $\beta = -\tan^{-1}[x / (H_0 - Z)]$).

$$\vec{X}_{Adjusted} = \vec{X}_{Biased} - R^{T}_{yaw} \begin{bmatrix} \delta\hat{\Delta}X - (H_0 - Z)\delta\hat{\Delta}\varphi - \sin\beta\,\delta\hat{\rho} - (H_0 - Z)\beta\,\delta\hat{S} \\ \delta\hat{\Delta}Y + (H_0 - Z)\delta\hat{\Delta}\omega + x\delta\hat{\Delta}\kappa \\ \delta\hat{\Delta}Z - x\delta\hat{\Delta}\varphi - \cos\beta\,\delta\hat{\rho} - x\beta\,\delta\hat{S} \end{bmatrix} \qquad (3.21)$$
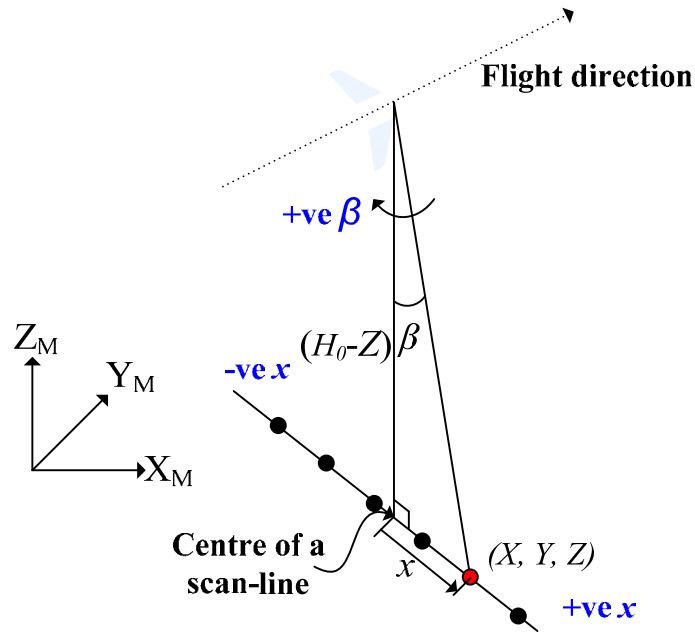
Figure 3.7. Estimation of lateral coordinates and encoder angles for a LiDAR point.

3.3 Quasi-Rigorous Method

The second proposed method, denoted as the quasi-rigorous method, can deal with non-parallel strips, heading variations, and varying terrain elevations in contrast to the simplified method. It can be achieved by the use of time-tagged point cloud and trajectory position data. The quasi-rigorous method is developed with following assumptions: a) we are dealing with a linear scanner, b) LiDAR strips are captured by a levelled laser scanner (i.e., pitch and roll angles are very small and can be assumed to be zero), and c) boresight angles are small. Such assumptions simplify the LiDAR geo-referencing equation as represented by Equation 2.1 to the form in Equation 3.22.

$$
\begin{aligned}
\vec{X}_G &\approx \vec{X}_o + \begin{bmatrix} \cos(yaw) & -\sin(yaw) & 0 \\ \sin(yaw) & \cos(yaw) & 0 \\ 0 & 0 & 1 \end{bmatrix} \left(\begin{bmatrix} \Delta X \\ \Delta Y \\ \Delta Z \end{bmatrix} + \begin{bmatrix} 1 & -\Delta\kappa & \Delta\varphi \\ \Delta\kappa & 1 & -\Delta\omega \\ -\Delta\varphi & \Delta\omega & 1 \end{bmatrix} \begin{bmatrix} -(\rho+\Delta\rho)\sin(S\beta) \\ 0 \\ -(\rho+\Delta\rho)\cos(S\beta) \end{bmatrix} \right) \\
&= \vec{X}_o + \begin{bmatrix} \cos(yaw) & -\sin(yaw) & 0 \\ \sin(yaw) & \cos(yaw) & 0 \\ 0 & 0 & 1 \end{bmatrix} \left(\begin{bmatrix} \Delta X \\ \Delta Y \\ \Delta Z \end{bmatrix} + \begin{bmatrix} 1 & -\Delta\kappa & \Delta\varphi \\ \Delta\kappa & 1 & -\Delta\omega \\ -\Delta\varphi & \Delta\omega & 1 \end{bmatrix} \begin{bmatrix} x \\ 0 \\ z \end{bmatrix} \right)
\end{aligned}
\tag{3.22}
$$

where,
z is the vertical coordinate of the laser point with respect to the laser unit coordinate system, and
x is the lateral coordinate of the laser point with respect to the laser unit coordinate system, which is the lateral distance (with the appropriate sign) between the LiDAR point in question and the projection of the flight trajectory onto the ground.

Unlike the simplified method, the quasi-rigorous method does not require straight flight lines, because the firing point position and heading are estimated by trajectory position data and time-tagged points. It should be mentioned that the point cloud coordinates ($\vec{X}_U$ shown in Equation 3.3) are handled in the user defined coordinate system in the

simplified method, where all flight directions are assumed either as forward or backward, while the quasi-rigorous method handles the LiDAR points ($\vec{X}_G$ in Equation 3.22) in the ground coordinate system with the flight direction. In Equation 3.22, z is the vertical coordinate of the laser point with respect to the laser unit frame, and it is determined by subtracting the elevation of laser firing point from the LiDAR point elevation. The x-laser unit coordinate is determined by the lateral distance between the LiDAR point in question and the projection of the flight line onto the ground. As shown in Figure 3.8, the local flight line for the LiDAR point is determined by fitting a straight line using neighbouring trajectory points. For a LiDAR point mapped at time t, neighbouring trajectory points are identified within a certain time interval ($t - \Delta t$, $t + \Delta t$). Then, a straight line is fitted through the selected trajectory positions to come up with a local estimate of the trajectory. The selected time interval should ensure having enough samples to reliably represent the local trajectory. Besides the duration of the time interval, the number of samples depends on the density of the trajectory data.

As previously discussed in the simplified method, the distorted LiDAR point coordinates due to biases in the system parameters can be represented by a function of the system parameters $\vec{x}$, measurements $\vec{l}$, and the biases in the system parameters $\delta\vec{x}$ (refer to Equation 3.5), which can be expanded using Taylor series expansion after ignoring second and higher order terms. Similar to the simplified method, we are considering biases in the lever-arm offset components, boresight angles, mirror angle scale, and laser range ($\delta\Delta X$, $\delta\Delta Y$, $\delta\Delta Z$, $\delta\Delta\omega$, $\delta\Delta\varphi$, $\delta\Delta\kappa$, δS, and $\delta\Delta\rho$). Equations 3.23, 3.24, 3.25, and 3.26 show the impacts of the biases in lever-arm, boresight angles, range measurements, and

encoder angle scale factor on the derived point cloud, respectively. One should note that, in these equations, "*yaw*" denotes the flight direction; therefore, the quasi-rigorous method is not restricted to straight and parallel overlapping strips unlike the simplified method.
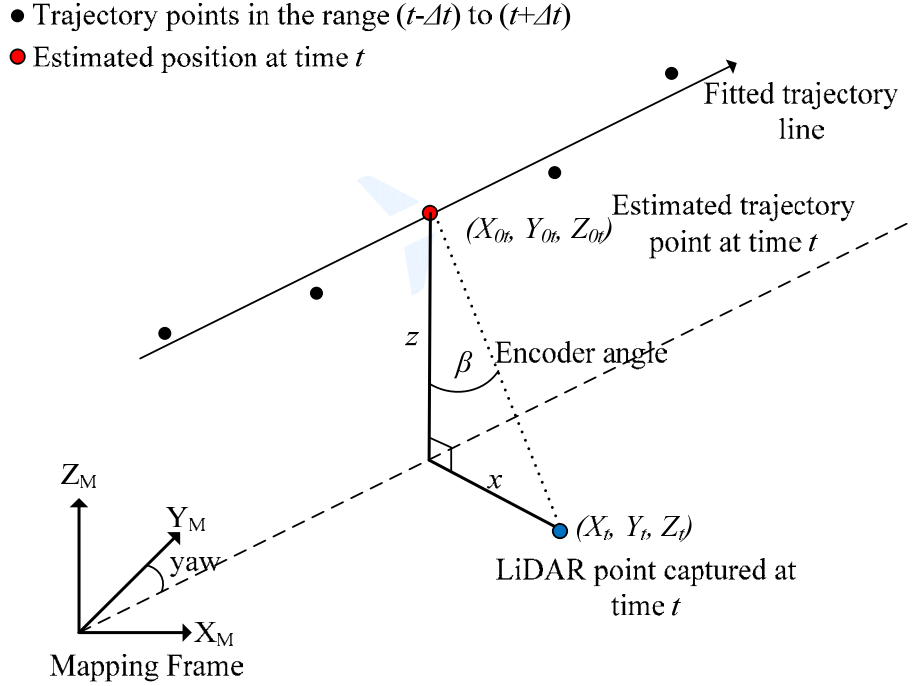
Figure 3.8. Lateral and vertical distance between the LiDAR point in question and the estimated firing point position using trajectory line fitting.

$$\frac{\partial f}{\partial \Delta X}\delta\Delta X + \frac{\partial f}{\partial \Delta Y}\delta\Delta Y + \frac{\partial f}{\partial \Delta Z}\delta\Delta Z = \begin{bmatrix} \cos(yaw)\delta\Delta X - \sin(yaw)\delta\Delta Y \\ \sin(yaw)\delta\Delta X + \cos(yaw)\delta\Delta Y \\ \delta\Delta Z \end{bmatrix} \quad (3.23)$$

$$\frac{\partial f}{\partial \Delta \omega}\delta\Delta\omega + \frac{\partial f}{\partial \Delta \varphi}\delta\Delta\varphi + \frac{\partial f}{\partial \Delta \kappa}\delta\Delta\kappa$$
$$= \begin{bmatrix} \sin(yaw)\,z\,\delta\Delta\omega + \cos(yaw)z\delta\Delta\varphi - \sin(yaw)\,x\delta\Delta\kappa \\ -\cos(yaw)\,z\delta\Delta\omega + \sin(yaw)\,z\delta\Delta\varphi + \cos(yaw)\,x\delta\Delta\kappa \\ -x\delta\Delta\varphi \end{bmatrix} \quad (3.24)$$

$$\frac{\partial f}{\partial \Delta \rho} \delta \Delta \rho = \begin{bmatrix} -\cos(yaw)\sin(S\beta)\delta\Delta\rho \\ -\sin(yaw)\sin(S\beta)\delta\Delta\rho \\ -\cos(S\beta)\delta\Delta\rho \end{bmatrix} \tag{3.25}$$

$$\frac{\partial f}{\partial S} \delta S = \begin{bmatrix} \cos(yaw)z\ \beta\delta S \\ \sin(yaw)z\ \beta\delta S \\ -x\ \beta\delta S \end{bmatrix} \tag{3.26}$$

The mathematical relationship between conjugate points in overlapping strips can be given by Equation 3.27 after merging Equations 3.23 to 3.26 for the overlapping strips (*A* and *B*) and subtracting the resulting equations from each other. Using Equation 3.27, one can recover the biases in the system parameters ($\delta\Delta X$, $\delta\Delta Y$, $\delta\Delta\omega$, $\delta\Delta\varphi$, $\delta\Delta\kappa$, δS, and $\delta\Delta\rho$) if trajectory position data and time-tagged point cloud coordinates are available. As long as we are dealing with overlapping strips, the vertical bias ($\delta\Delta Z$) in the lever-arm offsets cannot be recovered since the overlapping strips do not include discrepancies caused by this bias, which is previously discussed in section 3.2.

With the availability of control data, the mathematical relationship between control points and the LiDAR points can be derived by rewriting Equation 3.27 for the control surface (*A*) and LiDAR strip (*B*) and subtracting the resulting equations from each other. Since the bias effect terms do not exist for the control surface, the discrepancy between the control surface and LiDAR surface will be reduced to the form in Equation 3.28. Equations 3.27 and 3.28 are the final linearized equations for the quasi-rigorous calibration method, when dealing with overlapping strips and control surfaces, respectively. One should note that when control data over flat horizontal surfaces is employed (i.e., only vertical control is available), one cannot recover $\delta\Delta Z$ and $\delta\Delta\rho$ simultaneously due to the high correlation between these parameters since the value,

"$\cos(S\beta)\delta\Delta\rho$", is almost constant within nominal scan angle ranges. Control data over

flat horizontal surfaces will only contribute towards the estimation of the boresight roll

bias ($\delta\Delta\varphi$) and the encoder angle scale factor bias (δS) as can be seen in the 3rd row of

Equation 3.28. The use of control data over sloped surfaces will contribute towards the

estimation of all parameters and might help in decoupling $\delta\Delta Z$ and $\delta\Delta\rho$. Once the biases

are recovered, we can reconstruct the corrected point cloud using Equation 3.29. In this

equation, the terms $\delta\hat{\Delta}X$, $\delta\hat{\Delta}Y$, $\delta\hat{\Delta}Z$, $\delta\hat{\Delta}\omega$, $\delta\hat{\Delta}\varphi$, $\delta\hat{\Delta}\kappa$, $\delta\Delta\hat{\rho}$ and $\delta\hat{S}$ denote the

estimated biases in the system parameters.

$$
\begin{bmatrix} X_A \\ Y_A \\ Z_A \end{bmatrix}_{Biased} - \begin{bmatrix} X_B \\ Y_B \\ Z_B \end{bmatrix}_{Biased} = \begin{bmatrix} (\cos(yaw_A) - \cos(yaw_B))\delta\Delta X - (\sin(yaw_A) - \sin(yaw_B))\delta\Delta Y \\ (\sin(yaw_A) - \sin(yaw_B))\delta\Delta X + (\cos(yaw_A) - \cos(yaw_B))\delta\Delta Y \\ 0 \end{bmatrix} \quad (3.27)
$$

$$
+ \begin{bmatrix} (\sin(yaw_A)z_A - \sin(yaw_B)z_B)\delta\Delta\omega \\ -(\cos(yaw_A)z_A - \cos(yaw_B)z_B)\delta\Delta\omega \\ 0 \end{bmatrix} + \begin{bmatrix} (\cos(yaw_A)z_A - \cos(yaw_B)z_B)\delta\Delta\phi \\ (\sin(yaw_A)z_A - \sin(yaw_B)z_B)\delta\Delta\phi \\ -(x_A - x_B)\delta\Delta\phi \end{bmatrix}
$$

$$
+ \begin{bmatrix} -(\sin(yaw_A)x_A - \sin(yaw_B)x_B)\delta\Delta\kappa \\ (\cos(yaw_A)x_A - \cos(yaw_B)x_B)\delta\Delta\kappa \\ 0 \end{bmatrix} + \begin{bmatrix} -(\cos(yaw_A)\sin(S\beta_A) - \cos(yaw_B)\sin(S\beta_B))\delta\Delta\rho \\ -(\sin(yaw_A)\sin(S\beta_A) - \sin(yaw_B)\sin(S\beta_B))\delta\Delta\rho \\ -(\cos(S\beta_A) - \cos(S\beta_B))\delta\Delta\rho \end{bmatrix}
$$

$$
+ \begin{bmatrix} (\cos(yaw_A)z_A\beta_A - \cos(yaw_B)z_B\beta_B)\delta S \\ (\sin(yaw_A)z_A\beta_A - \sin(yaw_B)z_B\beta_B)\delta S \\ -(x_A\beta_A - x_B\beta_B)\delta S \end{bmatrix}
$$

$$
\begin{bmatrix} X_A \\ Y_A \\ Z_A \end{bmatrix}_{Control\ Surface} - \begin{bmatrix} X_B \\ Y_B \\ Z_B \end{bmatrix}_{Biased} = \begin{bmatrix} -\cos(yaw_B)\,\delta\Delta X + \sin(yaw_B)\delta\Delta Y \\ -\sin(yaw_B)\,\delta\Delta X - \cos(yaw_B)\delta\Delta Y \\ -\delta\Delta Z \end{bmatrix}
$$

$$
+ \begin{bmatrix} -\sin(yaw_B)z_B\,\delta\Delta\omega - \cos(yaw_B)z_B\,\delta\Delta\varphi + \sin(yaw_B)x_B\,\delta\Delta\kappa \\ \cos(yaw_B)z_B\,\delta\Delta\omega - \sin(yaw_B)z_B\,\delta\Delta\varphi - \cos(yaw_B)x_B\,\delta\Delta\kappa \\ x_B\,\delta\Delta\varphi \end{bmatrix} \quad (3.28)
$$

$$
+ \begin{bmatrix} \cos(yaw_B)\sin(S\beta_B)\delta\Delta\rho - \cos(yaw_B)z_B\beta_B\,\delta S \\ \sin(yaw_B)\sin(S\beta_B)\delta\Delta\rho - \sin(yaw_B)z_B\beta_B\,\delta S \\ \cos(S\beta_B)\delta\Delta\rho + x_B\beta_B\,\delta S \end{bmatrix}
$$

$$
\begin{bmatrix} X \\ Y \\ Z \end{bmatrix}_{Corrected} = \begin{bmatrix} X \\ Y \\ Z \end{bmatrix}_{Biased}
$$

$$
- \begin{bmatrix} \cos(yaw)\,\delta\hat{\Delta}X - \sin(yaw)\,\delta\hat{\Delta}Y + \sin(yaw)\,z\,\delta\hat{\Delta}\omega + \cos(yaw)\,z\,\delta\hat{\Delta}\varphi \\ \sin(yaw)\,\delta\hat{\Delta}X + \cos(yaw)\,\delta\hat{\Delta}Y - \cos(yaw)\,z\,\delta\hat{\Delta}\omega + \sin(yaw)\,z\,\delta\hat{\Delta}\varphi \\ \delta\hat{\Delta}Z - x\,\delta\hat{\Delta}\varphi \end{bmatrix}
$$

$$
- \begin{bmatrix} -\sin(yaw)\,x\,\delta\hat{\Delta}\kappa - \cos(yaw)\sin(S\beta)\,\delta\hat{\Delta}\rho + \cos(yaw)\,z\,\beta\,\hat{\delta S} \\ \cos(yaw)\,x\,\delta\hat{\Delta}\kappa - \sin(yaw)\sin(S\beta)\,\delta\hat{\Delta}\rho + \sin(yaw)\,z\,\beta\,\hat{\delta S} \\ -\cos(S\beta)\,\delta\hat{\Delta}\rho - x\,\beta\,\hat{\delta S} \end{bmatrix} \qquad (3.29)
$$

The procedure for estimating the necessary observations (x, z, yaw, and β) in Equations 3.27, 3.28, and 3.29 using the available data (time-tagged point cloud coordinates and trajectory position data) can be summarized as follows:

i) For a LiDAR point mapped at time t, we search in the trajectory file for positions within a certain time interval ($t - \Delta t$, $t + \Delta t$);

ii) A straight line is fitted through the selected trajectory positions to come up with a local estimate of the trajectory, as shown in Figure 3.8. After defining the flight path, the necessary observations can be estimated as follows:

-. The x-laser unit coordinate of the LiDAR point with respect to the laser unit frame, which is the lateral distance with the appropriate sign between the LiDAR point in question and the projection of the flight trajectory onto the ground, can be determined by computing the normal distance between the LiDAR point and the interpolated trajectory data. The intersection of the normal from the LiDAR point to the interpolated trajectory will define the position of the trajectory at time t;

-. The z-laser unit coordinate of the LiDAR point with respect to the laser unit frame can be determine by subtracting the elevation of the laser firing point (Z_{0t}) at time t, given by the interpolated flight trajectory, from the LiDAR point elevation (Z_t), i.e., $z = Z_t - Z_{0t}$ (Figure 3.8);

-. The *yaw* angle, which is the trajectory heading, can be computed once we have the local estimate of the trajectory and its direction (using the time tag of neighbouring trajectory positions); and

-. The β angle, which is the encoder angle indicating the laser beam direction with respect to the laser unit coordinate system, can be computed by a trigonometric operation using the estimated lateral distance (x) and the trajectory height (z) above the laser point in question.

One should note that, in this chapter, the proposed methods were derived based on point primitives. In other words, there was an implicit assumption that conjugate points are available between overlapping strips. However, it is not believed that distinct points are suitable for point cloud data. For this reason, the use of linear features and planar patches has been introduced as alternative primitives for point cloud data. The linear features defined by intersection of adjacent two planar patches have been used by Vosselman, 2002; Lee, 2007; Habib et al., 2008 because it is not easy to directly measure linear feature in point cloud data. Also, planar patches segmented from LiDAR data have been used by Pfeifer et al. 2005, Skaloud and Lichti, 2006; Habib and et al., 2007. The disadvantage of planar and linear features is that the alternative primitives can be reliably

extracted only in urban areas. In addition, the quality of plane segmentation affects the result of planar and linear feature extraction.

Instead of using well defined features for the co-alignment of point clouds, non-identifiable landmarks can be considered. In this work, the Iterative Closest Patch (ICPatch) is applied to establish point-patch correspondence between two overlapping strips. In this procedure, the original points represent the first strip while triangular patches, which can be derived from a TIN generation procedure, represent the second strip. Then, the ICPatch procedure establishes the correspondence between a LiDAR point in the first strip and a triangular patch in the second strip. To measure the similarity between corresponding point-patch pairs, the tetrahedron volume can be utilized. In addition, another approach using a modified weight matrix will be introduced as an point based similarity measure. This approach can handle point primitives after modifying a weight matrix even though true conjugate points are not available from the ICPatch procedure. The details of the surface matching procedure and modified weight matrix will be discussed in Chapter 4.

CHAPTER 4

PRIMITIVE AND SURFACE MATCHING

4.1 Introduction

In order to come up with a methodology for the determination of discrepancies between overlapping strips, one must address the following questions:

- What are the appropriate primitives, which can be used to identify conjugate surface elements in overlapping strips?

- What is the strategy for the derivation of these primitives?

- What is the appropriate similarity measure, which utilizes the involved primitives and the defined discrepancy functions to describe the correspondence of conjugate primitives in overlapping strips?

In Chapter 3, the proposed methods are based on utilizing discrepancies between conjugate points in overlapping strips for estimating biases in the system parameters. Point primitives have been commonly used in photogrammetric data registration; however, distinct points (e.g., building corner points) are not easily/reliably identifiable in irregularly distributed point data. Figures 4.1a and 4.1b show sample photogrammetric and LiDAR data captured over the same area, respectively. As shown in these figures, point features on man-made objects are easily identified in the stereo images (Figure 4.1a), while those features are not clearly observed in point cloud data (Figure 4.1b). Linear and areal features can be considered as alternative primitives. In photogrammetric data processing, linear features have been utilized in manual and automatic procedures

such as single photo resection, bundle adjustment, and camera calibration (Mulawa, 1989; Kubik, 1991; Habib et al., 2002; Habib and Morgan, 2003; Lee and Bethel, 2004). On the other hand, linear features can be extracted by the intersection of adjacent planes segmented from LiDAR data because linear features such as building boundaries and road lines cannot be directly captured by a LiDAR system as well as distinct points (Kraus and Pfeifer, 2001; Habib et al., 2005; Lee et al., 2007; Habib et al., 2008). Figure 4.1c shows linear features extracted from photogrammetric data, while the same linear features extracted by the intersection of planes segmented from LiDAR data are illustrated in Figure 4.1d. Planar patches have been also used as an alternative primitive, especially for the integration of photogrammetric and LiDAR data (Ghanma, 2006; Habib et al., 2007) and the co-alignment of point cloud data (Kager, 2004; Skaloud and Lichti, 2006; Bang, 2008). 3D planes can be defined by measuring vertices of a plane (such as a building roof) captured in multiple images (Figure 4.1e), while a plane segmentation procedure defines 3D planar patches in point cloud data (Figure 4.1d).

(a)

(b)

(c)

(d)

(e)
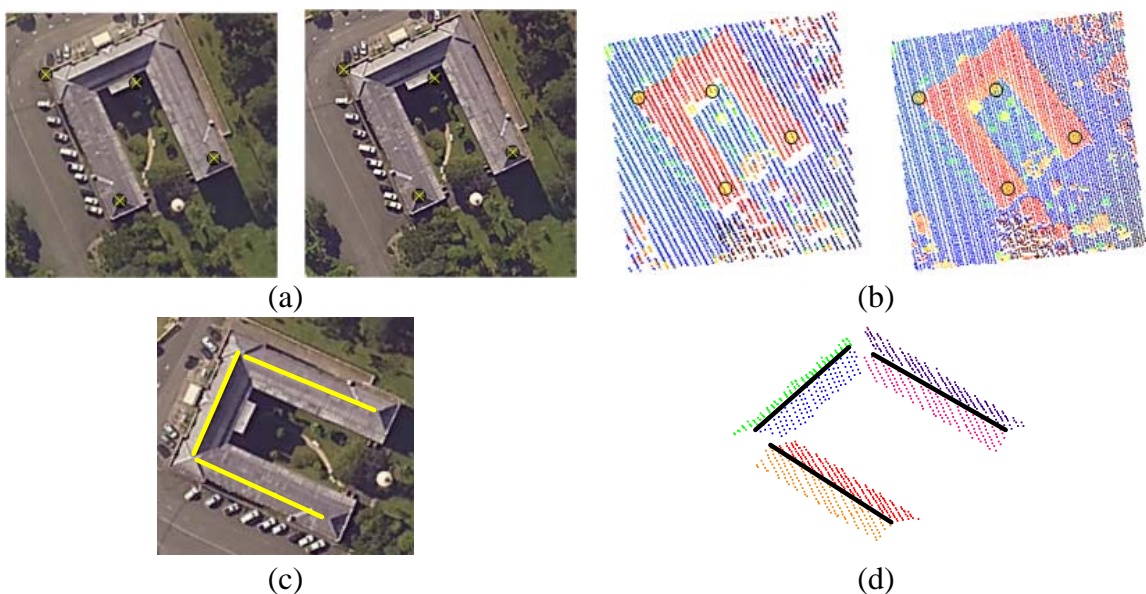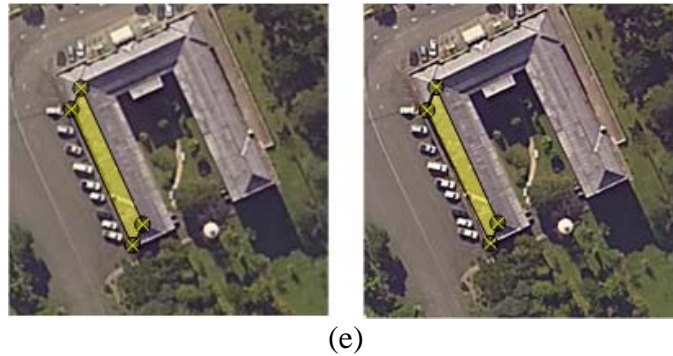
Figure 4.1. Points, linear features, and planar patches shown in photogrammetric and LiDAR data: (a) distinct points observed in stereo images, (b) point primitives shown in LiDAR overlapping strips, (c) linear features observed in photogrammetric data, (d) linear features extracted by intersection of adjacent planes segmented from LiDAR data, and (e) planar patch extracted from stereo images.

The drawback of the use of linear and areal features is that those primitives are usually available only in urban areas with man-made objects. Therefore, there is a lack of such objects in LiDAR data captured in rural areas. In addition, the accuracy of the linear features extracted by the plane intersection is affected by the quality of the plane segmentation procedure. Instead of extracting well defined features, a surface matching procedure can be considered as an alternative way to establishing correspondences between overlapping strips. The surface matching procedure has been used for point cloud co-alignment with the lack of identifiable landmarks (Zhang, 1994), and it is possible to establish the correspondences of point-point and point-patch in the overlapping area without the need to identify distinct features. The point-point correspondence can be established by ICP (Iterative Closest Point) procedure (Besl and McKay 1992; Zhang, 1994) which is an iterative procedure for finding correspondence between irregular point clouds. Similarly, another iterative approach, ICPatch (Iterative

Closest Patch) procedure, establishes point-patch correspondence between point cloud and TIN surfaces (Chen and Medioni, 1992; Li and Griffiths, 2000; Habib et al., 2006).

This research aims to select primitives that can be derived with minimal pre-processing of the original LiDAR points. Moreover, the selected primitives should be reliably derived regardless of object surface types such as urban and rural areas. To satisfy these objectives, the surface matching is used in this research. In the next section, the ICPatch procedure will be discussed while outlining how to evaluate the similarity (normal distance) between matched points and triangular patches as well as the involved mathematical models that encompass the simplified and quasi-rigorous calibration methods.

4.2 ICPatch Procedures with Volume Constraint

The ICPatch procedure finds the closest point-patch pairs from overlapping strips: one strip is represented by original points, and the other strip is represented by triangular patches which can be derived from a TIN generation procedure. In this research, the volume constraint is introduced as a similarity measure between matched point-patch pairs derived from the ICPatch procedure. Figure 4.2 illustrates the case where the strip denoted by "A" is represented by a set of triangular patches while the other strip denoted by "B" is represented by a set of irregular points. The surface matching procedure establishes the correspondence between a LiDAR point ($\vec{q}$) in strip B and a triangular patch (defined by the vertices $\vec{S}_{pa}$, $\vec{S}_{pb}$, and $\vec{S}_{pc}$) in strip A.
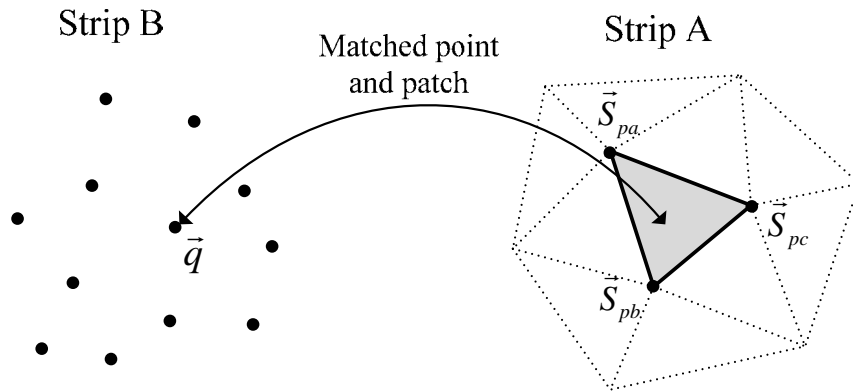
Figure 4.2. Conceptual basis of the proposed point-patch correspondence procedure.

TIN patches are acceptable to describe the physical surface due to the high density of the LiDAR data as well as the relatively smooth characteristics of terrain and man-made structures. Therefore, point-patch correspondences would be valid in overlapping strips represented by point cloud and TIN. However, there are some exceptions where the TIN patches would not represent the physical surface. In Figure 4.3a, the image shows that the object surface consists of buildings, trees, and ground, while Figure 4.3b shows overlapping strips captured in the same area, where strips A and B are represented by TIN and point cloud, respectively. As one can see in Figure 4.3b, TIN patches can successfully represent the physical surface along the ground and building roofs; however, this is not the case over the vegetation and around the building roof boundaries. TIN patches within the trees and along the transition from building roof boundaries to the ground do not represent physical surfaces. Figure 4.3c illustrates the result of the surface matching procedure, where blue points denote matched points, while red points indicate un-matched points. As it can be seen in this figure, most un-matched points are located at building boundaries/walls and trees. In summary, although one cannot assume that there is point-point correspondence between overlapping LiDAR strips, one can argue that

point-patch correspondence is available as long as the patch represents the physical surface.

(a)   (b)

(c)
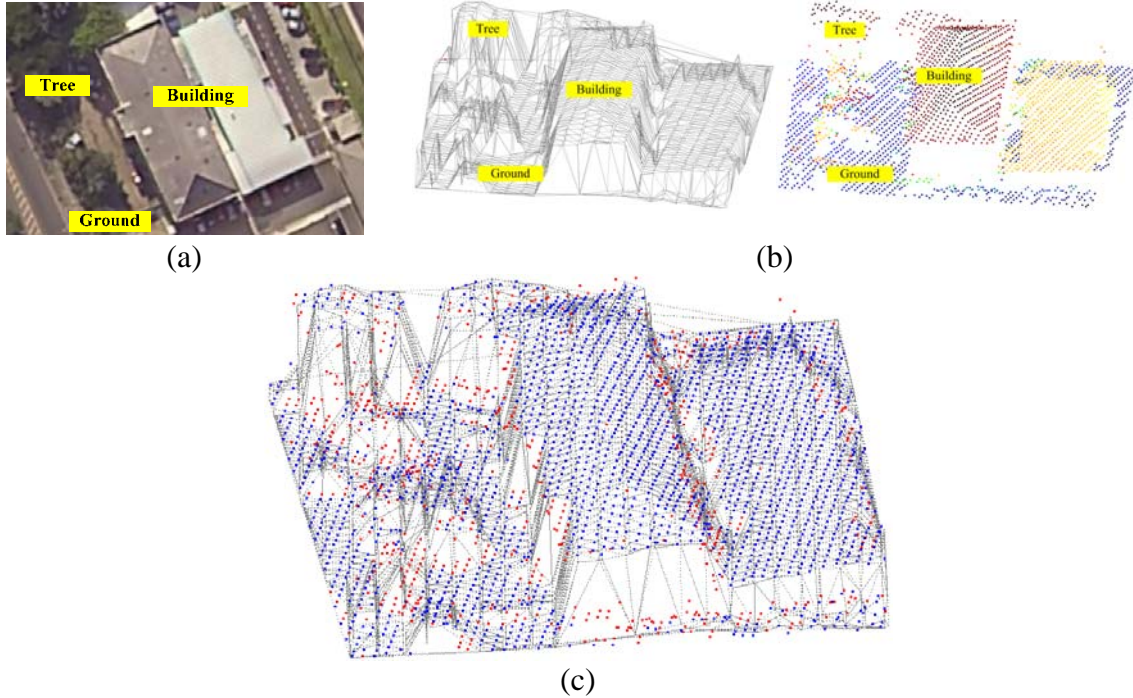
Figure 4.3. (a) An image captured over the object surface, (b) overlapping strips represented by TIN (strip A) and point cloud (strip B), and (c) matched (blue) and un-matched (red) points.

In Figure 4.2, if the point $\vec{q}$ in strip B (point cloud) belongs to the triangular patch represented by the vertices $\vec{S}_{pa}$, $\vec{S}_{pb}$, and $\vec{S}_{pc}$ in strip A (TIN), then this point should coincide with that patch. As known in the previous research (Habib et al., 2001; Habib et al., 2006; Ghanma, 2006), the similarity can be measured by the volume of the tetrahedron whose vertices are $\vec{q}$, $\vec{S}_{pa}$, $\vec{S}_{pb}$, and $\vec{S}_{pc}$ (Figure 4.4). The volume constraints can be mathematically described by Equation 4.1a which is the determinant formed by the coordinates of the tetrahedron vertices. It can be rewritten by Equation 4.1b after expanding Equation 4.1a. To estimate systematic biases using matched point-

patch pairs in overlapping strips and volume constraint, Equation 4.1b should be integrated with the transformation function and LiDAR geo-referencing equation for the simplified and quasi-rigorous methods. In the following sub-sections, the manipulation of the volume constraint will be discussed with respect to the proposed methods.
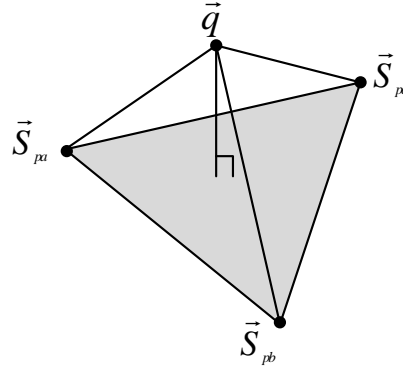
Figure 4.4. Corresponding triangular patch and point constitute a tetrahedron.

$$D = \begin{vmatrix} X_q & Y_q & Z_q & 1 \\ X_{pa} & Y_{pa} & Z_{pa} & 1 \\ X_{pb} & Y_{pb} & Z_{pb} & 1 \\ X_{pc} & Y_{pc} & Z_{pc} & 1 \end{vmatrix}$$

(4.1a)

where,

(X_q, Y_q, Z_q) denote the coordinates of $\vec{q}$;

$(X_{pa}, Y_{pa}, Z_{pa}),(X_{pb}, Y_{pb}, Z_{pb})$, and (X_{pc}, Y_{pc}, Z_{pc}) denote the coordinates of the vertices, $\vec{S}_{pa}$, $\vec{S}_{pb}$, and $\vec{S}_{pc}$, respectively.

$$f_{\det} = D = d_1 X_q + d_2 Y_q + d_3 Z_q + d_4$$

(4.1b)

where,

$$d_1 = \begin{vmatrix} Y_{pa} & Z_{pa} & 1 \\ Y_{pb} & Z_{pb} & 1 \\ Y_{pc} & Z_{pc} & 1 \end{vmatrix} = Y_{pa}(Z_{pb} - Z_{pc}) - Z_{pa}(Y_{pb} - Y_{pc}) + (Y_{pb}Z_{pc} - Y_{pc}Z_{pb});$$

$$d_2 = - \begin{vmatrix} X_{pa} & Z_{pa} & 1 \\ X_{pb} & Z_{pb} & 1 \\ X_{pc} & Z_{pc} & 1 \end{vmatrix} = -X_{pa}(Z_{pb} - Z_{pc}) + Z_{pa}(X_{pb} - X_{pc}) - (X_{pb}Z_{pc} - X_{pc}Z_{pb});$$

$$d_3 = \begin{vmatrix} X_{pa} & Y_{pa} & 1 \\ X_{pb} & Y_{pb} & 1 \\ X_{pc} & Y_{pc} & 1 \end{vmatrix} = X_{pa}(Y_{pb} - Y_{pc}) - Y_{pa}(X_{pb} - X_{pc}) + (X_{pb}Y_{pc} - X_{pc}Y_{pb});$$

$$d_4 = - \begin{vmatrix} X_{pa} & Y_{pa} & Z_{pa} \\ X_{pb} & Y_{pb} & Z_{pb} \\ X_{pc} & Y_{pc} & Z_{pc} \end{vmatrix} = -X_{pa}(Y_{pb}Z_{pc} - Y_{pc}Z_{pb}) + Y_{pa}(X_{pb}Z_{pc} - X_{pc}Z_{pb}) - Z_{pa}(X_{pb}Y_{pc} - X_{pc}Y_{pb}).$$

4.2.1 Volume Constraint for the Simplified Method

For the simplified method, the discrepancies between overlapping strips can be represented by a 4-parameter 3D transformation function. As shown in Equation 4.2, the matched point $\vec{q}$ in strip B can be represented by a function of the bias-contaminated coordinates ($\vec{q}_0$) and four transformation parameters. The best estimation of the transformation parameters (three shifts and one rotation angle) between two datasets can be determined when the estimated transformation parameters in Equation 4.2 minimize the determinant (Equation 4.1b) for all the matched point-patch pairs. Equation 4.3 represents the combination of the transformation function and volume constraint.

$$\vec{q} = \begin{bmatrix} X_T \\ Y_T \\ Z_T \end{bmatrix} + R_{(0,\varphi,0)}\vec{q}_0 \tag{4.2}$$

$$f_{\det} = \begin{bmatrix} d_1 & d_2 & d_3 \end{bmatrix} \left(\begin{bmatrix} X_T \\ Y_T \\ Z_T \end{bmatrix} + R_{(0,\varphi,0)}\vec{q}_0 \right) + d_4 \tag{4.3}$$

For a least square adjustment procedure, Gauss-Helmert model is used because the bias-contaminated vertex coordinates (observed values) and unknown parameters (transformation parameters) are not separable (Mikhail and Ackerman, 1976; Wolf and Ghilani, 1997; Koch, 1999; McGlone et al., 2004). Equation 4.4 represents the Gauss-Helmert adjustment model for the simplified method. In this equation, A is the design matrix of partial derivatives of Equation 4.3 taken with respect to the four transformation parameters; δ denotes the corrections to the approximate transformation parameters; B is the design matrix of partial derivatives of Equation 4.3 taken with respect to the vertex coordinates; v and w are the observation error vectors of the vertex coordinates and misclosure vector, respectively. The solution of the Gauss-Helmert adjustment model is derived by Equation 4.5, where $\Sigma_{\vec{q}\vec{S}_{pa}\vec{S}_{pb}\vec{S}_{pc}}$ is the a-priori variance-covariance matrix of the vertex coordinates.

$$A\delta + Bv = w \tag{4.4}$$

$$\hat{\delta} = [A^T (B \ \Sigma_{\vec{q}\vec{S}_{pa}\vec{S}_{pb}\vec{S}_{pc}} \ B^T)^{-1} \ A]^{-1} \ A^T (B \ \Sigma_{\vec{q}\vec{S}_{pa}\vec{S}_{pb}\vec{S}_{pc}} \ B^T)^{-1} \ w \tag{4.5}$$

After estimating the transformation parameters, the biases in the system parameters can be derived by Equations 4.6a, 4.6b, and 4.6c using the estimated transformation parameters. Equations 4.6a, 4.6b, and 4.6c pertain to the three parallel overlapping cases: opposite flight directions, opposite flight directions with 100% overlap ratio, and same flight directions, respectively. In these equations, $\hat{X}_T$, $\hat{Y}_T$, $\hat{Z}_T$, and $\hat{\varphi}$ denote estimated transformation parameters from Equation 4.5; $\delta\Delta X$, $\delta\Delta Y$, $\delta\Delta\omega$, $\delta\Delta\varphi$, $\delta\Delta\kappa$, $\delta\Delta\rho$, and δS denote biases in the system parameters.

$$\begin{bmatrix} \hat{X}_T \\ \hat{Y}_T \\ \hat{\varphi} \end{bmatrix} = \begin{bmatrix} 2\,\delta\Delta X - 2\,H\,\delta\Delta\varphi \mp D/H\,\delta\Delta\rho \mp H\beta_T\delta S \\ 2\,\delta\Delta Y + 2\,H\,\delta\Delta\omega \mp D\,\delta\Delta\kappa \\ 2\delta\Delta\varphi \pm 2\beta_T\delta S \end{bmatrix} \tag{4.6a}$$

$$\begin{bmatrix} \hat{X}_T \\ \hat{Y}_T \\ \hat{\varphi} \end{bmatrix} = \begin{bmatrix} 2\,\delta\Delta X - 2\,H\,\delta\Delta\varphi \\ 2\,\delta\Delta Y + 2\,H\,\delta\Delta\omega \\ 2\delta\Delta\varphi \end{bmatrix} \tag{4.6b}$$

$$\begin{bmatrix} \hat{X}_T \\ \hat{Y}_T \\ \hat{Z}_T \\ \hat{\varphi} \end{bmatrix} = \begin{bmatrix} -D/H\,\delta\Delta\rho - H\beta_T\delta S \\ -D\,\delta\Delta\kappa \\ D\,\delta\Delta\varphi \\ 2\beta_T\delta S \end{bmatrix} \tag{4.6c}$$

4.2.2   Volume Constraint for the Quasi-rigorous Method

The quasi-rigorous method represents the four vertices ($\vec{q}$, $\vec{S}_{pa}$, $\vec{S}_{pb}$, and $\vec{S}_{pc}$) of the tetrahedron using a function of the bias-contaminated coordinates, systematic biases, and calculated values such as *yaw*, *x*, *z*, and *β*. In Equation 4.7, $\vec{P}_0$ denotes bias-contaminated coordinates of a vertex constituting a tetrahedron, while $\vec{P}$ represents adjusted coordinates after removing the impact of the systematic biases. In this equation, *yaw*, *x*, *z*, and *β* which can be calculated values through the trajectory line fitting procedure represent the flight direction, lateral and vertical coordinates of a LiDAR point, and laser beam direction with respective to the laser unit coordinate system (refer to section 3.3 for more information). For the quasi-rigorous method, the volume constraints are realized by Equation 4.8 which is the combination of Equations 4.7 and 4.1b. In this equation, $\vec{x}$ denotes the biases in the system parameters; the calculated values (*yaw*, *x*, *z*, and *β*) are represented by $\vec{l}$ for each vertex point. One should note that d_1, d_2, d_3, and d_4 in

Equation 4.8 are functions of *yaw*, *x*, *z*, *β*, bias-contaminated coordinates, and systematic

biases in contrast to the volume constraint used in the simplified method. Using Equation

4.8, the biases in the system parameters are determined as unknowns when the volume of

the tetrahedron is minimized for all the matched point-patch.

$$f(\vec{P}_0, \vec{x}, \vec{l}) = \vec{P} = \vec{P}_0 - \begin{bmatrix} \cos(yaw)\delta\Delta X - \sin(yaw)\delta\Delta Y + \sin(yaw) z \,\delta\Delta\omega + \cos(yaw) z \delta\Delta\varphi \\ \sin(yaw)\delta\Delta X + \cos(yaw)\delta\Delta Y - \cos(yaw) z \,\delta\Delta\omega + \sin(yaw) z \delta\Delta\varphi \\ \delta\Delta Z - x \,\delta\Delta\varphi \end{bmatrix}$$
$$- \begin{bmatrix} -\sin(yaw) x\delta\Delta\kappa - \cos(yaw)\sin(S\beta)\delta\Delta\rho + \cos(yaw) z \,\beta\delta S \\ \cos(yaw) x\delta\Delta\kappa - \sin(yaw)\sin(S\beta)\delta\Delta\rho + \sin(yaw) z \,\beta\delta S \\ -\cos(S\beta)\delta\Delta\rho - x \,\beta\delta S \end{bmatrix} \quad (4.7)$$

$$f_{\text{det}} = \begin{bmatrix} d_1 & d_2 & d_3 \end{bmatrix} f(\vec{q}_0, \vec{x}, \vec{l}_q) + d_4 \quad (4.8)$$

where,

$$d_1 = f(Y_{pa0}, Y_{pb0}, Y_{pc0}, Z_{pa0}, Z_{pb0}, Z_{pc0}, \vec{x}, \vec{l}_{pa}, \vec{l}_{pb}, \vec{l}_{pc}),$$

$$d_2 = f(X_{pa0}, X_{pb0}, X_{pc0}, Z_{pa0}, Z_{pb0}, Z_{pc0}, \vec{x}, \vec{l}_{pa}, \vec{l}_{pb}, \vec{l}_{pc}),$$

$$d_3 = f(X_{pa0}, X_{pb0}, X_{pc0}, Y_{pa0}, Y_{pb0}, Y_{pc0}, \vec{x}, \vec{l}_{pa}, \vec{l}_{pb}, \vec{l}_{pc}), \text{ and}$$

$$d_4 = f(X_{pa0}, X_{pb0}, X_{pc0}, Y_{pa0}, Y_{pb0}, Y_{pc0}, Z_{pa0}, Z_{pb0}, Z_{pc0}, \vec{x}, \vec{l}_{pa}, \vec{l}_{pb}, \vec{l}_{pc}).$$

The solution of the Gauss-Helmert adjustment model for the quasi-rigorous method is

represented by Equation 4.9, where *A* is the design matrix of partial derivatives of

Equation 4.8 taken with respect to the systematic biases introduced in Equation 4.7; δ

denotes the corrections to the approximate systematic biases; *B* is the design matrix of the

vertex coordinates ($\vec{q}$ and $\vec{S}_{pa}$) and calculated values (*yaw*, *x*, *z*, and *β*) denoted by ($\vec{l}$);

w is the misclosure vector of the volume constraints; $\Sigma_{\vec{q}\vec{S}_{pa}\vec{l}_{\vec{q}}\vec{l}_{\vec{S}_{pa}}\vec{l}_{\vec{S}_{pb}}\vec{l}_{\vec{S}_{pc}}}$ denotes the a-priori

variance-covariance matrix derived by the accuracies of the LiDAR points and calculated *yaw*, *x*, *z*, and *β*.

$$\hat{\delta} = [A^T (B \, \Sigma_{\vec{q}\vec{S}_{pa}\vec{l}_{\vec{q}}\vec{l}_{\vec{S}_{pa}}\vec{l}_{\vec{S}_{pb}}\vec{l}_{\vec{S}_{pc}}} \, B^T)^{-1} \, A]^{-1} \, A^T (B \, \Sigma_{\vec{q}\vec{S}_{pa}\vec{l}_{\vec{q}}\vec{l}_{\vec{S}_{pa}}\vec{l}_{\vec{S}_{pb}}\vec{l}_{\vec{S}_{pc}}} \, B^T)^{-1} \, w \qquad (4.9)$$

4.3   Modified Weight Matrix

In the previous section, the similarity was measured by the volume of the tetrahedron consisting of the matched point-patch pair. In addition to the volume constraint, this section introduces a point-based similarity measure. In this approach, one can establish correspondences between overlapping strips using pseudo-conjugate points and their modified weight matrices which can be derived from matched point-patch pairs.

Figure 4.5 illustrates a point-patch pair, where the point $\vec{q}$ and triangular patch defined by $\vec{S}_{pa}$, $\vec{S}_{pb}$, and $\vec{S}_{pc}$ denote the matched point-patch pair. In this figure, $\vec{S}_{pa}$ is an arbitrarily selected vertex from the triangular patch as a corresponding point to the point $\vec{q}$ in the other strip. One should note that the corresponding two points ($\vec{q}$ and $\vec{S}_{pa}$) are pseudo-conjugate points. To compensate this non-corresponding problem, weight matrices for the pseudo-conjugate points are modified using surface normal vectors of the matched triangular patches. Specifically, for the vertex point $\vec{S}_{pa}$, a certain weight value determined by the precision of LiDAR data will be assigned along the surface normal, while zero weights will be assigned along the patch plane. By doing this, the non-corresponding problem of the point $\vec{S}_{pa}$ can be compensated. The following sections will show the manipulation of the modified weight matrix for the transformation function of the simplified method and LiDAR geo-referencing equation of the quasi-rigorous method.
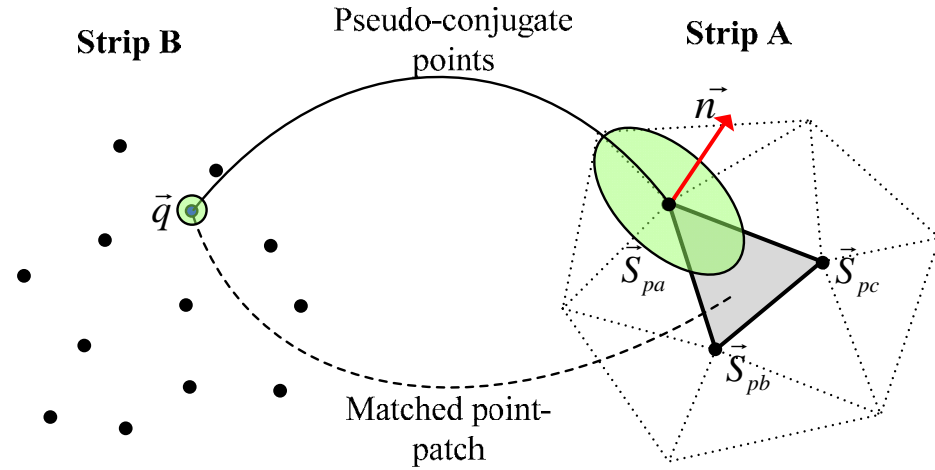
Figure 4.5. The matched point-patch pair and corresponding points; the vertex $\vec{S}_{pa}$ which is arbitrarily selected from the triangular patch (strip A) corresponds to the point $\vec{q}$ (strip B).

4.3.1 Modified Weight Matrix for the Simplified Method

Equation 4.10 represents the discrepancies between corresponding points after applying the transformation function. In this equation, $\vec{q}$ denotes a matched point of a strip represented by a point cloud and $\vec{S}_{pa}$ is an arbitrarily selected vertex point of a matched triangular patch in another strip represented by TIN. To solve Equation 4.10, the weight matrix for the pseudo-conjugate points ($\vec{q}$ and $\vec{S}_{pa}$) will be modified to compensate for the fact that they are not true conjugate points.

$$f(\vec{S}_{pa0}, \vec{q}_0, X_T, Y_T, Z_T, \varphi) = \vec{S}_{pa0} - \begin{bmatrix} X_T \\ Y_T \\ Z_T \end{bmatrix} - R_{(0,\varphi,0)}\vec{q}_0 \tag{4.10}$$

The modified weight matrix utilizes a local coordinate system (*UVW*) with the following axes-definition: *W* axis parallel to the patch normal and *U* and *V* axes aligned along the triangular plane. In this research, *U* axis is aligned along the triangle side $\overline{S_{pa}S_{pb}}$, while the *V* axis is parallel to the *U-W* plane normal (Figure 4.6). It should be mentioned that the *U* and *V* axes can be arbitrarily chosen as long as the *UV* plane is parallel to the triangular patch. The relationship between the strip coordinate system (*XYZ*) and the local coordinate system (*UVW*) can be represented by Equation 4.11. In this equation, R_{UVW}^{XYZ} is the rotation matrix defining the orientation of the triangular patch. Equation 4.12 shows the derivation of the rotation matrix R_{UVW}^{XYZ} as follows: the three vectors ($\vec{V}_U$, $\vec{V}_V$, and $\vec{V}_W$) parallel to *UVW* axes are determined by the three vertices; then, the determined $\vec{V}_U$, $\vec{V}_V$, and $\vec{V}_W$ define the direction cosines which constitute the rotation matrix.
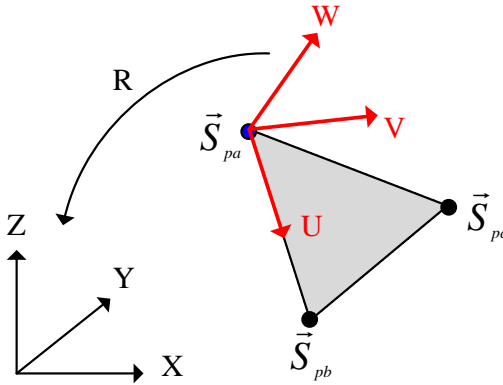
Figure 4.6. The Definition of the local coordinate system (*UVW*).

$$\begin{bmatrix} X \\ Y \\ Z \end{bmatrix} = R_{UVW}^{XYZ} \begin{bmatrix} U \\ V \\ W \end{bmatrix} \qquad (4.11)$$

$$R_{UVW}^{XYZ} = \begin{bmatrix} r_{11} & r_{12} & r_{13} \\ r_{21} & r_{22} & r_{23} \\ r_{31} & r_{32} & r_{33} \end{bmatrix} = \begin{bmatrix} \dfrac{\vec{V}_U}{\left\| \vec{V}_U \right\|} & \dfrac{\vec{V}_V}{\left\| \vec{V}_V \right\|} & \dfrac{\vec{V}_W}{\left\| \vec{V}_W \right\|} \end{bmatrix} \tag{4.12}$$

where,

$\vec{V}_U = \vec{S}_{pb} - \vec{S}_{pa}$,

$\vec{V}_W = \vec{V}_U \times (\vec{S}_{pc} - \vec{S}_{pa})$, and

$\vec{V}_V = \vec{V}_W \times \vec{V}_U$.

In Equation 4.13, the original weight matrix P_{XYZ} is defined as the inverse of $(B\Sigma_{\vec{q}\vec{S}_{pa}} B^T)$ where B is the design matrix of partial derivatives of Equation 4.10 taken with respect to the pseudo-conjugate point coordinates; the a-priori variance-covariance matrix $\Sigma_{\vec{q}\vec{S}_{pa}}$ derived by the accuracy specification of the data acquisition system. Using the law of error propagation, the weight of that vertex point in the local coordinate system P_{UVW} can be derived by Equation 4.14. As it has been noted earlier, the weight along the triangle plane normal is the only useful information when working with pseudo-conjugate points along matched point-patch pairs. Therefore, the weight matrix can be modified as in Equation 4.15. Finally, the modified weight matrix P'_{XYZ} in the strip coordinate system can be derived by Equation 4.16. After modifying the weight matrix, the corrections to the approximate transformation are determined by Equation 4.17 and the biases in the system parameters are determined by Equations 4.6a, 4.6b, and 4.6c. In Equation 4.17, A is the design matrix of partial derivatives of Equation 4.10 taken with respect to the transformation parameters; w is the misclosure vector represented the differences (dX, dY, and dZ) between the pseudo-conjugate points ($\vec{q}$ and $\vec{S}_{pa}$) after applying the

transformation function to the point $\vec{q}_0$. The best estimation of the transformation parameters is determined when the weighted squared-sum of the misclosure vector (w) in Equation 4.18 is minimized. In this equation, one can confirm that the modified weight matrix minimizes the normal distance which is represented by dW in the UVW coordinates system.

$$P_{XYZ} = (B\Sigma_{\vec{q}\vec{S}_{pa}} B^T)^{-1} \tag{4.13}$$

where,

$\Sigma_{\vec{q}\vec{S}_{pa}}$ is the a-priori variance-covariance matrix of LiDAR points.

$$P_{UVW} = R_{UVW}^{XYZ}{}^T P_{XYZ} R_{UVW}^{XYZ} = \begin{bmatrix} P_U & P_{UV} & P_{UW} \\ P_{VU} & P_V & P_{VW} \\ P_{WU} & P_{WV} & P_W \end{bmatrix} \tag{4.14}$$

$$P'_{UVW} = \begin{bmatrix} 0 & 0 & 0 \\ 0 & 0 & 0 \\ 0 & 0 & P_W \end{bmatrix} \tag{4.15}$$

$$P'_{XYZ} = R_{UVW}^{XYZ} P'_{UVW} R_{UVW}^{XYZ}{}^T \tag{4.16}$$

$$\hat{\delta} = [A^T P'_{XYZ} A]^{-1} A^T P'_{XYZ} w \tag{4.17}$$

$$
\begin{aligned}
&\Sigma(w^T P'_{XYZ} w) \\
&= \Sigma\left[\left(\vec{S}_{pa0} - [X_T \quad Y_T \quad Z_T]^T - R_{(0,\varphi,0)}\vec{q}_0\right)^T P'_{XYZ}\left(\vec{S}_{pa0} - [X_T \quad Y_T \quad Z_T]^T - R_{(0,\varphi,0)}\vec{q}_0\right)\right] \\
&= \Sigma([dX \quad dY \quad dZ]P'_{XYZ}[dX \quad dY \quad dZ]^T) \\
&= \Sigma([dX \quad dY \quad dZ]R_{UVW}^{XYZ} P'_{UVW} R_{UVW}^{XYZ}{}^T[dX \quad dY \quad dZ]^T) \\
&= \Sigma([dU \quad dV \quad dW]\begin{bmatrix} 0 & 0 & 0 \\ 0 & 0 & 0 \\ 0 & 0 & P_W \end{bmatrix}[dU \quad dV \quad dW]^T) = \Sigma P_W dW^2 \to \min
\end{aligned}
\tag{4.18}
$$

The evaluation of the redundancy in the calibration procedure will be based on the rank of the weight matrix for the individual points. For a corresponding point belonging to a

matched triangular patch, whose weight matrix is manipulated according to Equation 4.15, a contribution of one will be considered towards the redundancy computation (i.e., one effective equation constraint).

4.3.2 Modified Weight Matrix for the Quasi-rigorous Method

Equation 4.19 represents the discrepancies between bias-contaminated coordinates of corresponding LiDAR points ($\vec{q}_0$ and $\vec{S}_{pa0}$) after removing the impact of the biases in the system parameters. In this equation, f denotes Equation 4.7 which is the function to define adjusted LiDAR coordinates using the bias-contaminated coordinates, systematic biases ($\vec{x}$), and calculated values ($\vec{l}$) such as *yaw*, *x*, *z*, and *β*. Equation 4.20 represents the weight matrix P_{XYZ} defined in the *XYZ* coordinate system, where $\Sigma_{\vec{q}\vec{S}_{pa}\vec{l}_{\vec{q}}\vec{l}_{\vec{S}_{pa}}}$ denotes the a-priori variance-covariance matrix derived by the pre-determined accuracies of the LiDAR points and calculated *yaw*, *x*, *z*, and *β*; *B* is the design matrix of partial derivatives of Equation 4.19 taken with respect to the pseudo-conjugate point coordinates and their calculated values (*yaw*, *x*, *z*, and *β*). After calculating the modified weight matrix (P'_{XYZ}) in a similar way in the previous section, the biases in the system parameters are determined by Equation 4.21. In this equation, *A* is the design matrix of partial derivatives of Equation 4.19 taken with respect to the systematic biases and *w* is the misclosure vector represented by the discrepancies (*dX*, *dY*, and *dZ*) between the pseudo-conjugate points after removing the impact of the biases in the system parameters. One should note that the best estimation of the biases in the system parameters is determined when the weighted squared-sum of the misclosure vector (*w*) in Equation 4.22 is

minimized. As shown in Equation 4.22, the modified weight matrix contributes to minimizing the normal distance (*dW*) between the matched point-patch pair.

$$f(\vec{S}_{pa0}, \vec{x}, \vec{l}_{pa}) - f(\vec{q}_0, \vec{x}, \vec{l}_q) = \vec{S}_{pa} - \vec{q} = w \tag{4.19}$$

where,

$\vec{x}$ is biases in the system parameters, and

$\vec{l}_{pa}$ and $\vec{l}_q$ are the calculated values (yaw, x, z, and β) for the corresponding points $\vec{S}_{pa}$ and $\vec{q}$, respectively.

$$P_{XYZ} = (B\Sigma_{\vec{q}\vec{S}_{pa}\vec{l}_{\vec{q}}\vec{l}_{\vec{S}_{pa}}} B^T)^{-1} \tag{4.20}$$

$$\hat{\delta} = [A^T P'_{XYZ} A]^{-1} A^T P'_{XYZ} w \tag{4.21}$$

$$\Sigma(w^T P'_{XYZ} w)$$

$$= \Sigma\left[\left(\vec{S}_{pa} - \vec{q}\right)^T R_{UVW}^{XYZ} \begin{bmatrix} 0 & 0 & 0 \\ 0 & 0 & 0 \\ 0 & 0 & P_W \end{bmatrix} R_{UVW}^{XYZ\,T} \left(\vec{S}_{pa} - \vec{q}\right) \right]$$

$$= \Sigma([dU \quad dV \quad dW] \begin{bmatrix} 0 & 0 & 0 \\ 0 & 0 & 0 \\ 0 & 0 & P_W \end{bmatrix} [dU \quad dV \quad dW]^T) = \Sigma P_W dW^2 \rightarrow \min \tag{4.22}$$

The advantage of the modified weight matrix is that there is no change in the mathematical model of the adjustment procedure except manipulating the weight matrix regardless the type of utilized primitives such as points, linear features, and/or planar patches (if those are available). In addition, the mathematical model is relatively simple and easy to be implemented since there is no requirement to combine an additional equation representing alternative similarity measures such as normal distance or volume constraints. The next section will introduce the matching strategy and iterative procedure of updating matched point-patch pairs.

4.4 Surface Matching Strategy

After introducing the necessary similarity measure and the solution of the least square adjustment, one needs to propose a surface matching strategy for establishing the correspondences between points in strip A and patches in strip B. The approach proposed by Habib and Cheng (2006) deals with the point-patch matching problem in the presence of significant rotations and shifts between two overlapping surfaces. For such a case, the Modified Iterated Hough Transform (MIHT) is used to sequentially estimate the transformation parameters through a voting scheme in an accumulator array. For the current research, the correspondence is performed in an iterated manner, using the ICPatch procedure, which corresponds to the ICP approach (Besl and McKay, 1992; Zhang, 1994; Bergevin et al., 1996) after some modification. The initial correspondence between points and triangular patches can be established by determining the patch with the shortest normal distance to the point. Since the involved surfaces are co-aligned to a high degree of accuracy, it is reasonable to assume that the initial parameters (transformation parameters for the simplified method and systematic biases for the quasi-rigorous method) are zero. To be considered a correct match, the shortest normal distance should be less than a given threshold to avoid situations where the triangular patch does not represent the physical surface (e.g., in vegetation and building boundaries as shown in Figure 4.3). Moreover, the projection of the corresponding point onto the corresponding triangular patch should be located inside the corresponding triangular patch.

The ICPatch procedure is an iterative procedure for updating the matched point-patch pairs after estimating the transformation parameters/systematic biases. For the iterative

surface matching procedure, the simplified method transforms the bias-contaminated coordinates of the point cloud after estimating unknown transformation parameters based on the matched point-patch pairs. In the next iteration, matched point-patch pairs are updated using the transformed coordinates of the point cloud; then the transformation parameters can be re-estimated based on the new matched point-patch pairs. One should note that even though the procedure find the closest point-patch pairs is conducted by the transformed coordinates, the unknown transformation parameters should be estimated based on the original bias-contaminated coordinates. This iterative procedure will stop when the differences between the last and previous estimated transformation parameters are less than a threshold pre-defined by users. After estimating the best transformation parameters of all overlapping strip pairs, the biases of the system parameters can be calculated. In contrast to the simplified method, the quasi-rigorous method adjusts all the points of point cloud and TIN data using the estimated biases in the system parameters. After adjusting the point and vertex coordinates, the matching procedure updates the closest point-patch pairs based on the adjusted point coordinates. New systematic biases are estimated based on the updated point-patch pairs and original bias-contaminated coordinates. This procedure is repeated until convergence, where there is no significant change in the estimated biases larger than a given threshold. After finishing the ICPatch procedure of the simplified or quasi-rigorous methods, LiDAR strips can be adjusted using the estimated biases. Figure 4.7 illustrates the flowchart of the proposed calibration methods. In this flow chart, the white boxes denote common procedures shared with both the simplified and quasi-rigorous methods; the yellow boxes belong to the simplified method, while the green boxes belong to the quasi-rigorous method.

89

Input data

<Quasi-rigorous method> Trajectory Data

Strip A

TIN Generation

<Quasi-rigorous method> Control data if available

Strip B

<Quasi-rigorous method> Trajectory line fitting and firing point estimation

<Quasi-rigorous method> Calculation of *yaw*, *x*, *z*, and β

Iterative procedure

<Simplified method> Transform point coordinates in Strip B (Equation 3.17)

Quasi-rigorous method> Adjust point coordinates in Strip A&B (Equation 3.29)

Finding closest point-patch pairs using transformed/adjusted coordinates

Parameter estimation using bias-contaminated coordinates

<Simplified method> Sifts and rotation estimation $\{X_T, Y_T, Z_T, \varphi\}$ (Equation 3.17)

<Quasi-rigorous method> Calibration parameter estimation $\{\delta\Delta X, \delta\Delta Y, \delta\Delta\omega, \delta\Delta\phi, \delta\Delta\kappa, \delta S, \delta\rho\}$ (Equations 3.27 and 3.28)

N — Max-change in estimation < pre-defined threshold — Y

<Simplified method> Calibration parameter estimation $\{\delta\Delta X, \delta\Delta Y, \delta\Delta\omega, \delta\Delta\phi, \delta\Delta\kappa, \delta S, \delta\rho\}$ from $\{X_T, Y_T, Z_T, \varphi\}$ Equations 3.18, 3.19, and 3.20

Common procedure

Simplified method

Quasi-rigorous method

Adjusted point cloud using determined biases

<Simplified method> (Equation 3.21)

<Quasi-rigorous method> (Equation 3.29)

End

Figure 4.7. The workflow of the proposed calibration methods (the simplified and quasi-rigorous) using the ICPatch procedure.

CHAPTER 5

EXPERIMENTAL RESULTS

5.1 Introduction

This chapter aims at testing the validity of the proposed simplified and quasi-rigorous calibration methods using simulated and real datasets. The main purpose of utilizing simulated data is to verify the performance of the proposed models, including the point cloud adjustment formulas, in a controlled environment as well as studying the impact of deviations from the listed assumptions in the previous section on the estimated parameters. In addition to the simulated data test, the validity of the proposed methods is tested using real datasets which were captured by Optech ALTM 2050 and Leica ALS50. The performance of the proposed methods is evaluated with respect to relative and absolute accuracy. The relative accuracy is evaluated by two approaches: qualitative test is carried out using the strip profile and intensity image comparison before/after the calibration, while the quantitative test evaluates how the discrepancies between overlapping strips are improved after adjusting the biased coordinates. The absolute accuracy is evaluated using photogrammetric data. The results of the photogrammetric bundle adjustment using the LiDAR strips as control data will be evaluated using check points before/after the calibration. The evaluation of the check point errors presents the absolute accuracy of LiDAR data before/after the calibration.

5.2   Simulation Data Experiment

In this section, feasibility tests for the simplified and quasi-rigorous calibration methods will be presented using simulated datasets. The main purpose of utilizing simulated datasets for the experiments is to verify the performance of the proposed methods in a controlled environment as well as studying the impact of deviations from the listed assumptions for deriving the proposed methods. The following is the summary of the assumptions used in Chapter 3.

For the simplified method:

(i) linear scanning systems are considered, (ii) variations in the object space elevations are much smaller than the flight altitude, (iii) the flight lines are parallel, (iv) the platform trajectory is straight, (v) we are dealing with an almost levelled scanner, and (vi) the boresight angles are assumed to be very small.

For the quasi-rigorous method:

i) we are dealing with a linear scanner, ii) we are dealing with an almost levelled scanner, and iii) boresight angles are small.

The simulated data consists of 6 strips. Strips 1, 2, 3 and 4 were simulated with 70 kHz Pulse Repetition Frequency (PRF), 50 Hz scan rate, and 1,000m flight altitude. Strips 5 and 6, on the other hand, were simulated with 50 kHz PRF, 40 Hz scan rate, and 2,000m flight altitude. Strips 1 and 2 as well as strips 5 and 6 were flown in opposite directions with 100% overlap ratio while strips 3 and 4 were flown in the same direction with 50% overlap ratio. The encoder angles ranged between -25° and 25° for all the simulated strips. The simulated surface had terrain as well as some buildings with an elevation range

between 20.0 and 132.5 m. The range of the terrain slope was between 0° and 6.5° while the building rooftops had slopes up to 45°.

To test the impact of deviations from parallelism and vertical scanning, four cases were considered. In cases 1, 2 and 3, the strips were captured with a levelled laser unit (i.e., zero pitch and roll angles). The overlapping strips in case 1 were parallel to each other, while the overlapping strips in cases 2 and 3 were flown in non-parallel directions with 10° and 30° deviation from parallelism. In case 4, the strips were flown in non-parallel directions with 10° deviation from parallelism and un-levelled laser scanning with roll angles between -5° and 5° for all the strips, 5° pitch angle for strips 1, 3, 4, and 5, and -5° pitch angle for strips 2 and 6. The simulated surface and flight lines are shown in Figure 5.1. The above mentioned characteristics of the simulated strips are summarized in Table 5.1. Using the simulated surface, flight trajectories, and system parameters, the LiDAR measurements were derived. Then, biases were introduced to the system parameters as well as noise to the system measurements. The biased system parameters and noisy measurements were used to derive the distorted LiDAR point cloud coordinates. The characteristics of the introduced noise and biases in the system measurements and parameters are summarized in Table 5.2.

(a)

Profile of the simulated terrain

Top view of the simulated terrain

(b)
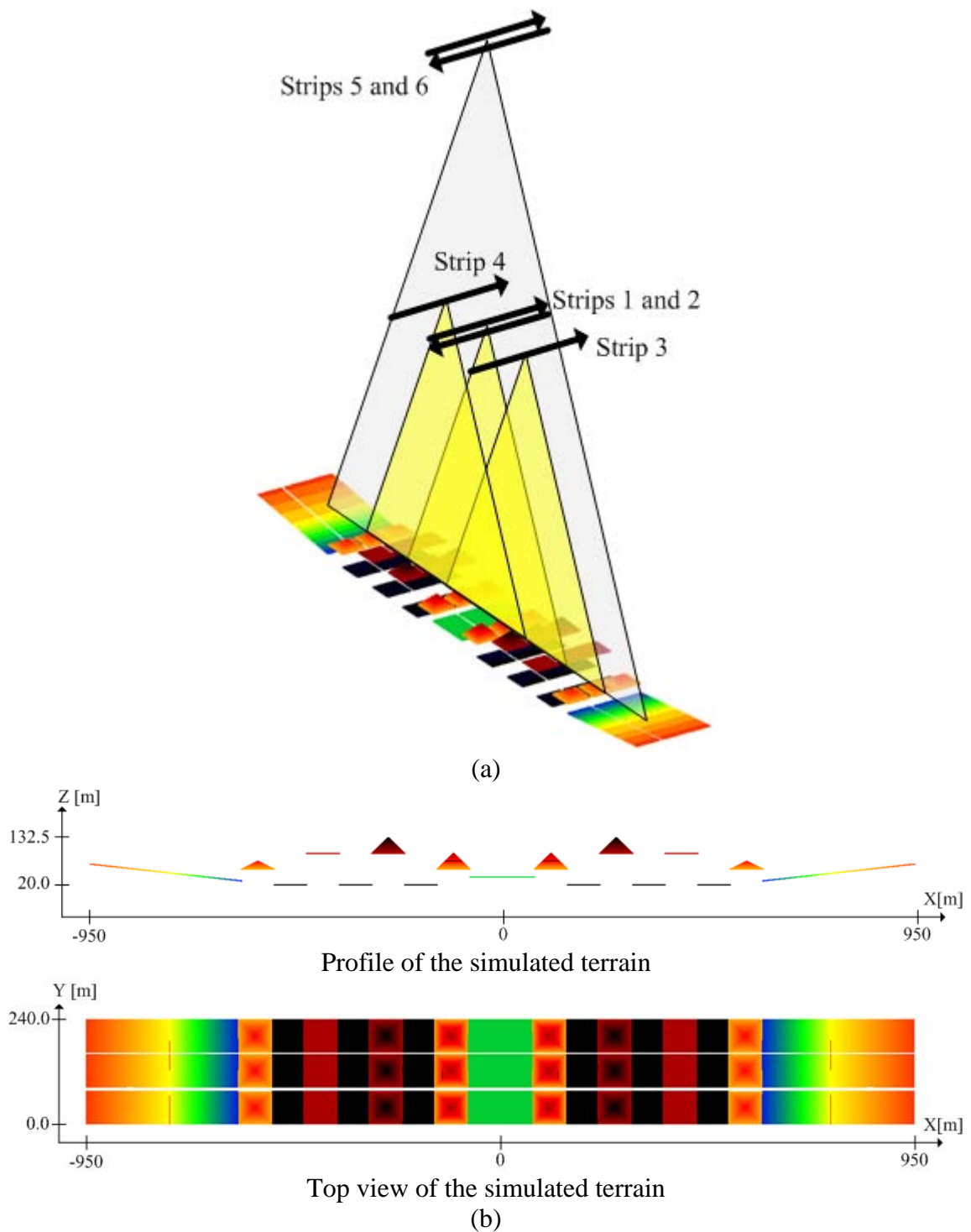
Figure 5.1. (a) simulated terrain and 6 flight lines which consist of 3 overlapping pairs (1&2, 3&4, and 5&6); (b) profile (across the flight line) and top view of the simulated terrain.

Table 5.1. Flight configuration and characteristics of the simulated LiDAR data.

Strip #	Flying direction (heading) [°]				Roll [°]		Pitch [°]		Flight Altitude [m]
	Case #				Case #		Case #		
	1	2	3	4	1, 2, & 3	4	1, 2, & 3	4	
1	0	5	15	5	0	-5 to 5	0	5	1000
2	180	175	165	175	0	-5 to 5	0	-5	1000
3	0	5	15	5	0	-5 to 5	0	5	1000
4	0	-5	-15	-5	0	-5 to 5	0	5	1000
5	0	5	15	5	0	-5 to 5	0	5	2000
6	180	175	165	175	0	-5 to 5	0	-5	2000

Table 5.2. Random and systematic errors introduced in the simulated LiDAR data.

Items	Values
Random errors in position data ($X/Y/Z$)	±0.1m/±0.1m/±0.15m
Random errors in attitude data (*roll/pitch/yaw*)	±0.01°/±0.01°/±0.016°
Random errors in encoder angles	±0.009°
Random errors in laser ranges	±2cm
Biases in lever-arm offset ($\delta\Delta X$, $\delta\Delta Y$, $\delta\Delta Z$)	5cm/5cm/5cm
Biases in boresight angles ($\delta\Delta\omega$, $\delta\Delta\varphi$, $\delta\Delta\kappa$)	0.01°/0.01°/0.01°
Bias in encoder angle scale factor (δS)	0.001
Bias in laser ranges ($\delta\Delta\rho$)	50cm

5.2.1 Comparison of the Modified Weight Matrix and Volume Constraint

As previously discussed in Chapter 4, there are two approaches available in the proposed methods with respect to the similarity measure: volume (determinant) constraint and modified weight matrix. In this section, the two approaches will be compared using the

simulated dataset cases 1 and 4. The comparison will be conducted by checking the difference between the estimated parameters through the volume constraint and modified weight matrix. One should note that this section mainly focuses on the comparison of the experimental results of cases 1 and 4 with respect to the different approaches of the similarity measure. Further analysis about the experimental results including all simulated dataset will be discussed after this section with respect to the quality of the estimated systematic biases.

Tables 5.3 and 5.4 show the estimated transformation parameters (for the simplified method) and systematic biases (for the quasi-rigorous method), respectively. The results are estimated using both approaches (the modified weight matrix and volume constraint) for the three overlapping pairs in cases 1 and 4. As we can see, there is no significant difference between the estimated transformation parameters and systematic biases for both approaches. From these results, one can conclude that, as long as the same matching strategy (closest point and triangular patch) is utilized, there is no significant change in the results of the simplified and quasi-rigorous methods regardless of which similarity measure is used. In this study, the modified weight matrix approach is preferred because there is no significant difference between the results derived by both approaches and the volume (determinant) constraint is difficult to be implemented compared to the use of the modified weight matrix. The combination of transformation and determinant functions increases the complexity of the mathematical model and leads to nonlinear problem. On the other hand, the modified weight matrix approach can be practically implemented without the need for an additional mathematical model and the performance is relatively rapid compared to the volume constraints because of the less computational loads. One

can further argue that the modified weight matrix can be used not only for point-path correspondences but also point-line correspondences after modifying the weight matrix based on the line orientation.

Table 5.3. Comparison of the estimated transformation parameters using the modified weight matrix and volume (determinant) constraint using cases 1 and 4.

Overlapping pair	X_T (m)	Y_T (m)	Z_T (m)	φ (°)
Modified weight matrix (Case 1)				
Strips (1 & 2)	-0.248	0.419	-0.001	0.0198
Strips (4 & 3)	-0.761	-0.109	0.080	0.0642
Strips (5 & 6)	-0.599	0.777	0.001	0.0199
Volume (determinant) constraint (Case 1)				
Strips (1 & 2)	-0.247	0.419	-0.001	0.0198
Strips (4 & 3)	-0.763	-0.098	0.080	0.0643
Strips (5 & 6)	-0.599	0.775	0.001	0.0199
Modified weight matrix (Case 4)				
Strips (1 & 2)	-0.248	0.484	-0.002	0.0181
Strips (4 & 3)	-0.805	-0.095	0.079	0.0611
Strips (5 & 6)	-0.625	0.806	0.009	0.0170
Volume (determinant) constraint (Case 4)				
Strips (1 & 2)	-0.248	0.484	-0.002	0.0181
Strips (4 & 3)	-0.806	-0.096	0.079	0.0613
Strips (5 & 6)	-0.626	0.805	0.009	0.0170

Table 5.4. Comparison of the quasi-rigorous method results through the modified weight matrix and volume (determinant) constraint for cases 1 and 4.

$\delta\Delta X$(m)	$\delta\Delta Y$(m)	$\delta\Delta\omega$(°)	$\delta\Delta\varphi$(°)	$\delta\Delta\kappa$(°)	$\delta\Delta\rho$ (m)	δS
		Modified weight matrix (Case 1)				
0.048	0.046	0.0102	0.0099	0.0101	0.471	0.0010
		Volume constraint (Case 1)				
0.049	0.047	0.0102	0.0099	0.0100	0.470	0.0010
		Modified weight matrix (Case 4)				
0.032	0.093	0.0093	0.0097	0.0102	0.524	0.0010
		Volume constraint (Case 4)				
0.027	0.088	0.0095	0.0096	0.0103	0.466	0.0011

In summary, the ultimate target function of the modified weight matrix is to minimize the normal distance between corresponding point and planar patch; therefore, the strength of the modified weight matrix is that the normal distance constraint can be manipulated without the use of an explicit function of the co-planarity constraint such as the volume constraint. Due to the compatible estimation results from both approaches (the volume constraint and modified weight matrix) and the strength of the modified weight matrix, after this section, the experimental results using simulated and real datasets will present the transformation parameters and systematic biases estimated by the use of the modified weight matrix.

5.2.2 The Simplified Method Results

As discussed in section 3.2, the Simplified method consists of a two-step procedure. First, the discrepancies between overlapping strips are determined; then, the system biases are estimated based on the determined discrepancies between the strips. Using the ICPatch

procedure, the biased and noise-contaminated footprints have been used to check for systematic biases between the overlapping strips. The overlapping strip configuration previously mentioned was chosen since it allows for the maximization of the impact of systematic biases as well as the ability to decouple the different biases from each other. Table 5.5 shows the estimated transformation parameters and a-posteriori variance factors of the adjustment procedures for the three overlapping strip pairs in case 1.

Table 5.5. Estimated transformation parameters for the simplified method in case 1 (parallel overlapping strip pairs).

Case 1	Strips (1 & 2)	Strips (4 & 3)	Strips (5 & 6)
X_T (m)	-0.248	-0.761	-0.599
Y_T (m)	0.419	-0.109	0.777
Z_T (m)	-0.001	0.080	0.001
φ (°)	0.0198	0.0642	0.0199
$\hat{\sigma}^2$	0.135	0.122	0.164

The first conclusion that can be drawn from the reported values is that there are biases in the system parameters and measurements. In the absence of biases, the estimated parameters should be almost zeros regardless of the random noise level in the input point cloud. The estimated transformation parameters are then expressed as a linear combination of the biases in the LiDAR system using Equation 3.19 (for the strips flown in opposite directions with 100% overlap ratio) and Equation 3.20 (for the strips flown in same directions). Finally, a least-squares adjustment derives an estimate of the biases in the LiDAR system parameters as shown in Table 5.6. In this table, the standard deviations show that the estimated biases are reliable. One should note that the bias in the lever-arm offset along the Z axis is not determined in the procedure since it does not

cause any discrepancy between overlapping strips regardless of the flight direction (refer to section 3.2).

Table 5.6. Estimated biases from the transformation parameters in Table 5.5.

Case #	$\delta\Delta X \pm \sigma$ (m)	$\delta\Delta Y \pm \sigma$ (m)	$\delta\Delta\omega \pm \sigma$ (°)	$\delta\Delta\varphi \pm \sigma$ (°)	$\delta\Delta\kappa \pm \sigma$ (°)	$\delta\Delta\rho \pm \sigma$ (m)	$\delta S \pm \sigma$
Case 1	0.039	0.041	0.0102	0.0099	0.0133	0.467	0.0012
	$\pm\,0.0012$	$\pm\,0.0032$	$\pm\,0.0001$	$\pm\,0.0000$	$\pm\,0.0004$	$\pm\,0.0062$	$\pm\,0.0000$

The involved strips in the above experiments are based on optimal datasets, which comply with the listed assumptions (refer to section 3.2) except for having a flat object space. To investigate the impact of having non-parallel overlapping strip pairs, this research conducted the other three experiments where there are 10° (cases 2 and 4) or 30° (case 3) deviation from parallelism between overlapping strips. In addition, the condition of an un-levelled scanner is applied to case 4 where the simulated strips are captured with ±5° roll and pitch angles. The flight parameters for the non-parallel/un-levelled cases are previously shown in Table 5.1. Tables 5.7, 5.8, and 5.9 show the estimated transformation parameters for the strips in case 2, 3 and 4, respectively.

Table 5.7. Estimated transformation parameters for the simplified method in case 2 (10° deviation from parallelism).

Case 2	Strips (1 & 2)	Strips (4 & 3)	Strips (5 & 6)
X_T (m)	-0.250	-0.789	-0.606
Y_T (m)	0.415	-0.103	0.756
Z_T (m)	-0.000	0.080	0.000
φ (°)	0.0199	0.0629	0.0200
$\hat{\sigma}^2$	0.136	0.147	0.167

Table 5.8. Estimated transformation parameters for the simplified method in case 3 (30° deviation from parallelism).

Case 3	Strips (1 & 2)	Strips (4 & 3)	Strips (5 & 6)
X_T (m)	-0.240	-0.827	-0.582
Y_T (m)	0.403	-0.145	0.734
Z_T (m)	-0.001	0.078	0.002
φ (°)	0.0193	0.0596	0.0193
$\hat{\sigma}^2$	0.144	0.140	0.172

Table 5.9. Estimated transformation parameters for the simplified method in case 4 (10° deviation from parallelism and 5° deviation from level).

Case 4	Strips (1 & 2)	Strips (4 & 3)	Strips (5 & 6)
X_T (m)	-0.248	-0.805	-0.625
Y_T (m)	0.484	-0.095	0.806
Z_T (m)	-0.002	0.079	0.009
φ (°)	0.0181	0.0611	0.0170
$\hat{\sigma}^2$	0.159	0.147	0.217

The estimated biases in the system parameters, which correspond to these transformation parameters, are reported in Table 5.10. As it can be seen in Tables 5.7, 5.8, and 5.9, the a-posteriori variance factors of the estimation results (derived from the ICPatch procedure) are slightly worse as the parallelism deviation is increased. In Table 5.10, one can see that the bias in the boresight heading angle is mainly affected by the non-parallelism of the involved strips. In addition, the result of case 4 (un-levelled laser scanner) shows that the estimated biases in the lever-arm offsets and boresight pitch($\Delta\omega$)/roll($\Delta\varphi$) angles are worse than the estimated values in case 2 and 3, where the reliability of the estimated biases can be confirmed by their standard deviations reported in Table 5.10. From the

results in Table 5.10, one can conclude that 10° deviation from parallelism of overlapping strips can be handled by the simplified method; 30° deviation from parallelism mainly affect to the estimation of the range bias. In addition, 5° deviation from level of platform attitudes (roll and pitch) makes worse the estimation of the biases in the lever-arm offsets ($\delta\Delta X$ and $\delta\Delta Y$) and boresight angles ($\delta\Delta\omega$ and $\delta\Delta\varphi$) as well as the range bias.

Table 5.10. Estimated biases from the transformation parameters in Tables 5.7 – 5.9

Case #	$\delta\Delta X \pm \sigma$ (m)	$\delta\Delta Y \pm \sigma$ (m)	$\delta\Delta\omega \pm \sigma$ (°)	$\delta\Delta\varphi \pm \sigma$ (°)	$\delta\Delta\kappa \pm \sigma$ (°)	$\delta\Delta\rho \pm \sigma$ (m)	$\delta S \pm \sigma$
Case 2	0.039 ± 0.0011	0.040 ± 0.0032	0.0102 ± 0.0001	0.0099 ± 0.0000	0.0134 ± 0.0004	0.466 ± 0.0061	0.0012 ± 0.0000
Case 3	0.039 ± 0.0008	0.045 ± 0.0024	0.0095 ± 0.0001	0.0097 ± 0.0000	0.0178 ± 0.0003	0.678 ± 0.0045	0.0011 ± 0.0000
Case 4	0.005 ± 0.0151	0.090 ± 0.0428	0.0091 ± 0.0016	0.0088 ± 0.0002	0.0117 ± 0.0049	0.607 ± 0.0117	0.0012 ± 0.0000

5.2.3 The Quasi-rigorous Method Results

The second calibration method is the quasi-rigorous method which utilizes trajectory position data and time tagged point clouds. The feasibility of the quasi-rigorous calibration method will be investigated using the same data introduced in the previous section. The required trajectory position data and time tags for each laser point were produced during the LiDAR strip simulation procedure. In this research, trajectory points within 2 seconds are chosen to estimate the flight direction because, at 180km/hr speed, 2 second would define a 100m local trajectory which is sufficient for reliable estimation of the heading angle. However, it should be mentioned that one can reasonably choose the time search range based on the condition of flight mission and available trajectory data.

Table 5.11 shows the estimated biases in the system parameters using the quasi-rigorous method. All the estimated biases are very close to the introduced biases, and the standard

deviations of the estimated values are compatible in all cases. Especially, the results of non-parallel strips in cases 2 and 3 and non-parallel/un-levelled strips in case 4 are significantly improved compared to Tables 5.10. For example, the estimation of the boresight heading angle is mainly affected by the non-parallelism in the simplified method; however, one can confirm that the improvement of the estimation of the bias in the quasi-rigorous results. The range bias estimated by the quasi-rigorous method is relatively close to the true value compared to the values estimated by the simplified method. From these results, one can conclude that the quasi-rigorous method provides reasonable estimates regardless the magnitudes of the deviations of terrain elevation and parallelism of overlapping strips. It shows that the use of trajectory position data and time-tagged point cloud effectively handle the non-parallel overlapping strip pairs to estimate the biases, which is the strength of the quasi-rigorous method compared to the simplified method. The result of case 4 is compatible with the result of case 2, and one can conclude that strips captured with 5° deviation from level can be handled by the quasi-rigorous method. The next section will show the validity of the proposed methods by evaluating the compatibility of the adjusted coordinates using the estimated biases.

Table 5.11. Estimated biases using the quasi-rigorous method for the simulated datasets.

Case #	$\delta\Delta X \pm \sigma$ (m)	$\delta\Delta Y \pm \sigma$ (m)	$\delta\Delta\omega \pm \sigma$ (°)	$\delta\Delta\varphi \pm \sigma$ (°)	$\delta\Delta\kappa \pm \sigma$ (°)	$\delta\Delta\rho \pm \sigma$ (m)	$\delta S \pm \sigma$
Case 1	0.048 ± 0.0007	0.046 ± 0.0012	0.0102 ± 0.0000	0.0099 ± 0.0000	0.0101 ± 0.0002	0.471 ± 0.0074	0.0010 ± 0.0000
Case 2	0.048 ± 0.0007	0.055 ± 0.0013	0.0097 ± 0.0000	0.0100 ± 0.0000	0.0100 ± 0.0002	0.497 ± 0.0073	0.0010 ± 0.0000
Case 3	0.093 ± 0.0009	0.092 ± 0.0016	0.0088 ± 0.0000	0.0102 ± 0.0000	0.0141 ± 0.0002	0.453 ± 0.0079	0.0008 ± 0.0000
Case 4	0.032 ± 0.0007	0.093 ± 0.0010	0.0093 ± 0.0000	0.0097 ± 0.0000	0.0102 ± 0.0002	0.524 ± 0.0059	0.0010 ± 0.0000

5.2.4   Quality of Adjusted Point Cloud Coordinates

In this section, the proposed point cloud adjustment procedures will be verified based on the mean/RMSE (Root Mean Squared Error) analysis before/after the calibration. First, the impact of the random and systematic errors introduced to the simulated strips will be discussed using mean/RMSE analysis between true and distorted coordinates. Then, the proposed point cloud adjustment procedures will be verified by the comparison between the true and adjusted point clouds using the true biases in Tables 5.6, 5.10 and 5.11. After discussing the efficiency of the point cloud adjustment formula, another mean/RMSE analysis will be conducted for the true and adjusted point clouds using the biases estimated by the simplified and quasi-rigorous methods to evaluate the performance of the point cloud adjustment procedures. The mean/RMSE analysis is conducted for strips 3 and 6 in all four cases. These two strips are good enough to see the validity of the proposed point correction procedure because the two strips have different flying heights (1,000 and 2,000m) and directions (north to south and south to north).

Table 5.12 shows the mean/RMSE analysis between the true and noise-contaminated point clouds. In this table, all mean values are close to zero because there is no systematic error. The RMSE values for strips 6 are larger than the values for strip 3 for all the cases, which means that the impact of the random errors in the platform attitudes and encoder angles depends on the flight altitude. In addition, the RMSE values along the *XY* plane are more significant than the RMSE values along the vertical direction, which shows that the impact of the noise mainly affect to the planimetric accuracy rather than the vertical accuracy.

Table 5.12. Mean/RMSE analysis between true and noise-contaminated coordinates.

	Mean			RMSE		
	X (m)	Y (m)	Z (m)	X (m)	Y (m)	Z (m)
			Case 1			
Strip3 (1,000m)	0.001	0.000	-0.000	0.246	0.206	0.163
Strip6 (2,000m)	-0.000	0.002	0.000	0.468	0.383	0.194
			Case 2			
Strip3 (1,000m)	0.000	-0.000	-0.000	0.246	0.205	0.163
Strip6 (2,000m)	0.000	-0.000	0.000	0.468	0.403	0.215
			Case 3			
Strip3 (1,000m)	-0.000	0.004	0.001	0.245	0.222	0.174
Strip6 (2,000m)	0.000	0.008	-0.001	0.471	0.424	0.242
			Case 4			
Strip3 (1,000m)	0.001	0.001	-0.000	0.245	0.206	0.161
Strip6 (2,000m)	-0.002	0.001	-0.000	0.471	0.379	0.192

Table 5.13 shows the mean/RMSE analysis between true and noise/bias-contaminated point cloud. In this table, the mean values are non-zero values, which mean that the point cloud coordinates are systematically biased. In addition, the RMSE values in this table worse than the values reported in Table 5.12 due to the impact of the biases in the system parameters. In the comparison between strips 3 and 6, the RMSE values along the vertical direction are compatible, while there are significant differences between the RMSE values of strips 3 and 6 along the *XY* plane. It can be explained by the fact that the impact of the biases in the system parameters on the height errors is not affected by the flight altitude, while the impact on the planimetric errors is significantly affected by the flight altitude.

Table 5.13. Mean/RMSE analysis between true and noise/bias-contaminated coordinates.

	Mean			RMSE		
	X (m)	Y (m)	Z (m)	X (m)	Y (m)	Z (m)
Case 1						
Strip3 (1,000m)	-0.065	0.216	-0.370	0.456	0.301	0.413
Strip6 (2,000m)	-0.289	0.391	-0.303	0.828	0.555	0.393
Case 2						
Strip3 (1,000m)	-0.065	0.220	-0.378	0.436	0.310	0.418
Strip6 (2,000m)	0.224	-0.414	-0.303	0.820	0.566	0.394
Case 3						
Strip3 (1,000m)	-0.071	0.217	-0.389	0.403	0.326	0.426
Strip6 (2,000m)	0.275	-0.438	-0.305	0.833	0.587	0.407
Case 4						
Strip3 (1,000m)	-0.129	0.238	-0.359	0.447	0.323	0.401
Strip6 (2,000m)	0.287	-0.419	-0.281	0.812	0.574	0.371

Another mean/RMSE analysis is conducted to justify the proposed point cloud adjustment procedures. Table 5.14 shows the mean/RMSE analysis between true and adjusted point clouds by the simplified method (Equation 3.21) and true biases, while Table 5.15 shows the comparison between the true and adjusted point clouds by the quasi-rigorous method (Equation 3.29) and true biases. These tables show that the mean values along the *XY* plane are close to zero. On the other hand, the mean values along the vertical direction are close to 5cm, which can be explained by the impact of the bias ($\delta\Delta Z$) in the lever-arm offset along the vertical direction. The RMSE values in this table are significantly improved compared to the RMSE values reported in Table 5.13, and quite compatible with the RMSE values in Table 5.12, which means that the impact of the systematic biases is successfully eliminated. From these results, the point cloud adjustment procedures for both the simplified and quasi-rigorous methods are justified. In addition, one can find that the mean/RMSE values are quite compatible between the

simplified and quasi-rigorous methods regardless the deviation from the parallelism, which means that if the estimated biases from both methods are compatible, the quality of the point cloud adjustment is not affected by the deviation for the parallelism of overlapping strips. In Equation 3.21, the vertical distance between firing point and a point in question is estimated by nominal flying attitude and point elevation, and the flight direction is determined by a normal direction to a scan-line which is estimated by a line fitting procedure using segmented scan-line points. On the other hand, in Equation 3.29, the vertical distance and flight direction are estimated by the trajectory position data. Therefore, if the estimated flight directions in the simplified method are quite reliable, and there is no significant variation in the flight altitudes, during the data capturing time, the point cloud adjustment results from both the simplified and quasi-rigorous methods can be quite compatible.

Table 5.14. Mean/RMSE analysis between true and adjusted coordinates by the simplified method formula (Equation 3.21) and true biases in Table 5.2.

	Mean			RMSE		
	X (m)	Y (m)	Z (m)	X (m)	Y (m)	Z (m)
Case 1						
Strip3 (1,000m)	0.003	0.003	0.050	0.244	0.206	0.170
Strip6 (2,000m)	0.002	0.001	0.050	0.468	0.383	0.200
Case 2						
Strip3 (1,000m)	0.000	0.001	0.050	0.244	0.206	0.170
Strip6 (2,000m)	0.001	0.000	0.050	0.466	0.384	0.200
Case 3						
Strip3 (1,000m)	0.000	-0.000	0.050	0.241	0.209	0.169
Strip6 (2,000m)	-0.001	0.002	0.050	0.463	0.385	0.196
Case 4						
Strip3 (1,000m)	-0.012	0.029	0.068	0.253	0.209	0.177
Strip6 (2,000m)	0.017	-0.026	0.083	0.485	0.382	0.213

Table 5.15. Mean/RMSE analysis between the true and adjusted coordinates by the quasi-rigorous method formula (Equation 3.29) and true biases in Table 5.2.

	Mean			RMSE		
	X (m)	Y (m)	Z (m)	X (m)	Y (m)	Z (m)
Case 1						
Strip3 (1,000m)	0.000	-0.000	0.050	0.244	0.206	0.170
Strip6 (2,000m)	0.002	0.001	0.050	0.468	0.383	0.193
Case 2						
Strip3 (1,000m)	0.001	0.000	0.051	0.244	0.206	0.170
Strip6 (2,000m)	0.008	0.004	0.050	0.466	0.384	0.200
Case 3						
Strip3 (1,000m)	0.000	-0.000	0.050	0.241	0.208	0.169
Strip6 (2,000m)	-0.001	0.002	0.050	0.463	0.385	0.196
Case 4						
Strip3 (1,000m)	-0.012	0.029	0.068	0.253	0.209	0.177
Strip6 (2,000m)	0.013	-0.006	-0.078	0.487	0.385	0.212

After justifying the point cloud adjustment procedures, this research evaluates the performance of the proposed calibration methods in terms of the quality of the adjusted point cloud coordinates. Tables 5.16 and 5.17 present the mean/RMSE analysis between the true and adjusted point clouds by the estimated biases in the system parameters. Table 5.16 shows the mean/RMSE analysis for the simplified method, while Table 5.17 shows the mean/RMSE analysis for the quasi-rigorous method. Comparing Tables 5.13, 5.16 and 5.17, one can see the improvement in the point cloud coordinates, which is manifested in smaller mean and RMSE values. In Table 5.16, the mean values along the *XY* plane are less than 2cm and the RMSE values along the *XY* plane are about 15 and 30cm for strips 3 and 6, respectively. It shows that the systematic errors along the *XY* plane are significantly reduced after the calibration regardless the flight altitude. The RMSE values along the *XY* plane shows the impact of the noise in system measurements,

which is affected by the flight altitude. The mean values along the vertical direction in cases 3 and 4 are worse than the values reported in cases 1 and 2, which is caused by the inferior estimation of the biases from the non-parallel (30° deviation from parallelism; case 3) and un-levelled (5° deviation from level; case 4) overlapping strip. Especially, the estimated range bias in cases 3 and 4 is worse than the other estimated biases, and the range bias mainly affects the vertical accuracy regardless the flight altitude. In Table 5.16, one can see the relatively worse mean values along the vertical direction in cases 3 and 4.

Table 5.16. Mean/RMSE analysis between true and adjusted coordinates by the simplified method formula (Equation 3.21) and estimated biases in Tables 5.6 and 5.10.

	Mean			RMSE		
	X (m)	Y (m)	Z (m)	X (m)	Y (m)	Z (m)
			Case 1			
Strip3 (1,000m)	0.011	0.006	0.005	0.247	0.207	0.163
Strip6 (2,000m)	-0.011	-0.003	-0.009	0.477	0.384	0.195
			Case 2			
Strip3 (1,000m)	0.006	0.003	0.006	0.247	0.207	0.163
Strip6 (2,000m)	-0.006	-0.001	-0.008	0.475	0.384	0.195
			Case 3			
Strip3 (1,000m)	-0.013	-0.000	0.217	0.247	0.213	0.270
Strip6 (2,000m)	0.010	-0.012	-0.211	0.474	0.387	0.284
			Case 4			
Strip3 (1,000m)	0.011	0.006	0.160	0.264	0.207	0.229
Strip6 (2,000m)	0.017	-0.016	0.162	0.504	0.382	0.257

On the other hand, Table 5.17 shows the mean/RMSE analysis between the true and adjusted point cloud by the quasi-rigorous method. The overall quality of the adjusted coordinates is better than the quality of the point cloud adjusted by the simplified method in Table 5.16. As one can see in Table 5.17, the improvement of the vertical accuracy is quite obvious compared to the results from the simplified method, especially in cases 3

and 4. From the reported mean and RMSE values, one can find the improvement of the adjusted point cloud coordinates; especially, the mean values show that the systematic errors are successfully eliminated after the calibration. The mean values along the vertical direction in cases 3 and 4 are significantly reduced compared to the values reported in Table 5.16. One can find the similar improvement in the RMSE values along the vertical direction in cases 3 and 4, which can be explained by the fact that the range bias estimated by the quasi-rigorous method is closer to the true value than the range bias estimated by the simplified method.

Table 5.17. Mean/RMSE analysis between error-free and adjusted coordinates by the quasi-rigorous method formula (Equation 3.29) and estimated biases in Table 5.11.

	Mean			RMSE		
	X (m)	Y (m)	Z (m)	X (m)	Y (m)	Z (m)
Case 1						
Strip3 (1,000m)	0.000	0.001	0.022	0.244	0.206	0.164
Strip6 (2,000m)	-0.001	0.002	0.022	0.468	0.383	0.195
Case 2						
Strip3 (1,000m)	0.003	0.001	0.022	0.244	0.206	0.164
Strip6 (2,000m)	0.009	0.007	0.022	0.466	0.384	0.195
Case 3						
Strip3 (1,000m)	-0.015	-0.032	0.017	0.248	0.211	0.163
Strip6 (2,000m)	-0.000	0.005	0.022	0.463	0.385	0.191
Case 4						
Strip3 (1,000m)	0.003	-0.001	0.092	0.253	0.207	0.187
Strip6 (2,000m)	0.007	0.013	0.101	0.487	0.385	0.221

This mean/RMSE analysis can verify the success of Equations 3.21 and 3.29 in removing the systematic distortions from the point cloud coordinates. Thus, one can conclude that the proposed calibration methods can show the performance from systematic biases estimation to point cloud adjustment for non-parallel/non-vertical flight configuration as

well as the terrain elevation deviation in the simulation datasets. In the next section, the feasibility of the proposed methods will be verified using real LiDAR dataset.

5.3 Real Data Experiment I

To evaluate the performance of the proposed calibration methods, we acquired a LiDAR dataset captured by an Optech ALTM 2050 using the optimum flight configuration. The real dataset was captured from a platform moving with 200 km/hr speed, 20° scan angle, 50 kHz PRF, and 20-29 Hz scan frequency. The density of the point cloud is about 1 point/m^2 for strips captured from 1,000m flight altitude, and about 0.5 point/ m^2 for strips captured from 2,000m flight altitude. Figure 5.2 and Table 5.18 illustrate the characteristics of this real dataset. Table 5.19 lists the five overlapping strip pairs that could be utilized. The strip pairs 1&2, 3&4, 3&5, and 2&6 are utilized in the calibration procedure. Strips 7&8, on the other hand, are used to check the performance of the proposed calibration procedures by evaluating the compatibility between conjugate surface elements in this pair using the original and adjusted point cloud coordinates.
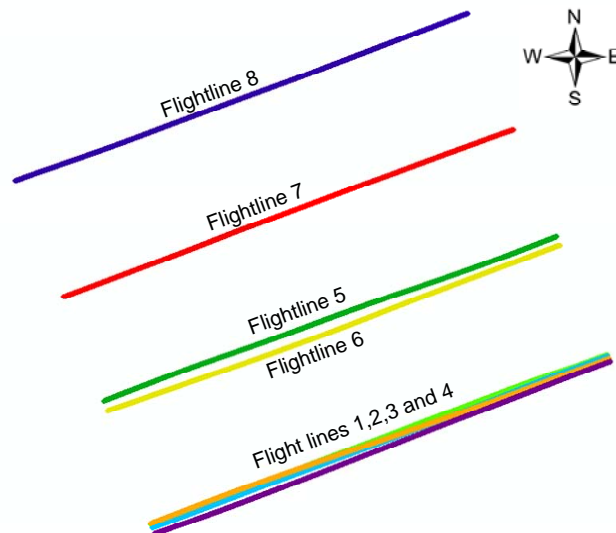
Figure 5.2. Strip configuration of the real dataset captured by Optech ALTM 2050.

Table 5.18. Characteristic of the involved overlapping strip pairs in the proposed calibration procedures.

Strip Number	Flight altitude	Direction
1	2,000 m	SW-NE
2	2,000 m	NE-SW
3	1,000 m	SW-NE
4	1,000 m	NE-SW
5	1,000 m	SW-NE
6	2,000 m	NE-SW
7	1,000 m	NE-SW
8	1,000 m	SW-NE

Table 5.19. Overlapping strip pairs utilized for the calibration procedure and its evaluation.

Overlapping pairs	Overlap ratio	Direction
(i) Strips 1&2	100%	Opposite directions
(ii) Strips 3&4	100%	Opposite directions
(iii) Strips 3&5	50%	Same direction
(iv) Strips 2&6	70%	Same direction
(v) Strips 7&8*	40%	Opposite directions

* Strips 7&8 are used to evaluate the quality of the proposed calibration procedures

It is important to mention that for reliable estimation of the system parameters, the calibration site should have topography with varying slope and aspect and/or an area with plenty of gable roof buildings with varying slope and aspect. Figure 5.3 illustrates strip 3

as an example, where we can observe the presence of gable roof buildings in Figure 5.3c. The procedure of finding the closest point-patch pairs can be carried out using the entire overlap area between neighbouring strips or it can be conducted using an aggregated set of preselected local areas to speed up the process. Regardless of utilizing the whole overlap region or the aggregated set of local areas, the correspondence between conjugate point-patch pairs should be established. Figure 5.4 shows the selected areas in the overlapping region utilized for the estimation of the system biases in the two calibration methods. To test the impact of incorporating control data in the quasi-rigorous method, 900 control points are utilized. The control points are collected over an airport runway (i.e., they are used as vertical control points) using real-time kinematic GPS surveying with a short baseline and a favourable GPS satellite constellation.

(a)

(b)   (c)
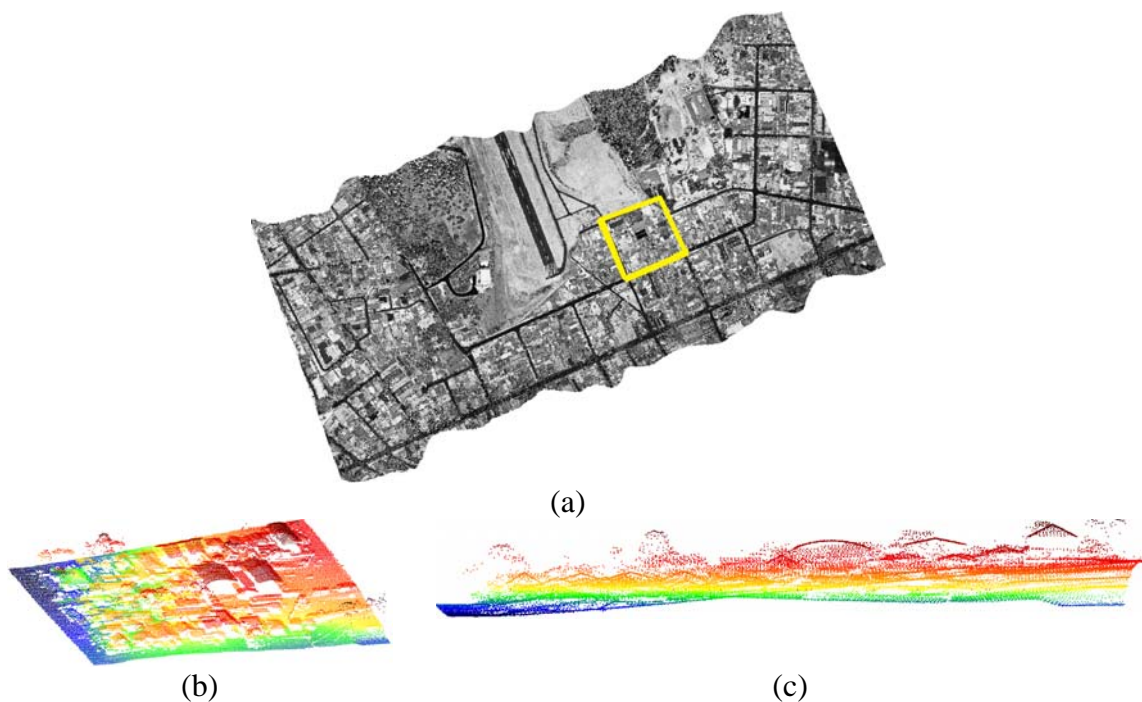
Figure 5.3. Sample data (strip 3): (a) intensity image of the sample strip, (b) 3D view of selected sub-area (yellow box in (a)), and (c) 2D view (X-Z plane) of the sub-area.
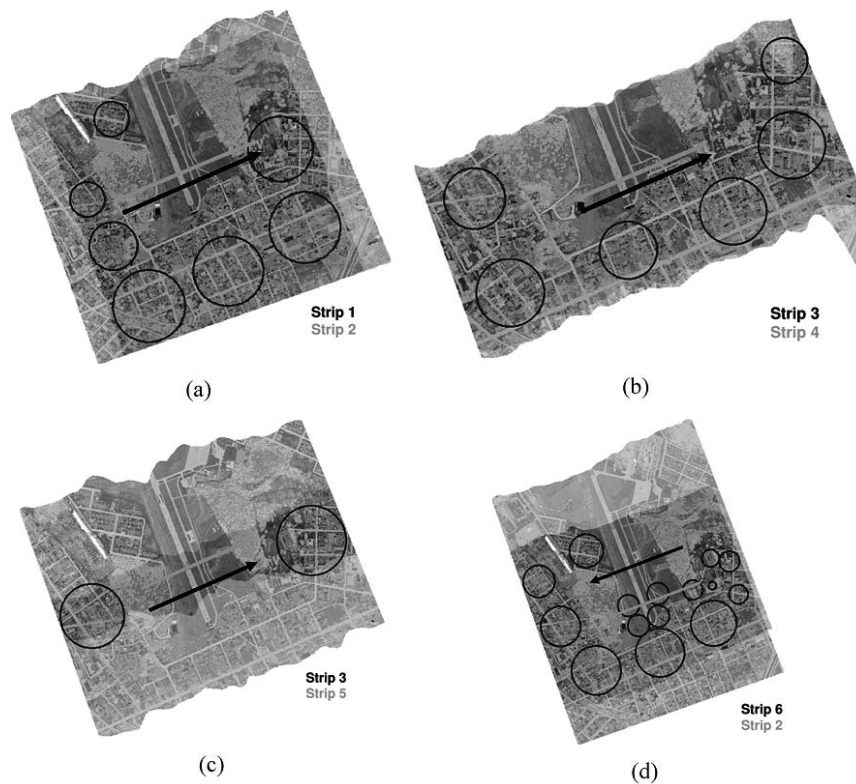
Figure 5.4. Selected areas from the overlapping pairs for the calibration procedure: (a) strips 1&2, (b) strip 3&4, (c) strip 3&5, and d) strip 6&2.

5.3.1   Calibration Results from the Proposed Methods

The derived formulas for the simplified method assume that the flight lines are parallel to the *Y*-axis of the mapping frame. However, the utilized strips are captured from flight lines in the SW-NE and NE-SW directions as can be seen in Table 5.18 and Figure 5.2. Therefore, the estimated transformation parameters have been recalculated to correspond to a local coordinate system where the flight directions are parallel to the *Y*-axis and its origin is located in the centre of the overlap area. The origin of the local coordinate system can be determined by the centroid of overlapping area. If trajectory data is available, *Y*-axis can be determined by the average heading angle. Without the trajectory data, the flight direction can be determined by estimating scan directions. A scan-line

segmentation procedure selects points which are assumed to belong to a scan-line to estimate the scan-line directions. One can assume that the average of the estimated scan directions denotes across the flight direction. The simplified method assumes that the flight directions are parallel to the Y axis of the ground coordinate system. Therefore, the estimated transformation parameters with respect to the ground coordinate system are rotated using the flight direction with respect to the user defined coordinate system. Equations 5.1a, 5.1b, 5.1c, and 5.1d show the procedure to recalculate the transformation parameters using the flight direction. In Equation 5.1a, $\vec{X}_m$ and $\vec{X}_u$ denote LiDAR points defined in the mapping frame and user defined coordinate system, respectively; R_m^u is a rotation matrix defined by the flight direction relating the mapping frame and user defined coordinate system. Equation 5.1b shows a transformation function between strips A and B, where T_m and R_m are shifts and rotation matrix with respect to the mapping frame. The transformation function can be represented by Equation 5.1c using the flight direction with respect to the user defined coordinate system. One can then recalculate T_u and R_u which are the shifts and rotation matrix with respect to the user defined coordinate system (Equation 5.1d).

$$R_m^u \vec{X}_m = \vec{X}_u \tag{5.1a}$$

$$\vec{X}_{mA} = T_m + R_m \vec{X}_{mB} \tag{5.1b}$$

$$\vec{X}_{uA} = R_m^u T_m + R_m^u R_m R_m^{u^T} \vec{X}_{uB} \tag{5.1c}$$

$$T_u = R_m^u T_m \text{ and } R_u = R_m^u R_m R_m^{u^T} \tag{5.1d}$$

Table 5.20 presents the four transformation parameters (X_T, Y_T, Z_T, and φ) among the overlapping strip pairs with respect to the user defined local coordinate system. In this table, one can observe that the estimated Y_T in strips 1&2 and strips 3&4 are significantly larger than the values in strips 3&5 and strips 2&6. Based on their flight directions and altitudes, one can conclude that this is an evidence of a bias in the boresight pitch angle. It can be confirmed by the systematic biases estimated by the simplified method, which are reported in the second row of Table 5.21, where the bias in the boresight pitch angle is much larger than the other angular biases. For the quasi-rigorous method, two experiments are performed. The first experiment utilized only overlapping strips to estimate the biases in system parameters, while the second experiment estimated system biases using overlapping strips and vertical control points. The estimated biases in the system parameters from the simplified method, the quasi-rigorous method without and with control data are summarized in Table 5.21. There is no significant difference between the estimated biases using the quasi-rigorous method with/without the vertical control points except the bias in the range measurement. It shows that the quasi-rigorous method can successfully estimate the biases without the help of control data; however, the difference observed in the estimated range bias can be explained by the correlation between the biases in the range measurement and encoder angle scale factor. Table 5.22 shows the correlation matrices for both results, with/without the control data. As one can see in this table, the use of the vertical control data reduced the correlation between the biases from -0.87 to -0.52. The next section will show the qualitative and quantitative evaluation of the discrepancies between overlapping strips before/after the calibration to confirm the impact of the proposed calibration procedures.

Table 5.20. Estimated transformation parameters derived by the discrepancy detection procedure with respect to the user defined local coordinate system.

	X_T (m)	Y_T (m)	Z_T (m)	φ (°)
Strips 1&2	-0.25	1.27	-0.01	0.00037
Strips 3&4	-0.01	0.52	0.02	-0.00270
Strips 3&5	-0.32	-0.19	-0.06	0.02680
Strips 2&6	-0.42	0.15	0.01	0.02073

Table 5.21. Estimated systematic biases for the simplified method, quasi-rigorous method (without control data), and quasi-rigorous method (with control data).

Methods	$\delta\Delta X$(m)	$\delta\Delta Y$(m)	$\delta\Delta\omega$(")	$\delta\Delta\varphi$(")	$\delta\Delta\kappa$(")	$\delta\Delta\rho$(m)	δS
Simplified	-0.08	-0.11	74.88	-1.08	-39.60	0.22	0.0006
Quasi-rigorous (without control data)	-0.08	-0.12	80.64	-4.68	17.28	0.00	0.0010
Quasi-rigorous (with vertical control data)	-0.08	-0.12	80.64	-5.04	18.72	-0.06	0.0010

Table 5.22. The contribution of the control data to decoupling the correlated parameters.

$\delta\Delta X$(m)	$\delta\Delta Y$(m)	$\delta\Delta\omega$(")	$\delta\Delta\varphi$(")	$\delta\Delta\kappa$(")	$\delta\Delta\rho$(m)	δS
Quasi-rigorous with no control point						
1.00	-0.01	0.01	0.81	0.00	0.09	-0.10
-0.01	1.00	-0.94	-0.01	-0.01	0.00	0.00
0.01	-0.94	1.00	0.01	0.03	0.00	0.00
0.81	-0.01	0.01	1.00	0.00	0.11	-0.13
0.00	-0.01	0.03	0.00	1.00	0.02	-0.01
0.09	0.00	0.00	0.11	0.02	1.00	-0.87
-0.10	0.00	0.00	-0.13	-0.01	-0.87	1.00
Quasi-rigorous with vertical control points						
1.00	-0.01	0.01	0.78	0.000	0.03	-0.05
-0.01	1.00	-0.94	-0.01	-0.006	0.00	0.00
0.01	-0.94	1.00	0.01	0.026	0.00	0.00
0.78	-0.01	0.01	1.00	-0.004	0.03	-0.09
0.00	-0.01	0.03	0.00	1.000	0.01	0.01
0.03	0.00	0.00	0.03	0.011	1.00	-0.52
-0.05	0.00	0.00	-0.09	0.009	-0.52	1.00

5.3.2 Qualitative Evaluation of the Calibration Results

In this section, the improvement of the quality of the data after the calibration is qualitatively evaluated. Visual comparison of the generated intensity images from the original and adjusted point clouds is performed to check any improvements in the clarity and definition of various objects. Besides checking intensity images, profiles are also generated using the original and adjusted point cloud coordinates to check any improvements in the quality of fit between overlapping strips. The improvement in the quality of the generated intensity images is illustrated in Figure 5.5. The intensity images are generated using strips 7 and 8; Figure 5.5a shows the intensity image generated before the calibration procedure, while the other figures in Figure 5.5 show the improved intensity images after the calibration procedure. As it can be seen in this figure (refer to the circled areas), enhancement in the feature definition, such as airplanes and surface markings, is noticeable in the generated intensity images after the calibration procedure. At least in this visual comparison, the quality of the adjusted point clouds is mostly equivalent regardless the used calibration method.

(a)   (b)

<div align="center">(c)   (d)</div>
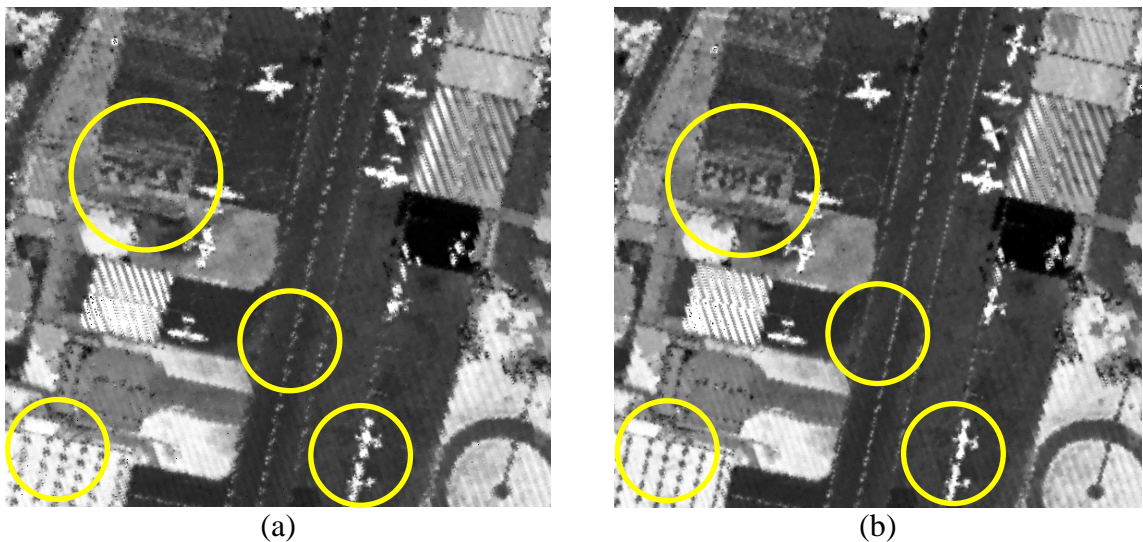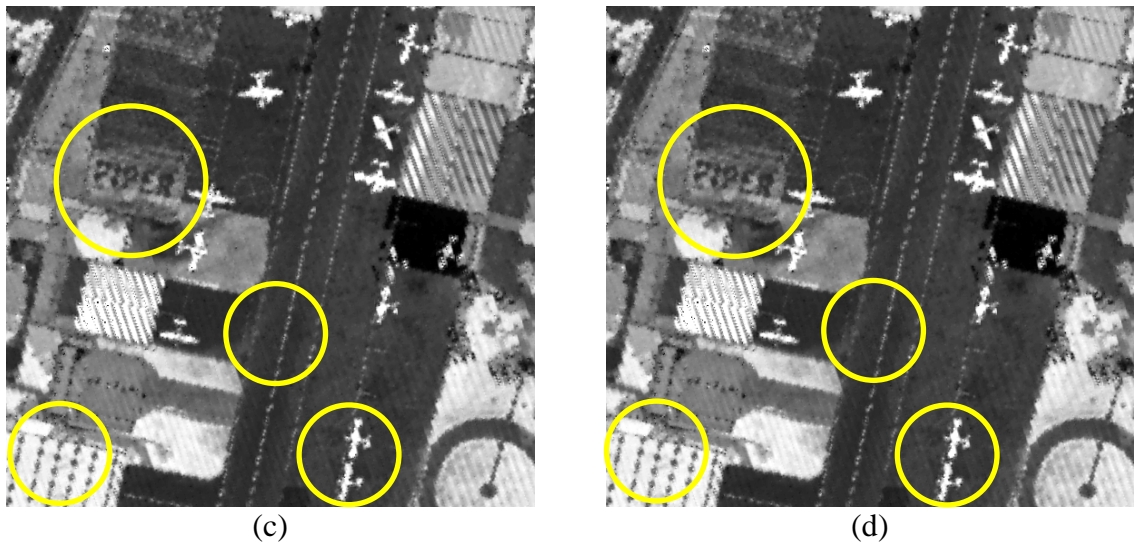
Figure 5.5. Intensity images generated before and after the calibration procedure: (a) original intensity image before the calibration, (b) intensity image after the simplified method, (c) intensity image after the quasi-rigorous method (without control data), and (d) intensity image after the quasi-rigorous method (with control data).

In addition, the profile comparison can show the reduction of the discrepancies between overlapping strips. The selected profile locations are shown in Figure 5.6. The selected four profiles are shown in Figure 5.7. One can observe better compatibility after the calibration procedures, especially the profiles aligned along the flight direction – Y axis, refer to Figure 5.6 for the profiles location. Profile 4 in Figure 5.7 does not present improvements since it is parallel to the scanning direction, where no significant discrepancies were detected (refer to Table 5.20). On the other hand, profiles 2 and 3 are significantly improved because the profiles are along the flight direction and the bias in the boresight pitch angle (see Table 5.21) causes large discrepancies along the flight direction in opposite overlapping strips such as strips 1 and 2.
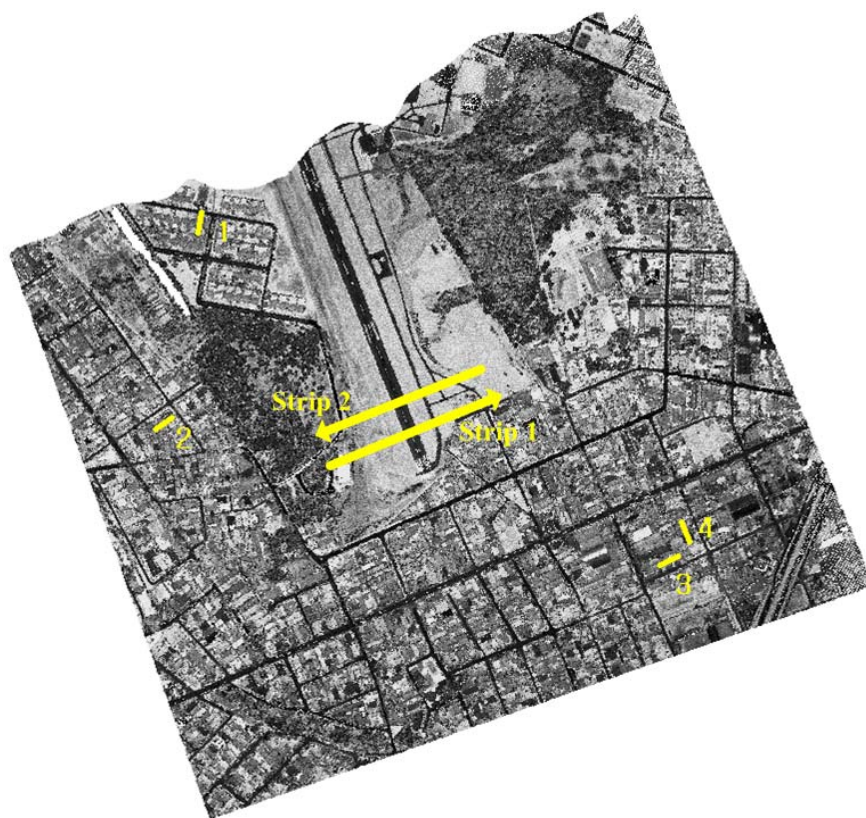
Figure 5.6. Profiles location selected in the overlapping strips 1&2.

Profile #	#1	#2
Before calibration		
After calibration (simplified method)		
After calibration (quasi-rigorous method)		
After calibration (quasi-rigorous method with control)		

120

Profile #	#3	#4
Before calibration		
After calibration (simplified method)		
After calibration (quasi-rigorous method)		
After calibration (quasi-rigorous method with control)		
	● strip 1	● strip 2
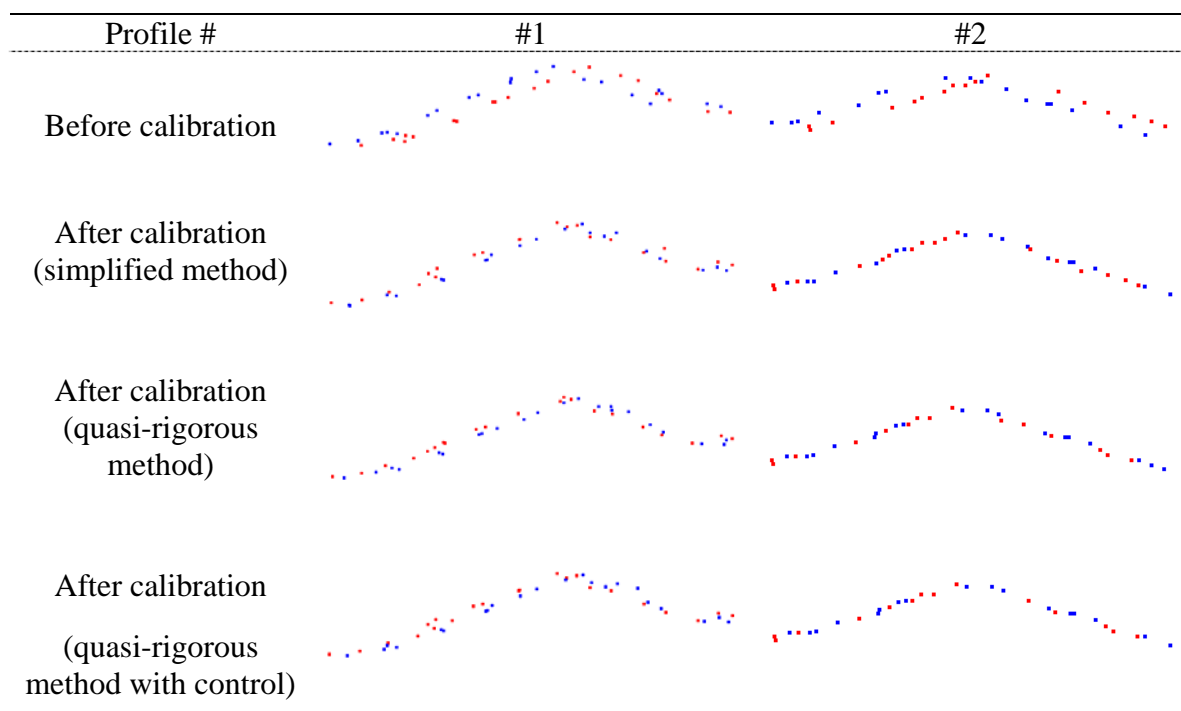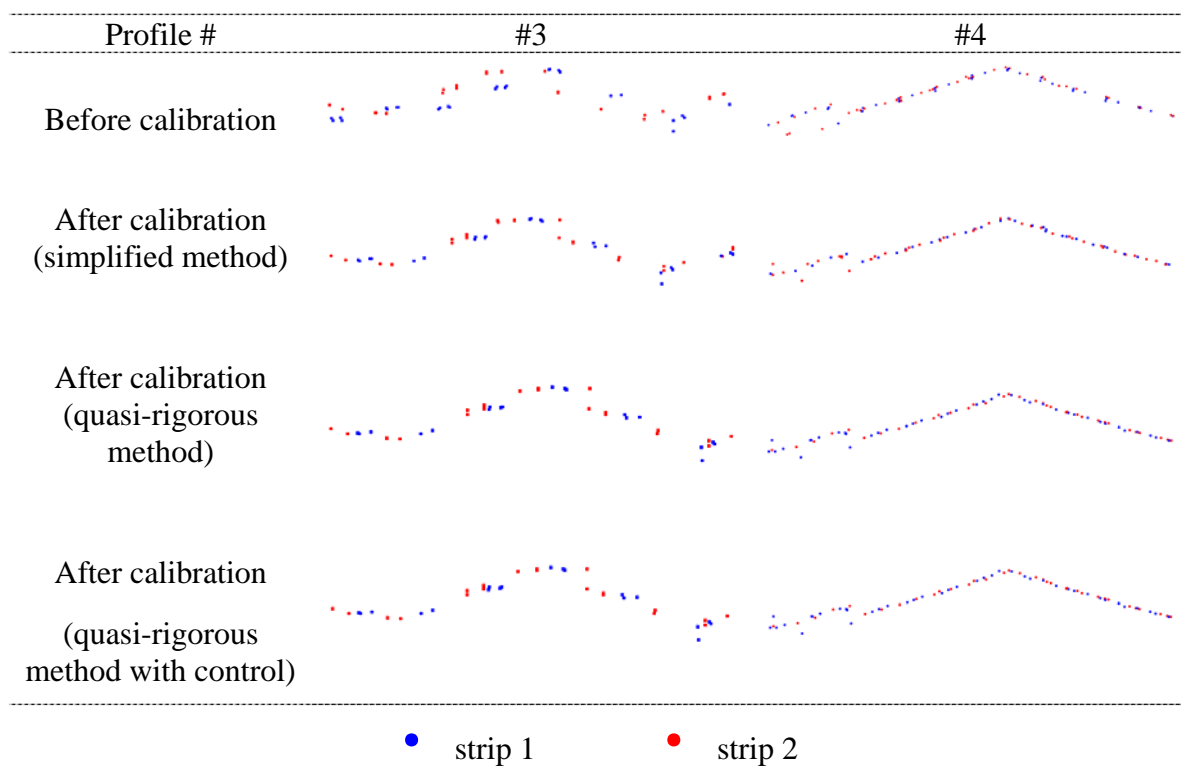
Figure 5.7. Profiles in the overlapping strip pair 1&2 (refer to Figure 5.6 for the location of these profiles) showing the degree of compatibility between the point cloud before and after the calibration procedure.

5.3.3   Quantitative Evaluation of the Calibration Results

In addition to the qualitative evaluation, a quantitative evaluation is performed in this section. For the quantitative evaluation, the overlapping strips 7&8, which were not involved in the calibration procedures, are utilized. The compatibility of these overlapping strips is evaluated before the calibration; then, the compatibility analysis is performed again after adjusting the point cloud using the estimated biases. With the help of the ICPatch procedure, which has been utilized to estimate the transformation parameters between overlapping strips, the discrepancies between strips 7&8 using the original and adjusted point cloud according to the estimated biases from the different

calibration methods are reported in Table 5.23. As shown in the table, one can see that the compatibility between the overlapping strips is improved after removing the impact of the estimated biases especially using the quasi-rigorous method. One should note that this work has focused on the implementation of system calibration procedures. More specifically, we are interested in detecting biases in the system parameters and reducing their impact on the derived point cloud. This does not mean that the adjusted point cloud will be error-free. Other errors, such as navigation errors, will still impact the quality of the derived point cloud as well as the estimated transformation parameters between adjusted overlapping strips. These errors cannot be included in a system calibration procedure since they are mission-dependent. Table 5.23 also shows that utilizing control data does not seem to have a significant effect on improving the quality of the compatibility among the strips – compare the last two rows in Table 5.23.

Table 5.23. Discrepancy evaluation between the bias-contaminated (before) and adjusted (after) point cloud coordinates of strips 7&8 for the different calibration procedures with respect to the ground coordinate system.

	X_T (m)	Y_T (m)	Z_T (m)	ω (")	φ (")	κ (")
Before	0.48	0.82	0.06	1.80	-166.32	-2.88
After (simplified)	0.54	0.44	0.05	2.88	-46.8	-9.00
After (quasi-rigorous with no control data)	0.23	0.28	0.05	3.24	8.28	-10.08
After (quasi-rigorous with vertical control data)	0.25	0.28	0.05	3.24	7.92	-10.08

For further evaluation of the relative performance of the simplified method and the quasi-rigorous method with and without control data, one can compare the adjusted point cloud coordinates for a given strip using the respective estimates of the biases in the system parameters. The estimated biases from two calibration experiments will be deemed compatible if the mean/RMSE values resulting from the comparison of the adjusted point cloud coordinates in each method are within the range of the noise level in point cloud. The compatibility analysis (mean/RMSE results) among the adjusted point cloud using estimated biases in Table 5.21 is summarized in Table 5.24. For such an analysis, we corrected the point cloud coordinates for two strips captured from two flight altitudes (2,000m and 1,000m for strips 1 and 7, respectively). In Table 5.24, one can see the high compatibility between two point clouds adjusted by the quasi-rigorous method with/without control data. It shows that the quasi-rigorous method is not much dependent on the use of control data, except the case of large bias ($\delta\Delta Z$) in lever-arm offset. On the other hand, the estimated biases in the simplified method produce an adjusted point cloud that slightly vary from the adjusted point cloud using the quasi-rigorous method, especially in the vertical directions. The observed incompatibility between the simplified and quasi-rigorous methods is attributed to the quality of the estimated range bias in the simplified method. As shown in Figure 2.11e, the range bias causes almost constant discrepancies across the flight direction between overlapping strips within small encoder angles, regardless flight altitude and overlapping ratio. In addition, the biases of range measurement and encoder angle scale factor cannot be easily coupled. To verify such a hypothesis, the compatibility analysis among the three bias estimates from the simplified

and quasi-rigorous methods while ignoring the estimated range bias (i.e., assuming a zero range bias) is conducted.

Table 5.24. Compatibility (mean/RMSE) analysis between the adjusted point clouds by the estimated biases in Table 5.21.

Simplified vs. quasi-rigorous (without vertical control data)						
Strips	Mean			RMSE		
	X (m)	Y (m)	Z (m)	X (m)	Y (m)	Z (m)
strip 1	0.114	-0.128	0.251	0.154	0.181	0.254
strip 7	0.100	-0.172	-0.259	0.104	0.174	0.261
Simplified vs. quasi-rigorous (with vertical control data)						
Strips	Mean			RMSE		
	X (m)	Y (m)	Z (m)	X (m)	Y (m)	Z (m)
strip 1	-0.114	0.130	-0.312	0.154	0.181	0.314
strip 7	0.099	-0.167	-0.319	0.103	0.168	0.320
Quasi-rigorous (without vertical control) vs. quasi-rigorous (with vertical control)						
Strips	Mean			RMSE		
	X (m)	Y (m)	Z (m)	X (m)	Y (m)	Z (m)
strip 1	0.000	-0.002	0.061	0.001	0.004	0.061
Strip 7	0.001	-0.005	0.060	0.002	0.006	0.060

The mean/RMSE values for this compatibility test are reported in Table 5.25, where we can see high compatibility among the different calibration methods. From this result, one can conclude that the estimated range bias might not be quite reliable for a system with a small scan angle in the absence of control data due to the weak variation of the impact of the range bias across the flight direction (i.e., the range bias would almost lead to constant elevation change across the flight direction for relatively small scan angle (20°), which is the case for the utilized real dataset) (refer to Equations 3.7d).

In this section, the experimental results using real dataset have confirmed the findings of the simulated dataset. Namely, the validity of the simplified and quasi-rigorous methods in the estimation of biases in the system parameters and removing the impact of such biases from the point cloud coordinates. Moreover, the real dataset has shown that the estimation of range biases might not be reliable when using overlapping strips with small scan angles in the absence of control data. In the next section, photogrammetric data is available as well as LiDAR strips captured over the same area. Using these datasets, the absolute and relative accuracy will be evaluated before/after the calibration.

Table 5.25. Compatibility (mean/RMSE) analysis between the adjusted point clouds by the estimated biases in Table 5.21 after ignoring the laser range bias.

Simplified vs. quasi-rigorous (without vertical control data)						
Strips	Mean			RMSE		
	X (m)	Y (m)	Z (m)	X (m)	Y (m)	Z (m)
strip 1	0.115	-0.129	0.033	0.159	0.188	0.049
strip 7	-0.101	0.172	0.040	0.107	0.174	0.050
Simplified vs. quasi-rigorous (with vertical control data)						
Strips	Mean			RMSE		
	X (m)	Y (m)	Z (m)	X (m)	Y (m)	Z (m)
strip 1	0.116	-0.136	0.034	0.162	0.195	0.051
strip 7	-0.103	0.177	0.041	0.110	0.180	0.051
Quasi-rigorous (without vertical control) vs. quasi-rigorous (with vertical control)						
Strips	Mean			RMSE		
	X (m)	Y (m)	Z (m)	X (m)	Y (m)	Z (m)
strip 1	0.002	-0.007	0.001	0.004	0.008	0.002
Strip 7	-0.002	0.005	0.001	0.003	0.005	0.001

5.4 Real Data Experiment II

This section will present the validity of the proposed methods using another real dataset consisting of LiDAR and photogrammetric data. The performance of the proposed calibration methods will be discussed with respect to the relative and absolute accuracy improvement after adjusting point cloud coordinates using estimated systematic biases. The impact on the relative accuracy will be assessed by quantifying the degree of compatibility between conjugate surface elements in overlapping strips before and after reconstructing the point cloud using the estimated system biases from both calibration methods. In a similar way of the previous test, the compatibility will be evaluated by computing the 3D transformation parameters between the overlapping strips before and after the calibration procedure. To evaluate the impact on the absolute accuracy of the point cloud, LiDAR linear and planar features will be used for the geo-referencing of an image block captured over the same area. The methodology used for photogrammetric geo-referencing utilizing control linear and planar features is detailed in Ghanma (2006); Shin et al. (2007). The absolute accuracy of the derived ground coordinates from the geo-referenced image block is evaluated using a check point analysis.

As shown in Figure 5.8, the LiDAR data captured by Leica ALS50 consist of six strips which have two different flight altitudes (1,150m and 540m) and four flight directions: south to north (strip 2), north to south (strip 1), east to west (strips 3, 5, and 6), and west to east (strip 4). The point density, PRF, and scan angle of the strips are about 1.5 - 4.0 points/m^2, 85 – 135 kHz, and ±20°, respectively. The photogrammetric data consist of 32 images captured by Rollei P-65 which has an array dimension of 8984×6732 pixels and a

focal length of about 60mm. The image block consists of 6 strips. Table 5.26 shows the flight configuration of the photogrammetric data. As shown in this table, 4 strips are flown in flight altitude 540m from east to west; the other two strips are flown in opposite directions (north to south and south to north) with flight attitude 1,150m. The ground resolutions are 5cm and 10cm for 1,150 and 540m flight attitudes, respectively. Field surveying data of 37 ground reference points is available. The points were captured by DGPS surveying over the photogrammetric data area. These points will be used as check points to evaluate photogrammetric bundle adjustment results. Figure 5.9 shows the distribution of the 37 check points over the area of photogrammetric data.
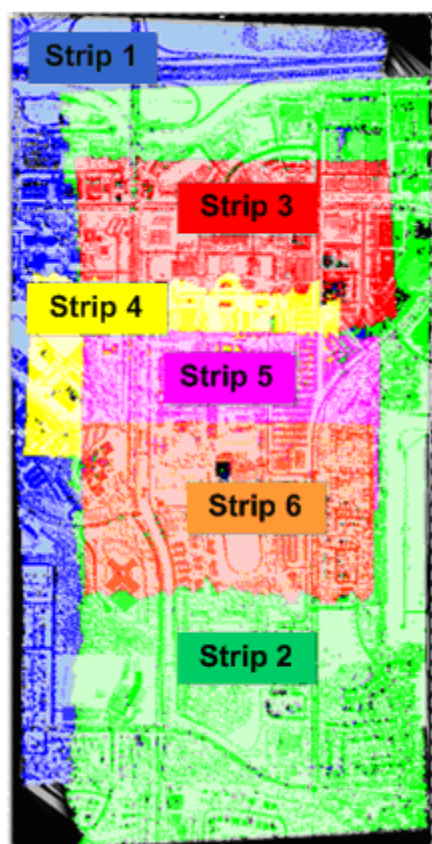
Strip Number	Flight altitudes	Flight directions
1	1,150 m	N-S
2	1,150 m	S-N
3	540 m	E-W
4	540 m	W-E
5	540 m	E-W
6	540 m	E-W

Figure 5.8. Strip configuration of the real dataset captured by Leica ALS50.

Table 5.26. Flight configuration for the photogrammetric data.

Strip #	Flight altitude [m]	Flight direction	Number of images
1	540	E-W	6
2	540	E-W	6
3	540	E-W	6
4	1,150	N-S	4
5	1,150	S-N	4
6	540	E-W	6
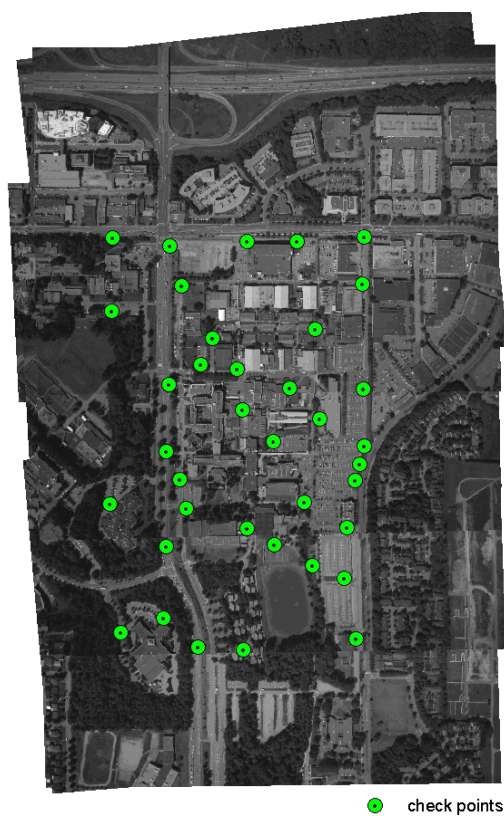
Figure 5.9. Distribution of 37 check points and photogrammetric data coverage.

In order to estimate the biases in the system parameters, four overlapping strip pairs are utilized from these LiDAR strips. Table 5.27 and Figure 5.10 show the characteristics of

the overlapping strip pairs which consist of three overlapping strip pairs flown in opposite flight directions and one overlapping strip pair flown in same flight direction.

Table 5.27. Overlapping strip pairs and their overlap ratio and flight directions.

Overlapping strip pairs	Overlap ratio (%)	Lateral distances (m)	Flight directions
Strips 1&2	80%	56	Opposite directions
Strips 3&4	25%	261	Opposite directions
Strips 4&5	75%	146	Opposite directions
Strips 5&6	50%	227	Same direction

Strips 1 (N-S) and 2 (S-N)   Strips 3 (E-W) and 4 (W-E)

H: 1,150m; D: 56m   H: 540m; D: 261m
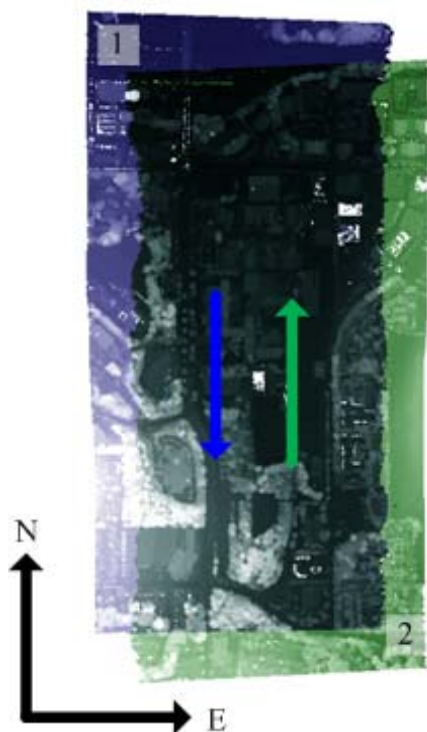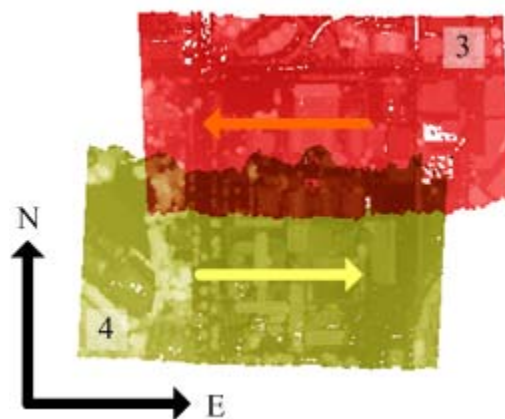
| Strips 4 (W-E) and 5 (E-W) | Strips 5 (E-W) and 6 (E-W) |
| H: 540m; D: 146m | H: 540m; D: 227m |
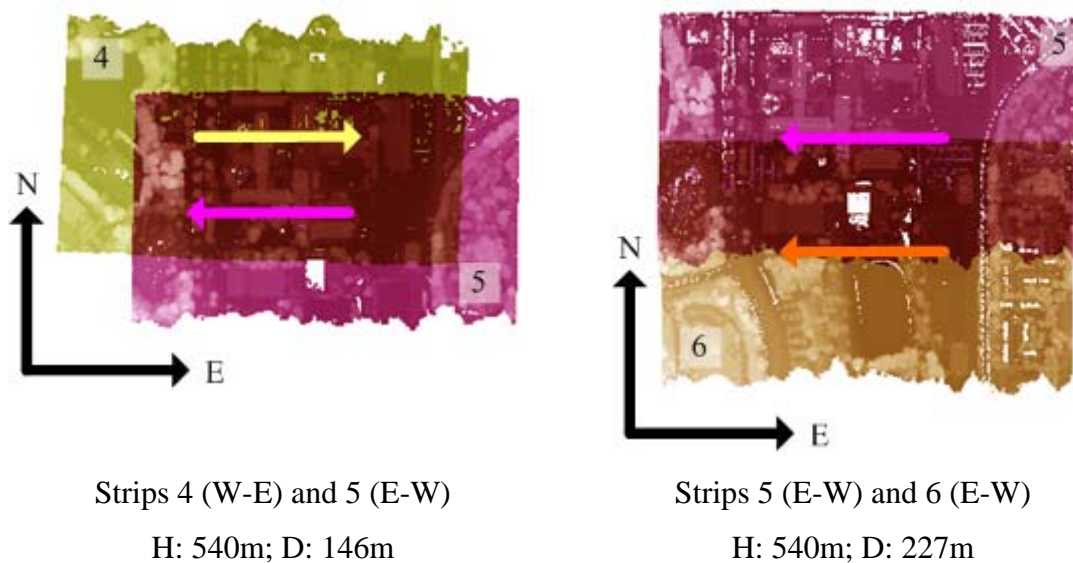
Figure 5.10. Illustration of the overlapping strip pairs involved in the experimental results from the second real dataset.

5.4.1 Calibration Results

In a similar way of the previous real data test, the biases in the system parameters are estimated by the simplified and quasi-rigorous methods. Table 5.28 reports the transformation parameters for four overlapping strip pairs (refer to Table 5.27 and Figure 5.10) with respect to the user defined local coordinate system. The simplified method estimated the biases in the system parameters using the transformation parameters reported in Table 5.28 through Equations 3.18 and 3.20. On the other hand, the quasi-rigorous method estimates the biases using Equation 3.27.

Table 5.29 reports the biases in the system parameters estimated by the simplified and quasi-rigorous methods. In

Table 5.29, one can see that the estimated bias in the boresight roll angle is significantly large compared to other biases. The impact of this bias can be confirmed by the estimated

transformation parameters in Table 5.28. In this table, one can see that the most significant discrepancies occurred across the flight directions for the overlapping strips flown in opposite directions. The estimated X_T (shift across the flight direction) from overlapping strip pairs 1&2, 3&4, and 4&5 are significantly larger than the other transformation parameters. On the other hand, the estimated X_T from strips 5&6 are relatively small because the bias $\delta\Delta\varphi$ which is the most significant bias in

Table 5.29 does not affect the discrepancies across the flight direction between the overlapping strips flown in same direction. In addition, one can see the estimated X_T from overlapping strips 1&2 is larger than the estimated X_T from overlapping strip pairs 3&4 and 4&5, because the impact of the bias $\delta\Delta\varphi$ depends on the flight altitude, and the flight altitude of overlapping strips 1 and 2 is much higher (1,150m) than the flight altitude (540m) of strips 3, 4, and 5. The analysis of discrepancy evaluation for overlapping strips will be further discussed in the next section.

Table 5.28. Estimated transformation parameters with respect to the user defined local coordinate system using the discrepancy detection procedure.

	X_T (m)	Y_T (m)	Z_T (m)	φ (°)
strips 1&2	1.10	-0.33	-0.01	0.0520
strips 3&4	0.40	-0.19	0.00	-0.0475
strips 4&5	0.57	-0.13	0.12	-0.0506
strips 5&6	-0.08	0.06	-0.08	0.0059

Table 5.29. Estimated biases in the system parameters using the simplified (based on the values in Table 5.28) and quasi-rigorous methods.

Methods	$\delta\Delta X$(m)	$\delta\Delta Y$(m)	$\delta\Delta\omega$(")	$\delta\Delta\varphi$(")	$\delta\Delta\kappa$(")	$\delta\Delta\rho$(m)	δS
Simplified	0.03	-0.01	-25.92	-91.08	-19.08	0.18	0.00005
Quasi-rigorous	-0.01	0.02	-39.60	-92.16	-6.12	0.21	-0.00003

5.4.2 Relative Accuracy Evaluation

The impact of the proposed calibration procedures on the relative accuracy of the point cloud is qualitatively evaluated by the comparison of selected profiles. Figure 5.11 illustrates the five profile locations and the overview of the area where the profiles are selected. The profile evaluation is conducted for strips 1, 2, 3, and 4. Figure 5.12 shows the compatibility of the profiles before/after the calibration for both the simplified and quasi-rigorous method. One can see that the profile compatibility is improved after the calibration. However, there is no noticeable difference between the simplified and quasi-rigorous methods.

The calibration results are quantitatively evaluated by computing the discrepancies between overlapping strips before and after the calibration procedure. The computed discrepancies are reported in Table 5.30. One should note that, in this table, X_T, Y_T, and Z_T denote translation parameters along the ground east, north, and up, respectively; ω, φ, and κ denote rotation angles around ground east, north, and up, respectively. As observed in this table, the two methods provided compatible results. Also, a significant

improvement can be observed, especially in the across flight direction between strips flown in opposite directions (X_T direction for strips 1&2, and Y_T direction for strips 3&4 and strips 4&5 – refer to highlighted cells in Table 5.30). This is expected since a larger bias was estimated in the boresight roll angle as previously discussed, which mainly affects the across flight direction (i.e., constant shift across the flight direction and a rotation around the flight direction). Insignificant improvement can be observed for strips 5&6 in Table 5.30. This is due to the fact that for strips flown in the same direction. The roll bias only causes near constant vertical shift between conjugate surfaces elements with a relatively small magnitude. In the next section, the improvement of the absolute accuracy will be analyzed using the integration of photogrammetric and LiDAR data.
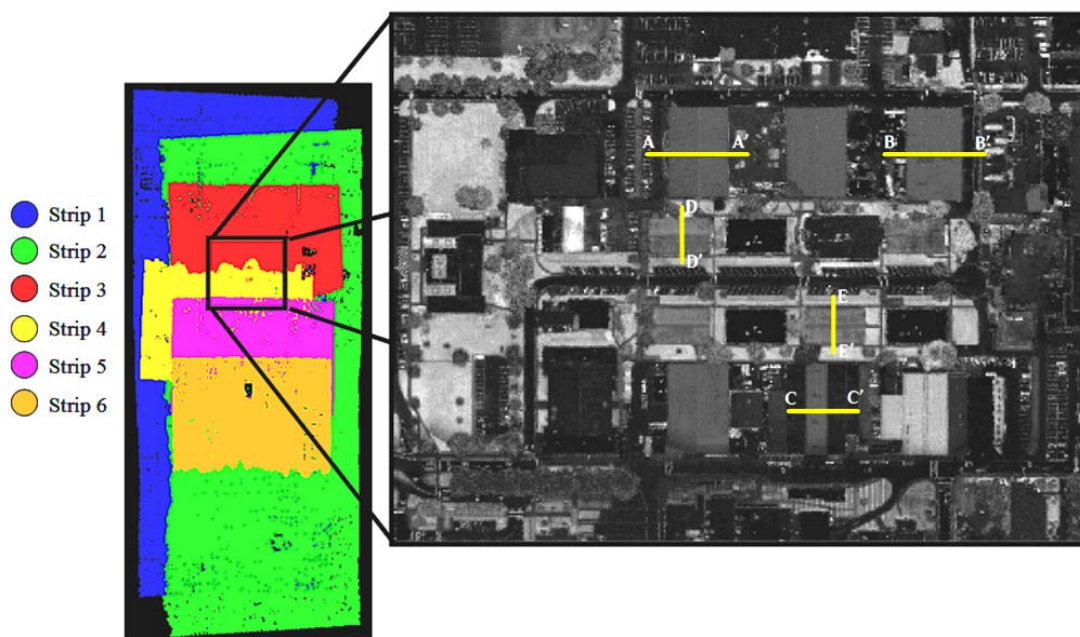
Figure 5.11. Location of the selected profiles for the qualitative compatibility check.
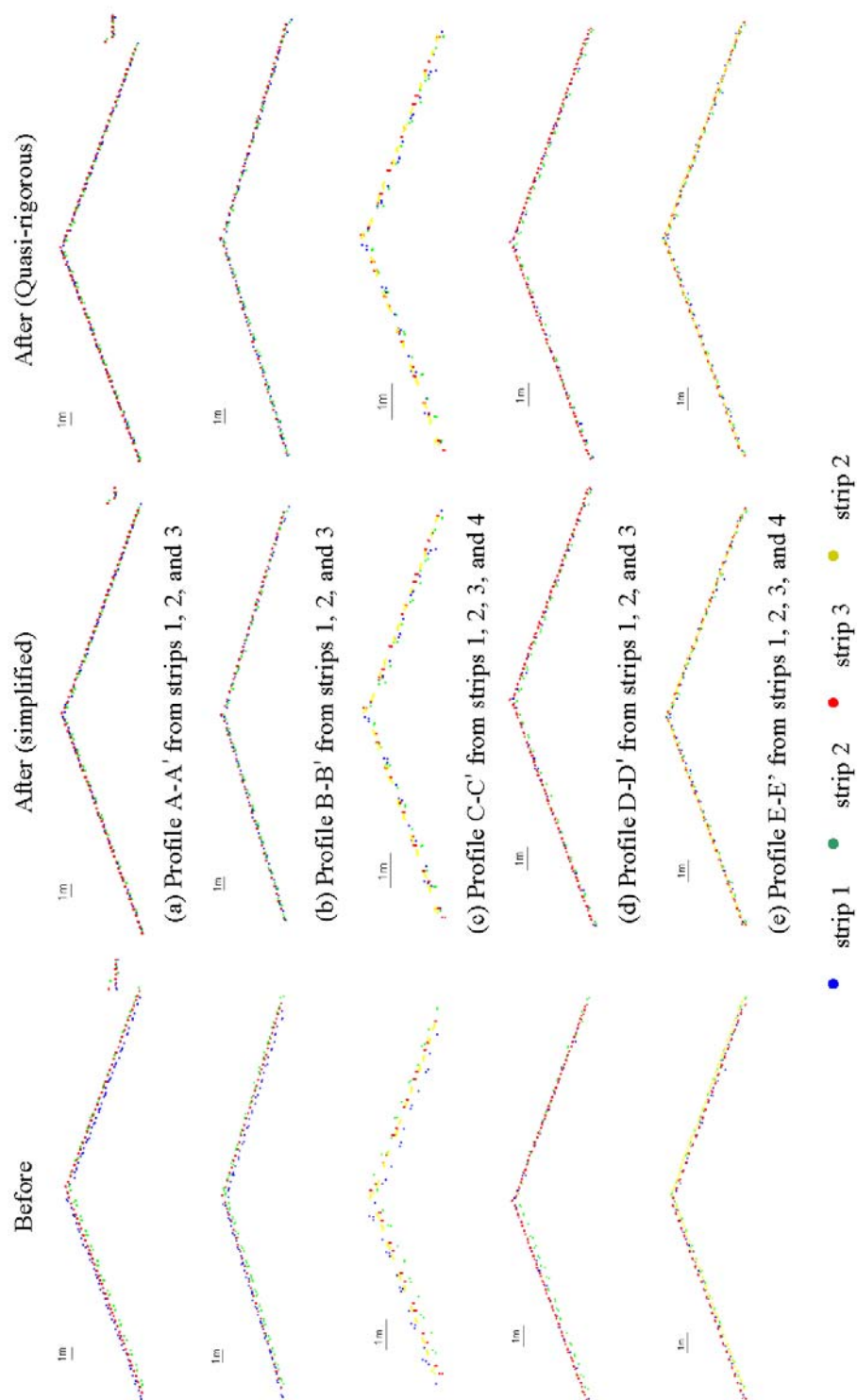
Figure 5.12. Profile comparison before and after the calibration procedure (the quasi-rigorous method).

Table 5.30. Compatibility analysis with respect to the ground coordinate system using the evaluation of discrepancies between overlapping strips before and after the calibration (the simplified and quasi-rigorous methods).

Before Calibration			After Calibration					
			Simplified Method			Quasi-rigorous Method		
Strips 1&2 (opposite directions)								
X_T (m)	Y_T (m)	Z_T(m)	X_T (m)	Y_T (m)	Z_T(m)	X_T (m)	Y_T (m)	Z_T(m)
1.10	-0.32	0.11	**-0.01**	-0.08	-0.05	**0.11**	0.07	-0.05
ω (°)	φ (°)	κ (°)	ω (°)	φ (°)	κ (°)	ω (°)	φ (°)	κ (°)
0.0001	**-0.052**	0.0012	0.0006	**-0.0027**	-0.0045	0.0012	**-0.0016**	-0.0051
Strips 3&4 (opposite directions)								
X_T (m)	Y_T (m)	Z_T(m)	X_T (m)	Y_T (m)	Z_T(m)	X_T (m)	Y_T (m)	Z_T(m)
0.18	**0.41**	-0.01	0.03	**-0.26**	0.00	-0.01	**-0.01**	0.01
ω (°)	φ (°)	κ (°)	ω (°)	φ (°)	κ (°)	ω (°)	φ (°)	κ (°)
0.0484	-0.0005	0.0052	**0.0053**	0.0009	-0.0046	**0.0052**	0.0008	-0.0045
Strips 4&5 (opposite directions)								
X_T (m)	Y_T (m)	Z_T(m)	X_T (m)	Y_T (m)	Z_T(m)	X_T (m)	Y_T (m)	Z_T(m)
-0.13	**-0.58**	0.07	0.04	**-0.04**	0.03	0.07	**-0.04**	0.03
ω (°)	φ (°)	κ (°)	ω (°)	φ (°)	κ (°)	ω (°)	φ (°)	κ (°)
-0.0506	-0.0004	0.0039	**-0.0019**	0.0000	-0.0031	**0.0039**	-0.0001	-0.0054
Strips 5&6 (same direction)								
X_T (m)	Y_T (m)	Z_T(m)	X_T (m)	Y_T (m)	Z_T(m)	X_T (m)	Y_T (m)	Z_T(m)
-0.06	-0.09	-0.05	-0.01	-0.19	0.02	-0.05	-0.03	0.03
ω (°)	φ (°)	κ (°)	ω (°)	φ (°)	κ (°)	ω (°)	φ (°)	κ (°)
-0.0049	0.0014	0.0005	-0.0041	0.0003	0.0077	0.0005	0.0018	0.0076

5.4.3 Absolute Accuracy Evaluation

To check the impact of the calibration procedures on the absolute accuracy, LiDAR linear and planar features have been extracted and used for the geo-referencing of an image block. The quality of the derived ground coordinates from the geo-referenced image block was evaluated using a check point analysis. Figure 5.13a shows the distribution of triangular patches corresponding to the planar patched extracted from the LiDAR data; Figure 5.13b shows the distribution of the linear features which are derived by the intersection of adjacent planar patches extracted in LiDAR data. The photogrammetric data is geo-referenced by the linear and areal features which are extracted from LiDAR data to be used as control data before/after the calibration. The RMSE analysis for the 37 check points after the photogrammetric data geo-referencing is listed in Table 5.31. One can see that the results using planar features before the calibration are much worse than the results using linear features. This might be due to the extraction process of the linear features, which are derived from the intersection of two planar patches such as gable roofs. This extraction process might cancel the effect of some of the biases. The relatively better performance of the linear features after the calibration procedure might be due to the fact that the utilized patches had a relatively mild slope, which might reduce the reliability of the geo-referencing results. Regardless of using linear or planar features significant improvement in the horizontal accuracy can be observed after the calibration for both methods. For example, when linear features are utilized as control data, $RMSE_{TOTAL}$, which is computed by total errors in X, Y, and Z coordinates, was improved from 0.34m to 0.22m in the simplified method, while the improved absolute accuracy in the quasi-rigorous method was 0.23m. As expected, less improvement is observed in the

vertical accuracy since detected biases in the system mounting parameters mainly affect the horizontal accuracy. From the check point RMSE analysis results, one can see the performance of the proposed methods (the simplified and quasi-rigorous methods) is verified with respect to the absolute accuracy.

Table 5.31. RMSE analysis of the 37 check points for the photogrammetric data geo-referenced by the control linear features and planar patches extracted from the LiDAR data as control data before/after the calibration.

	Before the calibration	After the calibration	
		Simplified	Quasi-rigorous
	Linear/Planar features	Linear/Planar features	Linear/Planar features
Mean ΔX (m)	-0.03/-0.36	-0.01/-0.10	-0.01/-0.09
Mean ΔY (m)	-0.18/0.67	0.06/0.24	-0.05/0.17
Mean ΔZ (m)	0.15/-0.05	-0.07/-0.15	0.11/-0.21
σ_X (m)	0.11/0.40	0.06/0.11	0.05/0.10
σ_Y (m)	0.15/0.29	0.08/0.06	0.06/0.07
σ_Z (m)	0.17/0.24	0.17/0.13	0.18/0.13
$RMSE_X$ (m)	0.11/0.53	0.06/0.14	0.05/0.13
$RMSE_Y$ (m)	0.23/0.72	0.10/0.24	0.07/0.18
$RMSE_Z$ (m)	0.23/0.25	0.18/0.20	0.21/0.25
$RMSE_{TOTAL}$ (m)	0.34/0.93	0.22/0.35	0.23/0.33
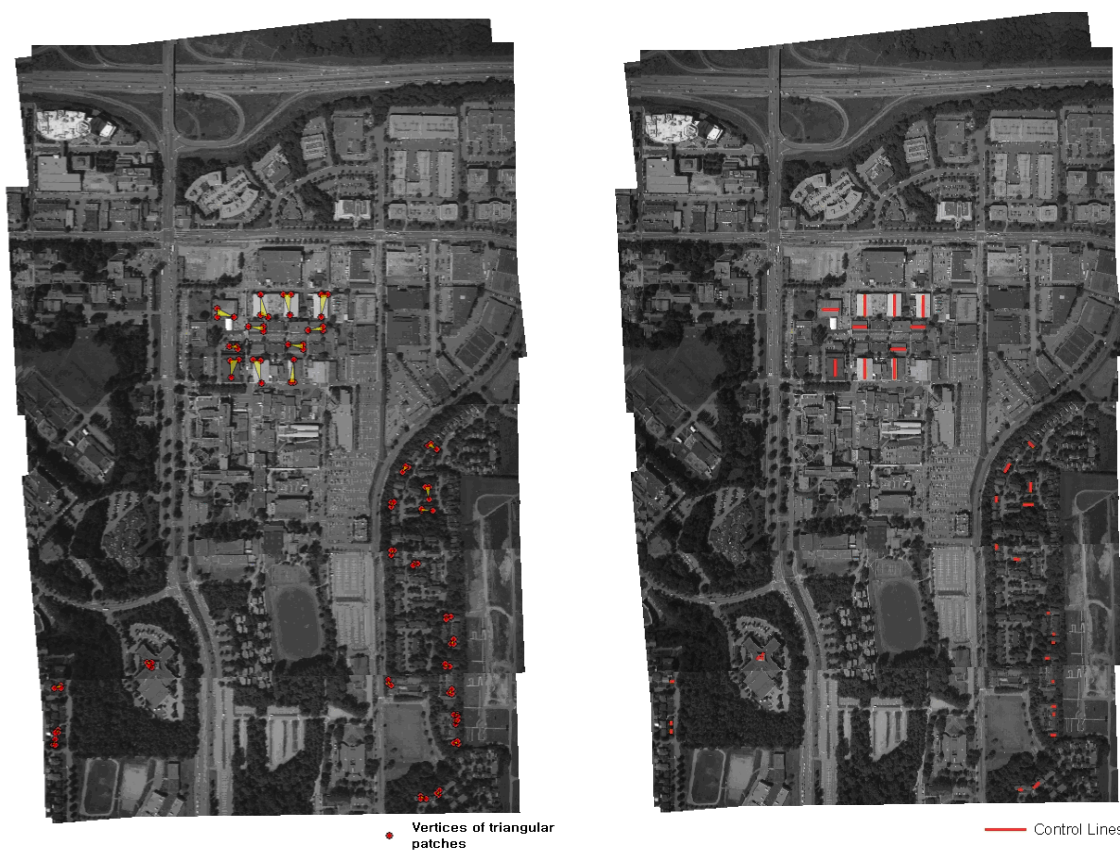
(a)   (b)

Figure 5.13. Distribution of (a) triangular patches and (b) linear features corresponding to features extracted from the LiDAR data used as control for photogrammetric geo-referencing.

CHAPTER 6

CONCLUSIONS AND RECOMMENDATIONS FOR FUTURE WORK

6.1   Conclusions

The availability of 3D surface data is very important for various applications such as ortho-photo generation, forest mapping, and urban modeling. A LiDAR system has been proven as a cost-effective tool for the generation of 3D data over extended areas since it can quickly provide accurate surface models with a dense set of irregularly spaced points. A typical LiDAR system is an active sensor system consisting of GPS/INS and a laser scanner. Point cloud derived by a LiDAR system can be distorted by random and systematic errors in the system measurements and mis-alignment between the individual components. This research aimed at analyzing the random and systematic errors of a linear scanning system in terms of their impact on the derived point cloud. In addition, alternative calibration methods integrated with a surface matching procedure were proposed. The proposed methods can be used in the case where the point cloud coordinates of overlapping strips are available, but where raw measurements are not utilized. The following will review research findings for the LiDAR error analysis, alternative calibration methods, and experimental results from the simulated and real datasets.

6.1.1   Random errors

This research started with confirming the impact of random and systematic errors introduced in the previous research. The impact of the random errors on the point cloud

coordinates can be evaluated by two ways: LiDAR data simulation and the law of error propagation. The noise in the platform positions causes similar errors in the derived point cloud, and the magnitude of the impact dose not change regardless the variation of flight altitudes and encoder angles. On the other hand, the impact of the noise in the platform orientation and laser scanner encoder angles is more negative on the planimetric accuracy rather than the height accuracy. The angular noise causes minimum height errors in the nadir region, while maximum height errors are found at the swath edges. In addition, the impact of the angular noise increases when LiDAR strips are captured at a higher flight altitude. The noise in laser range measurement mainly affects the vertical accuracy of the derived coordinates within nominal scan angle ranges (e.g., $\pm 25°$). The impact of the range noise is independent of flight altitude change.

6.1.2   Systematic errors

The biases in the lever-arm offsets cause almost constant errors in both planimetric and vertical coordinates. The errors caused by a bias in the lever-arm offset along the vertical direction do not change regardless of the flight direction. The bias in the boresight pitch causes near constant errors along the flight direction, which is similar to the effect of a bias in the lever-arm offset along the flight direction. The higher flight altitude however increases the impact of this bias. The bias in boresight roll causes errors across the flight direction as well as the vertical direction, while there is no error along the flight direction. The errors across the flight direction are almost constant. On the other hand, the errors along the vertical direction are minimized around the nadir areas, and maximized at the swath edges. The bias in the boresight yaw mainly causes errors along the flight direction

whose magnitudes increase with the increase in the off-nadir encoder angle. The height errors caused by biases in the range measurement and scale factor of encoder angles have curved shapes along the scan-lines. The errors caused by the bias in the encoder angle scale factor are close to zero around the nadir area, while the errors caused by the bias in the range measurements are maximized in that area.

6.1.3 Alternative calibration methods

The achievement of the full potential accuracy of a LiDAR system requires the elimination of all systematic errors. In this research, two alternative methods were proposed to estimate the systematic biases and eliminate their impacts for a linear scanning system. These methods can overcome the limitations of existing calibration procedures in terms of requirements of system raw measurements. The first proposed method, denoted as the simplified method, was developed with a few assumptions such as relatively flat terrain, levelled scanning, parallel flight lines, and small boresight angles. Based on the assumptions, this research simplified the LiDAR geo-referencing equation and derived the 4-parameter (three shifts and rotation around the flight direction) 3D transformation function to represent the discrepancies between overlapping strips. The simplified method consists of two steps. First, the transformation parameters are estimated using the point cloud coordinates of overlapping strips. Second, the biases in the system parameters are calculated by the estimated transformation parameters. If overlapping strips are non-straight and captured with varying flight altitudes, one can split the strips into several sub-strips, which are suitable for the simplified method.

The second proposed method, denoted as the quasi-rigorous method, can deal with non-parallel strips, heading variations, and varying terrain elevations using time-tagged point cloud and trajectory position data. The quasi-rigorous method was developed with the following assumptions: levelled scanning and small boresight angles. This method can utilize not only overlapping strips, but also control data if available. The use of control data contributes to decoupling the biases in the range measurements and encoder angle scale factor.

The point cloud adjustment procedures for both the simplified and quasi-rigorous methods were introduced. The simplified method can adjust the bias-contaminated point coordinates using approximate estimates of the lateral coordinate x, encoder angle β, flight altitude, and estimated systematic biases. In this procedure, the lateral coordinates and encoder angles can be calculated by estimated scan-line centers and average flight altitude. One should note that the calculated coordinate corrections should be rotated using the flight direction before applying them to the biased coordinates since the coordinate corrections are calculated with the assumption that the flight direction is along the ground Y axis. In the quasi-rigorous method, the bias-contaminated point coordinates are adjusted by a function of the estimated biases, and calculated parameters from the trajectory fitting procedure such as the flight direction, lateral coordinate x, encoder angle β, and vertical distance between firing point and LiDAR point.

6.1.4   Surface matching

In this research, identifiable features, such as points, lines, and planar patches, were not used since it is not expected that those features are always available in point cloud data.

Instead of the use of distinct features, a surface matching procedure was utilized to establish correspondences between the overlapping strips. For the utilized surface matching procedure (ICPatch), two overlapping strips were represented by original point cloud and TIN format, respectively. In these overlapping strips, the ICPatch procedure finds the closest point-patch pairs for corresponding features. The volume constraint was introduced as a similarity measure for matched point-patch pairs. In this constraint, the similarity is measured by the volume of the tetrahedron which consists of the matched point and triangular patch. In the simplified method, the four transformation parameters are determined when the transformed corresponding point coordinates minimize the tetrahedron volume, while the quasi-rigorous method determines the biases in the system parameters when the corrected four vertices of the tetrahedron minimize the volume. In addition to the volume constraint, a point-based similarity measure was introduced. In this approach, pseudo-conjugate points are derived from the matched point-patch pair. The pseudo-conjugate points consist of the matched point and an arbitrarily chosen vertex from the matched triangular patch. Since the pseudo-conjugate points are not true corresponding points, the weight matrix for the chosen vertex point is modified to assign zero-weight along the patch. Using the modified weight matrix, the simplified method minimize the normal distance between the matched point and patch after transforming the matched point, while the quasi-rigorous method minimize the normal distance after correcting the pseudo-conjugate points using the estimated biases. The advantage of the modified weight matrix is that the mathematical model is relatively simple and easy to implement since there is no requirement to combine an additional equation representing alternative similarity measure such as a volume constraint.

6.1.5   Experimental results

The performances of the simplified and quasi-rigorous calibration methods were verified using simulated and real datasets. The main purpose of utilizing simulated data was to investigate the performance of the bias estimation and point cloud adjustment procedures, in a controlled environment. In addition, parallel/non-parallel and levelled/un-levelled overlapping strips were generated over the rugged object surface to study the impact of deviations from the assumptions which were used in the derivation of the proposed methods. The experimental results of the simulation datasets proved that the derived mathematical models were not sensitive to the assumptions with reasonable ranges of non-parallelism, terrain height variation, and platform attitude. The mean/RMSE analysis between the true and adjusted strips using the true biases was conducted to evaluate the performance of the point cloud adjustment procedures. In this analysis, one could confirm that all mean values were close to zero, and RMSE values were significantly decreased after adjusting the point clouds. After justifying the point cloud adjustment procedures, the performance of the proposed methods was verified by another mean/RMSE analysis which was conducted between true and adjusted point clouds using the estimated biases. After the calibration, one could confirm that the systematic errors in both the planimetric and vertical coordinates were notably improved. The overall quality of the results from the quasi-rigorous method was relatively better the quality of the results from the simplified method (especially in the non-parallel strip cases), which shows the contribution of handling the deviation of flight altitudes and terrain elevations of the quasi-rigorous method.

The biases in the system parameters were estimated using the simplified and quasi-rigorous methods for real LiDAR datasets captured by commercial/operational LiDAR systems. For the quasi-rigorous method, two cases were conducted. In the first case, the biases were estimated using only overlapping strips, while vertical control data were additionally utilized in the second case. The estimated biases by the quasi-rigorous method with/without the vertical control data were quite compatible, which was proven by the compatibility analysis between two point clouds adjusted by the quasi-rigorous method with/without control data. On the other hand, the bias in the range measurement estimated by the simplified method was relatively incompatible with the bias estimated by the quasi-rigorous method. It is attributed to the fact that the biases of range measurement and encoder angle scale factor cannot be easily decoupled. According to the systematic error analysis using the simulated data over the flat terrain, the bias in the range measurements causes almost constant discrepancies across the flight direction between overlapping strips within small encoder angles, regardless flight altitude and overlapping ratio. This fact can affect the quality of the range bias estimation. However, the variation of the terrain elevation and flight altitudes contributed to decoupling the biases in the range measurements and encoder angles for the quasi-rigorous method. In addition, the use of the control data can contribute to decoupling the biases in the case of a relatively flat object surface.

The performance of the proposed methods was analyzed with respect to the improvement in the relative and absolute accuracy for real datasets. The relative accuracy was qualitatively and quantitatively evaluated. One could confirm the improvement of the relative accuracy by the visual comparison of the profiles and intensity images

before/after the calibration. The quantitative evaluation of the relative accuracy was conducted by the ICPatch procedure. The discrepancies between overlapping strips were decreased after eliminating the impact of the biases in the system parameters. The improvement of the absolute accuracy was evaluated by the photogrammetric block adjustment. In this procedure, the LiDAR strips were used as control data for the image geo-referencing before/after the calibration. After the geo-referencing, the mean and RMSE values of ground check points were evaluated for verifying the impact of the calibration. The improvement of the absolute accuracy was confirmed by the reduced mean and RMSE values after the calibration for both the simplified and quasi-rigorous methods. Especially, the planimetric accuracy was significantly improved, which can be explained by the fact that the biases in the system parameters mainly affect the planimetric accuracy.

In summary, the contributions of this research can be summarized as follows: a) the random and systematic errors were analyzed in terms of their impact on the derived point cloud and discrepancies between overlapping strips, b) the discrepancies caused by the systematic biases between overlapping strips can be represented by a 4-parameter transformation function for parallel strips captured over relatively flat terrain, c) the simplified method can estimate the systematic biases using only point cloud coordinates of parallel overlapping strips, d) the quasi-rigorous method can handle non-parallel overlapping strips and variation in terrain elevations using trajectory position data, d) ICPatch procedure makes the calibration procedures possible without identifiable features, e) the modified weight matrix makes it possible to utilize point based similarity measure between matched point-patch pairs instead of the use of a coplanarity constraint such as a

volume constraint, f) the proposed methods can be used regardless the system configuration such as the definition of the coordinate systems related to IMU and laser scanner, g) the proposed method can efficiently adjust point cloud coordinates without the help of the system parameters and raw measurements, h) the simulation data tests verified that the proposed method were not sensitive to the assumptions used for simplifying the LiDAR geo-referencing equation, i) the experimental results from the real LiDAR datasets verified that the relative and absolute accuracy of LiDAR data could be improved by the proposed calibration methods using only overlapping strips, and j) the proposed calibration procedures can be used not only for estimating the systematic biases and adjusting point cloud data, but also LiDAR data quality control (QC).

6.2   Recommendations for Future Work

Future research will focus on modifying the proposed methods for a one-step procedure of the simplified method, and the use of additional data such as platform attitude data and system raw measurements for the quasi-rigorous method. The ICPatch procedure will be modified for improving its performance by automatically filtering patches that do not represent the physical surface and selecting suitable surface elements from TIN data. Further study on the optimal configuration of overlapping strips will be addressed to alleviate the correlation between the biases in range measurements and encoder angle scale factor. The remaining discrepancies between overlapping strips will be studied in terms of un-modelled systematic biases, and a standard for acceptable errors will be developed. The following discussions illustrate the recommendations for future work.

1. The simplified method is a two-step procedure. The transformation parameters estimated in the first step are valuable information because they can be used not only for estimating the systematic biases, but also for evaluating the compatibility of overlapping strip before adjusting point cloud. However, it should be mentioned that one can modify the simplified method for a one-step procedure. In order to implement the one-step procedure, the 4-parameter transformation used in the first step can be replaced with a function of systematic biases, flight altitude, and lateral distance between overlapping strips (refer to Equations 3.13, 3.14, and 3.16).

2. The quasi-rigorous method can be modified to accept platform attitude data in order to handle LiDAR strips captured with significant roll and pitch angles. Even though, the result of the simulation data (case 3) proved that $\pm 5°$ deviation of roll and pitch angles can be handled by the proposed method, one might need to calibrate a LiDAR system using overlapping strips flown with significant tilt. Without the platform attitude data, the roll and pitch angles can be approximately estimated after determining platform position and scan-line center. As a future work, it will be useful to compare the estimated orientation and platform orientation data. In addition, future work will consider another approach for integrating the rigorous LiDAR geo-referencing equation including the system raw measurements and the ICPatch procedure in order to estimate the systematic biases using overlapping strips without control data and distinct features.

3. The surface matching procedure (ICPatch) used in the proposed method showed reliable performance for establishing correspondences between point cloud and TIN data. Future research will focus on improving the performance of the ICPatch procedure. For

example, TIN patches not describing the physical surface can be eliminated before the surface matching procedure, and appropriate surface areas can be automatically selected by analyzing eigenvalues of surface elements. It can alleviate the computational load of the ICPatch procedure and increase the reliability of the matched point-patch pairs.

4. Further study for the optimal strip configuration to decouple the biases in range measurement and encoder angle scale factor is recommended. As previously discussed, both biases are correlated, especially in the case of a relatively small scan angle. In the quasi-rigorous, the use of control data is recommended to decouple these biases. Without control data, optimal overlapping strip configuration can be considered to decouple the biases. For example, Figure 6.1 shows overlapping strips A and B which are flown in same directions and captured at different flight altitudes. The scan angles of the strips are the same, and the lateral distance between the strips is D. As shown in the figure, the left edges of the strips meet together. In other words, it can be considered that the encoder angles of the overlapping strips are similar around the left side of the strips. In this case, the discrepancies caused by the bias in the range measurement between the overlapping strips are close to zero around the highlighted area in Figure 6.1, while the impact of the bias in the encoder angle scale factor is maximized in that area because the impact of the angular bias depends on a flight altitude. This can be mathematically illustrated using Equation 6.1. In this equation, H_A and H_B denote two different flight altitudes; β_A and β_B denote encoder angles of the strips A and B, and x_A and x_B are lateral coordinates of a ground object point relative to the laser unit frame. In Equation 6.1, the difference between β_A and β_B is considered small enough to be ignored in the highlighted area shown in Figure 6.1, and the difference of the lateral coordinates $(-x_A+x_B)$ depends on the

lateral distance between the overlapping strip. Therefore, the coordinate difference between corresponding points in the highlight area can be represented by a function of the biases in boresight angles, encoder angle scale factor, flight attitudes, and lateral distance between the strips (Equation 6.2).

<center>Impact of $\delta\Delta\rho$ Impact of δS</center>
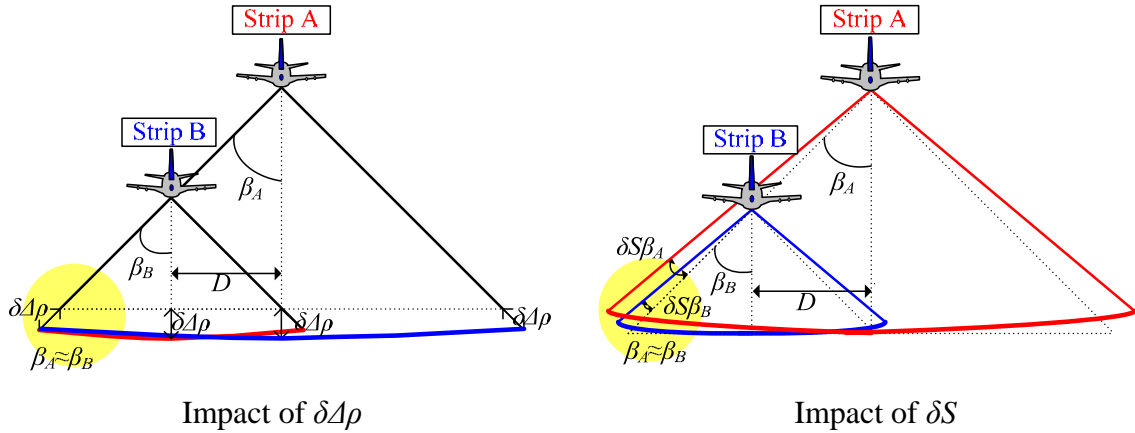
Figure 6.1. Special overlapping case to reduce the impact of the bias in the range measurement.

$$\begin{bmatrix} X_A - X_B \\ Y_A - Y_B \\ Z_A - Z_B \end{bmatrix} \approx \begin{bmatrix} -(H_A - H_B)\delta\Delta\varphi - (\sin(S\beta_A) - \sin(S\beta_B))\,\delta\Delta\rho - (H_A\beta_A - H_B\beta_B)\delta S \\ (H_A - H_B)\delta\Delta\omega + (x_A - x_B)\,\delta\Delta\kappa \\ -(x_A - x_B)\,\delta\Delta\varphi - (\cos(S\beta_A) - \cos(S\beta_B))\,\delta\Delta\rho - (x_A\beta_A - x_B\beta_B)\delta S \end{bmatrix} \quad (6.1)$$

$$\begin{bmatrix} X_A - X_B \\ Y_A - Y_B \\ Z_A - Z_B \end{bmatrix} \approx \begin{bmatrix} -(H_A - H_B)\delta\Delta\varphi - (H_A - H_B)\beta_A\,\delta S \\ (H_A - H_B)\delta\Delta\omega - D\,\delta\Delta\kappa \\ D\,\delta\Delta\varphi + D\beta_A\,\delta S \end{bmatrix} \quad (6.2)$$

5. A standard for acceptable discrepancies between overlapping strips will be developed in future research. Especially after the calibration, the remaining discrepancies between overlapping strips can be classified into two parts: random and systematic errors. The remaining random errors can be analyzed based on a system specification, while the

remaining system errors can tell us an evidence of un-modelled systematic biases such as biases in position and orientation data.

REFERENCES

Alharthy, A., Bethel, J., and Mikhail, E., 2004. Analysis and accuracy assessment of airborne laser-scanning system, *International Archives of the Photogrammetry, Remote Sensing and Spatial Information Sciences*, 35(B2): 144–149.

Ackermann, F., 1999. Airborne laser scanning - present status and future expectations, *ISPRS Journal of Photogrammetry and Remote Sensing*, Vol. 54, No. 2-3, pp. 64-67.

Anton, H., 2000. *Elementary Linear Algebra (8th Edition)*, John Wiley and Sons, INC., New York, US, 653p.

Applanix, 2007. POS AV specification, http://www.applanix.com/media/downloads /products/specs/POSAV_SPECS.pdf (accessed November 2007).

Baltsavias, E.P., 1999a. Airborne laser scanning - basic relations and formulas, *ISPRS Journal of Photogrammetry and Remote Sensing*, Vol. 54, No. 2-3, pp. 199-214.

Baltsavias, E.P., 1999b. Airborne laser scanning – existing systems and firms and other resources, *ISPRS Journal of Photogrammetry and Remote Sensing*, Vol. 54, No. 2-3, pp. 164-198.

Bang, K.I., Habib, A.F., Kusevic, K., and Mrstik, P., 2008. Integration of terrestrial and airborne LiDAR data for system calibration, *The International Archives of the Photogrammetry, Remote Sensing and Spatial Information Sciences*, WG I/2, 3-11 July, Beijing, China. pp. 391-398.

Bang, K.I., Habib, A.F., Kersting, A., 2010. Estimation of Biases in LiDAR System Calibration Parameters Using Overlapping Strips, *The Canadian Journal of Remote Sensing*, (accepted 2010).

Bergevin, R. Soucy, M., Gagnon, H., and Laurendeau, D., 1996. Towards a general multi-view registration technique, *IEEE Transactions on Pattern Analysis and Machine Intelligence*, Vol. 18, No. 5, pp. 540-547.

Besl, P., and McKay, N., 1992. A method for registration of 3-D shapes, *IEEE Transactions on Pattern Analysis and Machine Intelligence*, Vol. 14, No. 2, pp. 239-256.

Bossler, J. D., 2010. *Manual of Geospatial Science and Technology*, CRC Press, Boca Raton, US, 854p.

Brenner, C., 2006. Aerial laser scanning, International Summer School Digital Recording and 3D Modelling, 24-29 April, Crete, Greece, http://www.photogrammetry. ethz.ch/summerschool/ (accessed May 2010)

Bretar, F., Pierrot-Deseilligny, M., and Roux, M., 2004. Solving the strip adjustment problem of 3D airborne LiDAR data, *Proceedings of the IEEE IGARSS'04*, 20-24 September, Anchorage, US. pp. 4734-4737.

Burman, H., 2000. *Calibration and Orientation of Airborne Image and Laser Scanner Data Using GPS and INS*, Ph.D. Thesis, Photogrammetry, Reports No. 69, Royal Institute of Technology, Stockholm, Sweden.

Burman, H., 2002. Laser strip adjustment for data calibration and verification, *Photogrammetric Computer Vision (ISPRS Commission III Symposium)*, 9-13 September, Graz, Austria. Vol. 34, No. 3, A-67-72.

Chauve, A., Mallet, C., Bretar, F., Durrieu, S., Deseilligny, M. P., and Puech, W., 2007. Processing full-waveForm LiDAR data : modelling raw signals, *ISPRS Workshop on Laser Scanning 2007 and SilviLaser 2007*, 12-14 September, Espoo, Finland. pp. 102-107.

Chen, Y., and Medioni, G., 1992. Object modeling by registration of multiple range images, *Image and Vision Computing*, Vol. 10, No. 3, pp. 145-155.

Clode, S., Kootsookos, P., and Rottensteiner, F., 2004. The automatic extraction of roads from LiDAR data, *International Archives of Photogrammetry, Remote Sensing and Spatial Information Sciences, 35 (Part B3)*, pp. 231–236.

Crombaghs, M.J.E., Brügelmann, R., and Min E.J. de., 2000. On the adjustment of overlapping strips of laser altimeter height data, *International Archives of Photogrammetry and Remote Sensing*, 16-22 July, Amsterdam, the Netherlands. pp. 230-237.

El-Sheimy, N., Valeo, C., and Habib, A.F., 2005. *Digital Terrain Modelling: Acquisition, Manipulation And Applications (1st Edition)*, Artech House, Norwood, US, 257p.

Filin, S., 2003. Recovery of systematic biases in laser altimetry using natural surfaces. *Photogrammetric Engineering and Remote Sensing*, Vol. 69, No. 11, pp. 1235-1242.

Fugro EarthData, Inc., LiDAR mapping fact sheet, white paper published in the company web-site, web-site, http://www.fugroearthdata.com/pdfs/FCT_Lidar-Educational_11-07.pdf (accessed Sep 2010).

Ghanma, M., 2006. *Integration of Photogrammetry and LiDAR*, Ph.D. Dissertation, Department of Geomatics Engineering, the University of Calgary, Calgary, Canada.

Glennie, C., 2007. Rigorous 3D error analysis of kinematic scanning LiDAR systems, *Journal of Applied Geodesy*, Vol. 1, No. 3, pp. 147-157.

Gruen, A., and Akca, D., 2005. Least squares 3D surface and curve matching, *International Journal of Photogrammetry and Remote Sensing*, Vol. 59, pp. 151-174.

Habib, A. F., Lee, Y., and Morgan, M., 2001. Surface matching and change detection using a modified Hough transformation for robust parameter estimation, *Photogrammetric Record*, Vol. 17, No. 98, pp. 303-315.

Habib, A. F., Morgan, M., and Lee, Y., 2002. Bundle adjustment with self-calibration using straight lines, *Photogrammetric Record*, Vol. 17, No. 100, pp. 635-650.

Habib, A. F. and Morgan, M., 2003. Linear feature in photogrammetry, *Geodetic Science Bulletin*, Vol. 9, No. 1, pp. 3-24.

Habib, A. F., Ghanma, M., Morgan, M., and Al-Ruzouq, R., 2005. Photogrammetric and LiDAR data registration using linear features, *Photogrammetric Engineering and Remote Sensing*, Vol. 71, No. 6, pp. 699-707.

Habib, A. F., 2006. Advanced photogrammetric and ranging techniques (ENGO 531), Course Note of Department of Geomatics Eng., University of Calgary, Canada.

Habib, A.F., Cheng, R.W.T., Kim, E.M., Mitishita, E.A., Frayne, R., and Ronsky, J.L., 2006. Automatic surface Matching for the registration of LiDAR data and MR imagery, *ETRI Journal*, Vol. 28, No. 2, pp. 162-174.

Habib, A. F., Bang, K.I., Shin, S.W., and Mitishita, E., 2007. LiDAR system self-calibration using planar patches from photogrammetric data, *The 5th International Symposium on Mobile Mapping Technology*, [CD-ROM]. 28-31 May, Padua, Italy.

Habib, A. F., Kersting, A. P., Ruifang, Z., Al-Durgham, M., Kim, C., and Lee, D. C., 2008. LiDAR strip adjustment using conjugate linear features in overlapping strips. *International Archives of Photogrammetry, Remote Sensing and Spatial Information Sciences,* 3-11 July, Beijing, China. Vol. XXXVII, Part B1, pp. 385–390.

Habib, A. F., Bang, K.I., Kersting, A., and Lee D.C., 2009a. Error budget of LiDAR systems and quality control of the derived data, *Photogrammetric Engineering and Remote Sensing*, Vol. 75, No. 9, pp. 1093-1108.

Habib, A. F., Kersting, A., Bang, K.I., Zhai, R., and Al-Durgham, M., 2009b. A strip adjustment procedure to mitigate the impact of inaccurate mounting parameters in parallel LiDAR strips, *The Photogrammetric Record*, Vol 24, No. 126, pp. 171-195.

Harding, D. J., 2004. TerraPoint LiDAR mapping instrumentation and methodology, Documentation prepared by TerraPoint, LLC. 16 November. http:// denali.gsfc.nasa.gov/lidar/terrapoint/TerraPoint_System_Description. (accessed October 2009).

Hitz, B., Ewing, J. J., and Hecht, J., 1998. *Introduction to Laser Technology (3rd Edition)*. IEEE Press, New York, US, 302p.

Hug, C., Ullrich, A. and Grimm, A., 2004, LITEMAPPER-5600: a waveform-digitizing LiDAR terrain and vegetation mapping system. *International Archives of Photogrammetry, Remote Sensing and Spatial Information Sciences*, Vol. 36, Part 8/W2, pp. 24-29.

Huising, E.J. and Gomes Pereira, L.M. G., 1998. Errors and accuracy estimates of laser data acquired by various laser scanning systems for topographic applications, *ISPRS Journal of Photogrammetry and Remote Sensing*, Vol. 53, No. 5, pp. 245-261.

Hyyppä, J., Hyyppä, H., Litkey, P., Yu, X., and Haggrén, H., 2004. Algorithms and methods of airborne laser scanning for forest measurements, *Proceedings of the ISPRS working group VIII/2 'Laser-Scanners for Forest and Landscape Assessment'*, Vol. XXXVI, Part 8/W2, 3-6 October, Freiburg, Germany. pp. 82–89.

Kager, H., 2004. Discrepancies between overlapping laser scanning strips - simultaneous fitting of aerial laser scanner strips, *International Archives of Photogrammetry, Remote Sensing and Spatial Information Sciences*, Vol. 35, Part B1, pp. 555–560.

Katzenbeisser, R., 2003. About the calibration of LiDAR sensors, *Proceedings of the ISPRS working group III/3 workshop, "3-D Reconstruction from Airborne Laser-scanner and InSAR Data"*, [CD-ROM]. 8-10 October, Dresden, Germany.

Kilian, J., Haala, N., and Englich, M., 1996. Capture and evaluation of airborne laser scanner data, *International Archives of Photogrammetry and Remote Sensing, WG I/1*, 12-18 July, Vienna, Austria. pp. 383–388.

Koch, K.-R., 1999. *Parameter Estimation and Hypothesis Testing in Linear Models*, Springer-Verlag, New York, US, 333p.

Kraus, K. and Pfeifer, N., 2001. Advanced DTM generation from LiDAR data, *International Archives of the Photogrammetry, Remote Sensing and Spatial Information Sciences*, Vol. XXXIV, Commission III/WG3, pp. 23–30.

Kubik, K., 1991. Relative and absolute orientation based on linear features, *ISPRS Journal of Photogrammetry and Remote Sensing*, Vol. 46, No. 4, pp. 199-204.

Lee, C., and Bethel, J. S., 2004. Extraction, modelling, and use of linear features for restitution of airborne hyperspectral imagery, *ISPRS Journal of Photogrammetry and Remote Sensing*, Vol. 58, No. 5-6, pp. 289-300.

Lee, J., Yu, K., Kim, Y., and Habib, A.F., 2007. Adjustment of Discrepancies between LiDAR Data Strips Using Linear Features, *IEEE Geoscience and Remote Sensing Letter*, Vol. 4, No. 3, pp. 475-479.

Li Q., and Griffiths, J. G., 2000. Iterative Closest Geometric Objects Registration, *Computers & Mathematics with Applications*, Vol. 40, No. 10, pp. 1171-1188.

Lemmens, M., 2009. Airborne LiDAR Sensors, *GIM International*, Vol. 23, No. 2, pp. 16-19.

Maas, H.G., 2000. Least-squares matching with airborne laser-scanning data in a TIN structure, *International Archives of Photogrammetry and Remote Sensing,* 16-22 July, Amsterdam, Netherlands. pp. 548-555.

Mallet, C. and Bretar, F., 2009. Full-waveform Topographic LiDAR: State-of-the-art, *ISPRS Journal of Photogrammetry and Remote Sensing*, Vol. 64, No. 1, pp. 1-16.

May, N. C. and Toth, C. K., 2007. Point positioning accuracy of airborne lidar systems: a rigorous analysis, *International Archives of Photogrammetry, Remote Sensing and Spatial Information Sciences*, Vol. 36, Part 3/W49B, pp. 107-111, 2007.

McGlone, J.C., Mikhail, E.M., Bethel, J., and Mullen, R., 2004. *Manual of Photogrammetry (5th Edition)*, American Society for Photogrammetry and Remote Sensing, Bethesda, US, 1151p.

Mikhail, E. M. and Ackerman, F., 1976. *Observations and Least Squares*, University Press of America, Lanham, US, 497p.

Morin, K.W., 2002. *Calibration of Airborne Laser Scanners*, M.S. thesis, Department of Geomatics Engineering, the Univertisy of Calgary, Calgary, Canada.

Mulawa, D., 1989. *Estimation and photogrammetric treatment of linear features*, Ph.D. Dissertation, School of Civil Engineering, Purdue University, West Lafayette, US.

Mücke, W., 2008. *Analysis of full-waveform airborne laser scanning data for the improvement of DTM generation*, Master's thesis, Institut für Photogrammetrie und Fernerkundung, Technische Universität, Wien, Austria. http://publik. tuwien.ac.at/files/PubDat 170289.pdf (accessed April 2010).

Optech, 2007. ALTM 3100 specifications, http://www.optech.ca/pdf/Specs/specs_ altm_ 3100.pdf (accessed November 2007).

Park, S., and Subbarao, M., 2003. An accurate and fast point-to-plane registration technique, *Pattern Recognition Letters,* Vol. 24, No. 16, pp. 2967-2976.

Pfeifer, N., Elberink, S.O., and Filin, S., 2005. Automatic Tie Elements Detection for Laser Scanner Strip Adjustment, *ISPRS WG III/3, III/4, V/3 Workshop "Laser scanning 2005"*, 12-14 September, Enschede, the Netherlands. pp. 1682-1750.

Schenk, T., 2001. *Modelling and Analyzing Systematic Errors in Airborne Laser Scanners*, Technical Notes in Photogrammetry, Vol. 19, The Ohio State University, Columbus, US.

Schnadt, K. and Katzenbeisser, R., 2004. Unique airborne fiber scanner technique for application-oriented LiDAR products, *International Archives of Photogrammetry, Remote Sensing and Spatial Information Sciences*, Vol. XXXVI, Part 8/W2. pp. 19-23.

Shan, J. and Toth, C. K., 2009. *Topographic Laser Ranging and Scanning*, CRC Press, Boca Raton, US, 590p.

Shin, S. W., Habib, A., Ghanma, M., Kim, C., and Kim, E., 2007. Algorithms for Multi-Sensor and Multi-Primitive Photogrammetric Triangulation, *ETRI Journal*, Vol. 29, No. 4, pp. 411-420.

Silfvast, W. T., 2004. *Laser Fundamentals (2nd Edition)*, Cambridge University Press, Cambridge, UK, 642p.

Skaloud, J. and Lichti, D., 2006. Rigorous approach to boresight self-calibration in airborne laser scanning, *ISPRS Journal of Photogrammetry and Remote Sensing*, Vol. 61, No. 6, pp. 47-59.

Skaloud, J. and Schaer, P., 2007. Towards automated LiDAR boresight self-calibration, *The 5th Inetrnational Symposium on Mobile Mapping Technology*, [CD-ROM]. 28-31 May, Padua, Italy.

Song, J., Han, S., Yu, K., Kim, Y., 2002. Assessing the possibility of land-cover classification using LiDAR intensity data, *International Archives of Photogrammetry, Remote Sensing and Spatial Information Sciences 34 (Part 3B)*, 9-13 September, Graz, Austria, pp. 259–262.

Toth, C. K., 2002. Calibrating airborne LiDAR systems, *Proceedings of ISPRS Commission II Symposium*, 20-23 August, Xi'an, China, pp. 475-480.

Vaughn, C.R., Bufton, J.L., Krabill, W.B., and Rabine, D.L., 1996. Georeferencing of airborne laser altimeter measurements, *International Journal of Remote Sensing*, Vol. 17, No. 11, pp. 2185-2200.

Vosselman, G., 2002. Strip offset estimation using linear features, *3rd International Workshop on Mapping Geo-Surfical Processes using Laser Altimetry*, [CD-ROM]. 7-9 May, Columbus Ohio, US.

Wang, M. and Tseng, Y. H., 2004. LiDAR data segmentation and classification based on octree structure, *XXth International Society for Photogrammetry and Remote Sensing (ISPRS) Congress*, Istanbul, Turkey

Weber, M. J., 1999. *Handbook of Laser Wavelength*, CRC Press, Boca Raton, US, 784p.

Wehr, A. and Lohr, U., 1999. Airborne laser scanning - an introduction and overview, *ISPRS Journal of Photogrammetry and Remote Sensing*, Vol. 54, No. 2-3, pp. 68-82.

Wolf, P. R. and Ghilani, C. D., 1997. Adjustment computations: statistics and least squares in surveying and GIS, John Wiley and Sons, INC., New York, US, 564p.

Xudong, L., Xuedong, Z., and Youchuan, W., 2005. A kind of filtering algorithms for LiDAR intensity image based on flatness terrain, *Proceedings of the International Symposium on Spatio-temporal Modeling, Spatial Reasoning, Analysis, Data Mining and Data Fusion*, 27-29 August, Beijing, China. http://www.isprs.org/proceedings/XXXVI/2-W25/Proceedings_STM05.html (accessed April 2010).

Zhang, Z., 1994. Iterative point matching for registration of free-form curves and surfaces, *International Journal of Computer Vision*, Vol. 13, No. 2, pp. 119-152.